

---


Electronic Theses and Dissertations, 2004-2019

---

2019

## Design and Fabrication of Scalable Multifunctional Multimaterial Fibers and Textiles

Felix Tan  
*University of Central Florida*

 Part of the [Electromagnetics and Photonics Commons](#), and the [Optics Commons](#)  
Find similar works at: <https://stars.library.ucf.edu/etd>  
University of Central Florida Libraries <http://library.ucf.edu>

This Doctoral Dissertation (Open Access) is brought to you for free and open access by STARS. It has been accepted for inclusion in Electronic Theses and Dissertations, 2004-2019 by an authorized administrator of STARS. For more information, please contact [STARS@ucf.edu](mailto:STARS@ucf.edu).

---

### STARS Citation

Tan, Felix, "Design and Fabrication of Scalable Multifunctional Multimaterial Fibers and Textiles" (2019). *Electronic Theses and Dissertations, 2004-2019*. 6831.  
<https://stars.library.ucf.edu/etd/6831>

DESIGN AND FABRICATION OF SCALABLE MULTIFUNCTIONAL MULTIMATERIAL  
FIBERS AND TEXTILES

by

FELIX A. TAN

B.S. Physics, University of Florida, 2008

M.S. Optics, University of Central Florida, 2014

A dissertation submitted in partial fulfilment of the requirements  
for the degree of Doctor of Philosophy  
in the College of Optics & Photonics  
at the University of Central Florida  
Orlando, Florida

Summer Term  
2019

Major Professor: Ayman F. Abouraddy



© 2019 Felix A. Tan

## ABSTRACT

Multimaterial fibers eschew the traditional mono-material structures typical of traditional optical fibers for novel internal architectures that combine disparate materials with distinct optical, mechanical, and electronic properties, thereby enabling novel optoelectronic functionalities delivered in the form factor of an extended fiber. This new class of fibers developed over the past two decades is attracting interest from researchers in such different fields as optics, textiles, and biomedicine. The juxtaposition of multiple materials integrated at micro- and nanoscales in complex geometries while ensuring intimate smooth interfaces extending continuously for kilometers facilitates unique applications such as non-invasive laser surgery, self-monitoring fibers, e-textiles, and extreme-environment tethers.

In this work, I focus on the scalable manufacturing of novel multimaterial fibers that make possible the fabrication of hundreds of kilometers of optical micro-cables and producing fibers at volumes commensurate with the needs of the textile and apparel industry. Although a multiplicity of fabrication schemes exists, I have investigated thermal drawing and melt-extrusion for thermo-forming of multimaterial fibers. Such fibers can be readily integrated with a broad range of downstream processes and techniques, such as textile weaving, precision-winding of fiber micro-cables, and inline functional coating. Specifically, I have developed a hybrid fabrication approach to produce robust optical fibers for single-mode and multi-mode mid-infrared transmission with the added possibility of high-power-handling capability. Second, I describe an optoelectronic fiber in which an electrically conductive composite glass is thermally co-drawn in a transparent glass matrix with a crystalline semiconductor and metallic conductors, which is the first fully integrated thermally drawn optoelectronic fiber making use of a traditional semiconductor. Third, I appropriate the industry-proven system of multicomponent melt-extrusion traditionally utilized for the scalable production of textile yarns and non-woven fabrics to produce our multimaterial fiber structures previously

fabricated via thermal drawing. This has enabled melt-spinning of user-controlled color-changing fibers that are subsequently woven into active color-changing fabrics. I additionally report the design and prototyping of structured capacitive fibers for potential integration into advanced functional e-textiles. Finally, I have produced a new class of optical scattering materials based on designer composite microspheres by exploiting a recently discovered capillary instability in multimaterial fibers produced by thermal drawing, multifilament yarn spinning, and melt-extruded non-woven fabrics.

Dedicated to my loving Abuelas, my supportive family, and my steadfast friends.

## ACKNOWLEDGMENTS

None of this work would have been possible without the constant guidance, patience, and direction from my advisor Dr. Ayman Abouraddy. His trust in my abilities and unwillingness to accept less than my best effort sparked the ambition and confidence I possess today. I thank him greatly.

For their guidance and valuable feedback, I would also like to thank my doctoral committee: Professors Aristide Dogariu, Demetrios Christodoulides, and Yuanli Bai. I likewise extend my gratitude to my groupmates, especially Dr. Joshua Kaufman, Dr. Ali Jahromi, Dr. Shi Chen, Dr. Scott Webster, Dr. Soroush Shabahang, Dr. Guangming Tao, Morgan, Murat, Abbas, Michael, Robert, and all of my past and present colleagues, friends, and staff at CREOL.

Lastly, and definitely not least, I need to thank my family for their unwavering support and faith in my (often wayward and headache-inducing) process of growing into the man I am today. My sister, Christine, and my loving parents, Chino & Ivonne, are especially near and dear to me. They continue to illuminate my path forward, and I cherish their opinion and perspective.

## TABLE OF CONTENTS

LIST OF FIGURES . . . . .	x
LIST OF TABLES . . . . .	xiii
CHAPTER 1: INTRODUCTION . . . . .	1
CHAPTER 2: BENCHTOP RAPID-PROTOTYPING OF MULTIMATERIAL FIBERS . . . . .	4
2.1 Principles of Extrusion . . . . .	6
2.2 Benchtop Ram Extrusion . . . . .	9
2.3 Principles of Thermal Fiber Drawing . . . . .	14
2.4 Benchtop Draw Tower . . . . .	19
2.5 Case Study: Polymer Light Pipe . . . . .	22
2.6 Case Study: High-Concentration Additive Doping . . . . .	27
2.7 Case Study: 3D-Printed Fiber Preforms . . . . .	30
CHAPTER 3: ROBUST MID-IR OPTICAL FIBERS . . . . .	34
3.1 Hybridized Polymer/ChG Fiber Fabrication . . . . .	35
3.2 Low-Loss Transmission with AR Coatings . . . . .	38

3.3	High-Power Transmission . . . . .	41
3.4	Efficient QCL Coupling . . . . .	43
CHAPTER 4: MONOLITHIC OPTOELECTRONIC FIBER DEVICE . . . . .		45
4.1	Electrically Conductive Composite Glass . . . . .	48
4.2	Design and Construction of an Intermediate- $T_g$ Draw Tower . . . . .	51
4.3	Fiber Fabrication and Structural Characterization . . . . .	53
4.4	Characterization of Optoelectronic Properties . . . . .	56
CHAPTER 5: DESIGNER COMPOSITE MICROSPHERES FOR TUNABLE OPTICAL SCATTERING . . . . .		59
5.1	Motivation: "Macroscopic Dipole" Scattering . . . . .	62
5.2	Thermal Fiber Drawing Approach . . . . .	65
5.3	Characterization of the Optical Scattering Properties . . . . .	68
CHAPTER 6: MULTICOMPONENT EXTRUSION OF NOVEL FUNCTIONAL FIBERS		72
6.1	Continuous Multifilament and Non-Woven Fabrics . . . . .	75
6.2	Thermochromic Fabrics . . . . .	78
6.3	Capacitive Fibers for Electronic Textiles . . . . .	81

CHAPTER 7: DISCUSSION . . . . . 83

REFERENCES . . . . . 87



## LIST OF FIGURES

Figure 2.1:	Benchtop Ram Extruder . . . . .	11
Figure 2.2:	BEX Components . . . . .	12
Figure 2.3:	Thermal Fiber Drawing Overview . . . . .	15
Figure 2.4:	Schematic of Thermal Fiber Drawing Modeling Parameters . . . . .	16
Figure 2.5:	Benchtop Draw Tower . . . . .	20
Figure 2.6:	BDT Components . . . . .	21
Figure 2.7:	Polymer Optical Fiber Extrusion and Drawing . . . . .	22
Figure 2.8:	Stack and Draw Technique . . . . .	25
Figure 2.9:	Polymer Light Pipe Characterization . . . . .	27
Figure 2.10:	Structured Fibers with High-Concentration Additives . . . . .	28
Figure 2.11:	Structured Spheres with Compartmentalized Functionalities . . . . .	30
Figure 2.12:	Dual-Material 3D-Printing System . . . . .	31
Figure 2.13:	3D-Printed Dual-Material Preforms . . . . .	33
Figure 3.1:	Hybridized Fiber Fabrication Overview . . . . .	35
Figure 3.2:	Specialty Fiber Cane Puller . . . . .	36

Figure 3.3:	Mid-IR Fiber Preform and Drawing . . . . .	37
Figure 3.4:	Mid-IR Optical Fiber Cross-Section . . . . .	39
Figure 3.5:	AR Coating on Mid-IR Fiber . . . . .	40
Figure 3.6:	Mid-IR Transmission and Tensile Strength Testing . . . . .	41
Figure 3.7:	High-Power CW Transmission at 2053 nm . . . . .	42
Figure 3.8:	Experimental Setup for QCL Coupling . . . . .	43
Figure 3.9:	Experimental Results for QCL Coupling . . . . .	44
Figure 4.1:	Review of Metal-Insulator-Semiconductor Fibers . . . . .	46
Figure 4.2:	Metal-Insulator-Semiconductor Device Fiber Motivation . . . . .	48
Figure 4.3:	Conductive Composite Glass Fabrication Overview . . . . .	49
Figure 4.4:	Intermediate- $T_g$ Draw Tower . . . . .	52
Figure 4.5:	M-I-S Device Initial Trials . . . . .	54
Figure 4.6:	M-I-S 3-Layer Device Fiber . . . . .	55
Figure 4.7:	M-I-S 5-Layer Device Fiber . . . . .	57
Figure 4.8:	Optoelectronic Characterization of 5-Layer Device Fiber . . . . .	58
Figure 5.1:	Schematic of PRI in Fiber . . . . .	59
Figure 5.2:	Schematic Overview of Dipole-like Scattering from Microspheres . . . . .	61

Figure 5.3:	Dispersion vs. Distribution of Additives . . . . .	63
Figure 5.4:	Comparison of Additive Compounding . . . . .	64
Figure 5.5:	Characterization of Fiber Precursor for Composite Microspheres . . . . .	66
Figure 5.6:	SEM of Extracted Composite Microspheres . . . . .	67
Figure 5.7:	Optical Characterization of Composite Microspheres . . . . .	69
Figure 5.8:	Tunable Scattering Results from Composite Microspheres . . . . .	70
Figure 6.1:	Fiber Extrusion vs. Thermal Fiber Drawing . . . . .	72
Figure 6.2:	Bicomponent Screw Extrusion . . . . .	74
Figure 6.3:	Extruded Bicomponent Fibers on Bobbins . . . . .	76
Figure 6.4:	Comparison of Composite Core Fibers . . . . .	77
Figure 6.5:	Composite Spheres from Non-Woven Bicomponent Fabric . . . . .	78
Figure 6.6:	User-Controlled Color-Changing Fabrics . . . . .	79
Figure 6.7:	Capacitive Fiber Cross-Sections . . . . .	81
Figure 6.8:	Capacitive Fabric Characterization . . . . .	82

## LIST OF TABLES

Table 3.1: Mid-IR Optical Fiber Transmission . . . . .	40
--	----

## CHAPTER 1: INTRODUCTION

Few innovations pre-date and persistently thread the fabric of society through the modern era than fibers. Recently reported work provides evidence of pre-historic hunters making cords for hafting stone tools, weaving baskets, or sewing garments from spun, dyed, and knotted flax as early 32 thousands years before the present [1]. By the Bronze Age, a thriving textile industry on a global scale had already refined familiar techniques such as spinning, dyeing, weaving, and knitting for mass production [2]. Textile manufacturing technology remained largely unchanged until the mechanization and transition to assembly lines characteristic of the Industrial Revolution. Advances in chemistry and materials processing eventually led to a major paradigm shift away from natural fibers with the development of synthetic polymers during the late 19<sup>th</sup> and early 20<sup>th</sup> centuries. These synthetic fibers fueled an explosion of engineered textiles whose fallout persists today spanning functional goods ranging from penetration-resistant body armor[3, 4], to surgical aids such as drug-eluting sutures[5] and resorbable gauze[6], to advanced filtration systems made of non-woven fabrics with nano-scale fibers[7], and textile composites for robust light-weight structural reinforcement[8].

Inorganic fibers similarly evolved into indispensable fixtures of modern life [9]. In a wool, they can provide favorable thermal insulation[10]; as nano-scale fibers and tubes, they can exhibit enhanced electrical properties[11], find utility as anti-microbial[12] and bio-filtration systems[13], and service specialty applications as high-temperature composites parts[14] and lubricants[15]. Arguably the most revolutionary inorganic fiber technology of the last half century is the invention of the silica optical fiber, enabling information exchange at unprecedented speeds and essentially ushered in an irreversible age of global connectivity. The workhorse design of an optically dense guiding core with a slightly lower refractive-index cladding has changed little since conception, as has the top-level methodology for fabrication of these fibers. The brunt of technological devel-

opment in the intervening time instead focused on increasing production yield while maintaining nanometer-scale tolerances and on improving the purity and composition of the glass to thereby minimize losses, commensurate with the demand for long haul transmission with reduced energy consumption. Related developments in the form of signal enhancement with active dopants and multiplexed data channels further advanced the capabilities for telecommunication.

The fibers discussed thus far, although exhibiting broad and technical functionalities, possess relatively simple architectures along their length. The development of fibers with multiple material phases possessing markedly different optical, mechanical, and electronic properties in complexly structured, axially continuous architectures (thereby distinguished from composite fibers with embedded discrete phases) has only recently ignited as an active research interest in fields including optics, textiles, and bio-medicine. Such *multimaterial* fibers thereby enable unique applications such as non-invasive laser surgery[16–18], self-monitoring fibers[19–21], e-textiles[22, 23], and extreme-environment tethers[24].

This work discusses the scalable manufacturing of novel multimaterial fibers that make possible the fabrication of hundreds of kilometers of optical micro-cables and producing fibers at volumes commensurate with the needs of the textile and apparel industry. Although a multiplicity of fabrication schemes exists, broadly categorized as direct assembly, chemical synthesis, and thermoforming techniques, the focus here is on the latter subsets of thermal drawing and melt-extrusion of multimaterial fibers. Some cases require adapting and incorporating two or more of these techniques into the fabrication scheme, especially as the fiber architecture and implementation increase in complexity and scope. Such fibers can be readily integrated with a broad range of downstream processes and techniques, including textile weaving, precision-winding of fiber micro-cables, and inline functional coating.

The fabrication schemes discussed bridge the development life-cycle from initial prototype at the

laboratory scale to near commercial-ready pilot scale production on multicomponent extrusions systems. Specifically, the first chapter discusses the design and validation of a custom bench-top system for rapid-prototyping of thermally drawn fiber devices produced from ram-extruded preforms. These devices include an all-polymeric light pipe, structured spheres containing multiple compartmentalized functionalities, and digitally designed 3D-printed preforms produced from custom-made filaments. Subsequent chapters discuss: the development of a hybrid fabrication approach to produce robust optical fibers for single-mode and multi-mode mid-infrared transmission with the added possibility of high-power-handling capability; the design and fabrication of an optoelectronic fiber in which an electrically conductive composite glass is thermally co-drawn in a transparent glass matrix with a crystalline semiconductor and metallic conductors, which is the first fully integrated thermally drawn optoelectronic fiber making use of a traditional semiconductor; the realization of a new class of optical scattering materials based on designer composite microspheres by exploiting a recently discovered capillary instability in multimaterial fibers produced by thermal drawing; and finally, the appropriation of an industry-proven system for multicomponent melt-extrusion traditionally utilized for the scalable production of textile yarns and non-woven fabrics to produce multimaterial fiber structures previously fabricated via thermal drawing. The system is adaptable to a host of additional industry-inspired processes including wire-coating, cable-jacketing, and staple fiber production. A first validation step of this system demonstrates the ability to scale fabrication of the optically scattering microspheres previously discussed using multifilament spinning and melt-extrusion of non-woven fabrics with micron-diameter fibers. The next step describes the melt-spinning of user-controlled color-changing fibers that are subsequently woven into active color-changing fabrics. The final step presents new experimental results related to the design and prototyping of structured capacitive fibers for potential integration into advanced functional e-textiles.

## **CHAPTER 2: BENCHTOP RAPID-PROTOTYPING OF MULTIMATERIAL FIBERS**

Commercialization of novel technology, especially that of a particularly complex or broad-scoped nature, persists as a desirable yet challenging ambition for many researchers. Innumerable development efforts failed to transition from good idea to consumed market product, and most often for no fault of the novelty, utility, or impact of the idea, nor for poor decisions on the part of the investigators. Likewise, it is challenging to enumerate an explicit list of protocols to follow upon analyzing those products that do succeed at market. It would seem "best-practices", learned experience, and well-established network of collaborators and industry partners dominate the discussion, along with a hesitancy to admit the silent role of fortune and good timing. Now, it is not implied here that commercialization is, nor should be, the primary goal of basic research, scientific or otherwise. Rather, that commercialization is but one consequence of the academic pursuits to probe, describe, predict, catalog, and disseminate, as the two efforts are inextricably tied by the real-world costs associated with both: new technology generates new wealth as a consequence of commercialization, which then directly or indirectly funds the development of new technology that in turn creates new wealth, and so on. It then follows that closing the loop in a more expeditious and efficient manner is beneficial to both academia and industry.

Establishing well-defined milestones against which to validate the progress and viability of new product development is a clear commonality among successfully executed commercialization and research efforts. Typically, for manufactured goods such as multimaterial fibers, one such early milestone is the Proof of Concept (PoC) in which physical phenomena investigated and characterized at the basic research level is combined with proven techniques appropriated from industrial practices. In some cases, the novelty mandates adaptation or hybridization of existing techniques



or, in rarer cases, the outright formulation of new processes. Conventions differentiate the individual terms that describe these early development stages across various fields and industries. Whatever the nomenclature employed, the primary goal of the PoC stage is to produce a working prototype that demonstrates a grasp on the underlying mechanisms and the ability of the design to function as intended. Good prototypes inform future development by identifying potential obstacles to scaling, materializing unanticipated limitations, and illuminating unnecessary features along the path to mass consumption or publication. Great prototypes accomplish these goals with the resources currently available in as quick and cost-efficient manner as possible.

The ability to manufacture single-material and certain multimaterial fibers at commercial scales has been demonstrated for a select number of applications and industries, most notably those relating to optical fibers for telecommunications and to fiber extrusions for the textiles. However, the development of novel, complexly structured multimaterial fibers has been fairly confined to academic settings at the laboratory scales due to the costs incurred were industry to adapt large-scale production machines for new fiber material systems that may never reach the consumer market. Modeling and simulation are tools often employed in other manufacturing settings to minimize these costs and potentially circumvent the need to produce working prototypes in order to determine viability of new concepts. However, applying this predictive methodology is complicated by the multidimensional parameter space associated with multimaterial fiber fabrication, namely material parameters such as interfacial fluid dynamics, viscoelastic effects, thermomechanical properties, additive loading, and the geometric allocation thereof, coupled with process parameters such as (for thermal drawing) preform construction, furnace temperature profile, quenching, and feed/pulling speeds or (for fiber extrusion) spinneret design, volumetric flow rates, heating, quenching, and take-up speeds. Adding downstream processes only further complicates the modeling effort. It follows then that, in most cases, novel fiber designs are best investigated empirically with parameter settings and adjustments informed by iterative manufacturing trials and previous experience

with similar systems. It is therefore desirable to implement a prototyping scheme that reliably produces scalable fiber samples while minimizing fabrication time, costs, and material consumption without sacrificing fiber functionality or performance.

With this in mind, a benchtop system was custom-designed and manufactured for rapid-prototyping of multimaterial fibers thermally drawn from extruded preforms. The system consists of a 1 m tall ram extruder and similarly sized drawing system that together can fabricate meters of fiber from grams of raw material in a few hours. The system is comprised of readily available components at a relatively low cost when compared to traditional optical fiber draw towers and occupies a fraction of the footprint. The minimalist design affords easy installation into academic and industrial research laboratories along with settings like classrooms and hobbyist workshops. In addition to providing rapid feedback on new technical concepts, the latter two settings highlight the secondary goal of the system to broaden the reach of the relatively new field to inspire new interest and applications incorporating multimaterial fiber form-factors. As such, the system was deliberately designed for simple operation with little to no training required thereby overcoming the entry barrier presented by the intimidating size, cost, and highly specialized features of traditional draw towers.

## **2.1 Principles of Extrusion**

There are two basic types of extruders: continuous and discontinuous (batch-type) extruders. Typically, continuous extruders utilize a rotating screw to transport, shear, and mix the material in the melt chamber (extruder barrel) and can be continually fed for steady flow of extruded material. Batch-type extruders have a reciprocating member (such as a piston or ram) that compresses and transports the material to the die. Extruders are generally referred to by the mechanism of material transport inside the melt chamber, i.e. screw extruder or ram extruder. Screw extrusion

is typically favored for production-scale applications due to the ability to continuously feed large quantities of material into the extruder. Moreover, process-specific control over parameters such as shear rate and residency time can be customized with complexly engineered screw geometries. On the other hand, the mechanism of screw transport relies on filling the extruder barrel volume to push the melt through the die and so finite material losses are expected. For costly samples with high additive loading, or for fiber prototypes based on laboratory batches of custom synthesized materials, extruding small gram-scale quantities with complete consumption (and no remaining waste) is near impossible in typical extruder designs. To overcome this limitation, there has been recent work in developing smaller batch screw extruders ( $<10$  g) [25]. However, these devices typically have a simplified screw design and internal re-circulation channel which makes up-scaling to continuously-fed, production-scale extruders difficult [26].

In contrast to screw extruders, the components of ram extruders are relatively simple in their geometries and functionality. Thus, it is a comparatively easier task to scale down the overall size of the device. For example, a syringe, perhaps the simplest form of a ram extruder, consists of a manually-actuated plunger (ram) and a cylindrical body in which both the chamber and die (syringe needle) are housed. Many 3D-printers also employ a form of ram extrusion by which a thermoplastic filament is fed into a small open-ended melt chamber that tapers down to the die aperture. In this configuration, the unheated body of the filament acts as the ram while the chamber and die are, once again, housed in the same body. However, the need for pre-fabricating the raw material (i.e. filament) adds an additional processing step to the manufacturing cycle which typically limits the adaptability for new development to scale to commercial levels. Continuously fed ram extruders for industrial-scale production do exist, although these are typically sufficiently large to permit top-loading of raw material at room temperature and additionally are difficult to control atmospheric conditions inside the melt chamber.

As mentioned, there are continuous-style ram extrusions operating at production scales. Likewise,

there are screw extruders configured for batch-style production. In particular, injection molding systems for thermoplastic polymers typically employ a screw extruder continuously fed but designed to deliver a finite amount (*shot*) of molten polymer to the mold. The screw-drive control mechanism could be based on a melt pressure feedback loop configured to deliver constant pressure to the mold. It could also be configured for constant volume shots based on the known melt density of the polymer. In either case, these parameters are set and tuned according to the specific properties of the mold and polymer. Although the operation and practices of injection molding are not directly applicable to fiber fabrication systems, it is mentioned here to establish that screw and ram extrusion systems differ primarily in the mechanism of melting and transporting the material in use. Independent of these two mechanisms, both systems can be configured to shape and quench the melt in a similar fashion, i.e. both systems are designed to feed molten states to an extrusion die.

As such, die design is arguably the most influential aspect of extrusion systems. The form factor of the extruded article (*extrudate*), the viscoelastic effects of the melt, production rate, and fluid instabilities are all important considerations in the design of a functional die. These each inform the computational effort involved regarding the melt velocity and temperature distribution in the die, the mechanical shape and properties of the die, the manner in which heat is delivered to the die, and the modularity required to accommodate different extrudate materials and geometries. For instance, using the same screw extruder, changing the die design can transition the production process from continuous filament (fiber) to non-woven fabric, or to wire coating, cable jacketing, blown-film, continuous sheets, or to profiled foams, rods and bars. As such, the effects of the die design on the extrudate are important to consider in the context of the specific process goals and parameters, as much as it is important to consider the effects of the melt properties on the design of the die.

One such effect to consider in particular is *die swelling*, also known as the Barus effect. It is a

well-known phenomenon in extrusion of either type, and is characterized by the tendency of extruded melt bulge at the die exit. The effect is more predominant in polymer extrusion due to the large molecular weights. Prior to entering the die, the molten stream flows at a constant rate with the molecular entanglements relaxing into fairly spherical domains. Upon entering the restricted area die, the polymer is forced into a more rapid flow and these entanglements elongate along the die axis direction. Due to the finite extent of real dies, these elongated domains return to their prior spherical shape and thereby cause the melt to swell upon exiting the die. With a sufficiently large  $L/D$  ratio, the majority of the elongated domains are able to relax back to a smaller spherical morphology thereby mitigating the effect. As such, the  $L/D$  ratio is an important figure of merit for extrusion die design. Optimization strategies further consider parameters ranging from simple volumetric flow and pressure resistance, to more practical parameters such as velocity distribution, residency times, and shear rates [27]. These strategies are well-established and investigated, with methods categorized as gradient-free (coordinate [28], rotating coordinate [29], pattern search [30], DSC [31], simplex and complex [32]), gradient-based [28], stochastic (Monte Carlo), and evolutionary (biology inspired) methods [33–35].

## 2.2 Benchtop Ram Extrusion

In the context of benchtop rapid-prototyping of fibers, the discussion so far has established that gram-scale batches are best handled by ram extrusion systems, if the goal is to also minimize the unconsumed material. Such ram extruders readily produce rods for use in preforms for a wide range of thermally drawn multimaterial fibers[36, 37]. Dies with circular cross-section are among the simplest to design and produce such cylindrical rods. Additionally, although an important figure of merit, the  $L/D$  ratio and overall die design will need to balance the goal to minimize material waste with the quality of the extruded preform. A useful rapid-prototyping system for

drawn fibers would then repeatably produce cylindrical rods of sufficient length to construct a preform, minimize the material required to execute the extrusion, minimize the material lost during the extrusion, and provide modular control and features to accommodate broad range of material processing temperature, viscosity, additives, and atmospheric conditions. To meet these criteria, the Benchtop Ram Extruder (BEX) was custom-designed and manufactured (Figure 2.2). The overall height is  $\approx 80$  cm with a base surface area of  $30.5 \text{ cm} \times 30.5 \text{ cm}$ . The critical features of the BEX to control are the 1) applied load on the material, the 2) melt chamber temperature, the 3) die assembly, and 4) atmosphere control via degassing of the melt chamber. The last feature ensures that the resulting extrudates are fully compacted into a homogeneous and bubble-free billet, especially when the starting material is porous or non-uniformly shaped. In typical small-scale ram extruders, melt chambers volumes are on the order of hundreds of cubic centimeters. Thus, at least tens of grams are required per batch in order to compensate for loss at the outset of extrusion and for the remnant material left in the die and chamber. By scaling down the system components even further in size ( $< 25 \text{ cm}^3$ ), the BEX can produce extrudates with as little as  $< 1 \text{ g}$  of raw material at a small fixed loss in the tens of milligrams.

The components of the extruder are housed in a support structure fabricated of 9.5 mm thick aluminum plates and 37 mm wide T-slotted aluminum framing extrusions. Aluminum was selected for its relatively low density and cost in comparison to steel alloys. Although not as strong or rigid as steel, aluminum performs sufficiently well under normal extrusion conditions. The stand is separated into two main sections with the bottom-section plate-to-plate displacement measuring 17.8 cm and the top-section plate-to-plate displacement measuring 30.5 cm. The top plate measures  $20.3 \text{ cm} \times 20.3 \text{ cm}$  in surface area and supports the motor assembly. The middle plate supports the main body of the extruder, namely the heater block, extrusion sleeve, and vacuum cap. The critical design feature of the frame assembly is to minimize shaft misalignment between the ram shaft and the axis of the melt chamber. Assuming the center of the chamber is the BEX origin

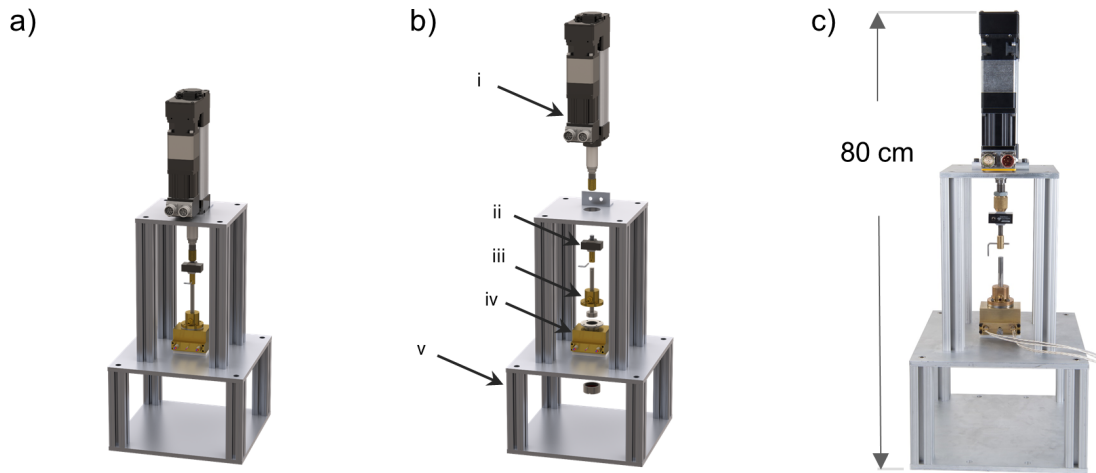


Figure 2.1: a) Rendered schematic of the BEX assembly. b) Exploded view of the BEX highlighting the (i) linear actuator, (ii) load cell, (iii) vacuum cap, (iv) heater block, and (v) support stand subassemblies. c) Actual photograph of fully assembled BEX system.

with x-axis to the right, y-axis to the back, and z-axis oriented along the chamber axis, the support frame assembly is symmetric about the yz-plane. As such, any mismatch in shaft alignment due to mounting to the frame is significantly reduced by dimensioning all hole patterns on the plates using the yz-plane as the primary reference datum.

The ram applies load to the sample by thrust delivered through the linear rod actuator. A servomotor in series with a 700:1 gearhead drives the actuator, resulting in ram speeds on the order of several microns per second. The use of a servomotor ensures precise control over the position of the ram and minimizes adverse “ripples” in the speed profile while being capable of delivering up to 1.33 kN (300 lbf) of thrust to the ram. In order to safeguard the motor assembly from damage, a load cell is affixed between the actuator rod end and the piston assembly. The load cell is small in overall profile, measuring  $\approx 25$  mm in width and height. Software handles feedback from the load cell, programmed to kill drive to the motor if the measured load is higher than the set-point. In addition to protecting the motor assembly, the data from the load cell enables indirect monitoring

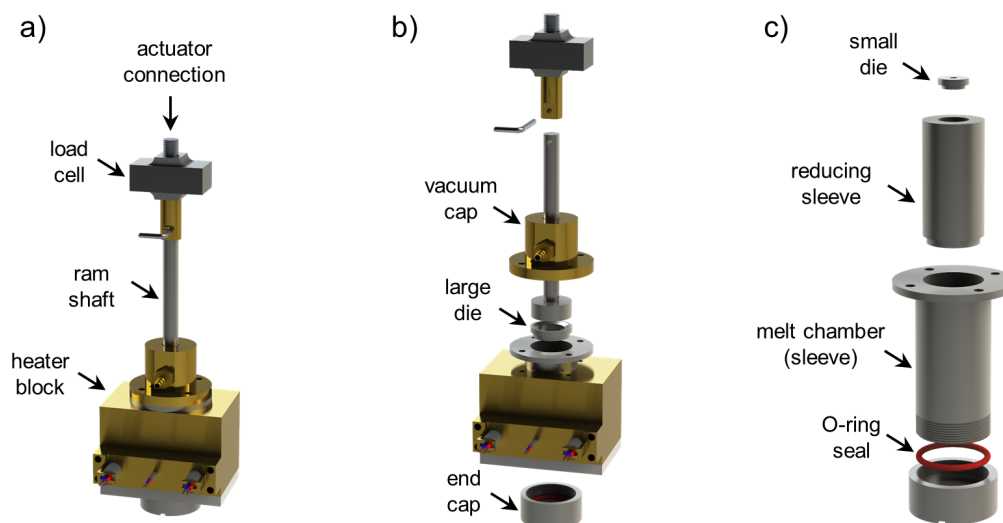


Figure 2.2: a) Rendered schematic of the primary BEX components. Not included are the linear actuator and support stand. b) Exploded view of the BEX components. c) Exploded view of the sleeve and die subassembly with the reducing sleeve configuration for small diameter extrusions.

of the sample viscosity in that the load required to propagate the extrusion is proportional to the pressure drop through the die which is related to the sample viscosity and ram speed.

The heater block (HB) subassembly delivers heat to the sample (Figure 2.2). The body of the HB measures  $5.1 \text{ cm} \times 7.6 \text{ cm} \times 5.1 \text{ cm}$  ( $L \times W \times H$ ) and is made of brass for its thermal conductivity and machinability. The HB houses the extruder sleeve and die subassemblies in a vertical bore at its center. Insertion cartridge heaters (CHs) positioned on either side of the sleeve deliver heat to the system at thermal loads up to 150 W each and maximum cartridge temperature of  $700 \text{ }^\circ\text{C}$ . Other components of the extruder, namely the silicone gaskets, PTFE isolator, and PTFE vacuum transfer line, limit the maximum operating temperature to  $\approx 300 \text{ }^\circ\text{C}$ . A PID controller drives the CHs with a “normally open” mechanical relay configuration using feedback from an insertion thermocouple probe (TC). The TC tip abuts the sleeve exterior wall at a point equidistant from and in plane with the center axes of the CHs. Retaining clips secure the CHs to a small block of brass (heater panel) which allows for easy mounting. A 6 mm thick PTFE isolator block insulates the bottom face of



the HB from the rest of the extruder. Aside from being a safety precaution, the isolator mitigates heat-sinking into the aluminum frame surrounding the heater block.

The extrusion sleeve houses the sample and dies, and constitutes the melt chamber of the extruder (Figure 2.2c). The outer face of the sleeve body is threaded at the bottom in order to secure the cap during the heating and compression stages of extrusion. The sleeve has an outer diameter of 31 mm with an inner bore diameter of 25 mm. The sleeve is fabricated of stainless steel as opposed to brass in order to prevent adverse effects from corrosion and structural deformations resulting from repeated use. A small lip at the bottom of the sleeve supports top-loaded dies of various profiles, highlighting one of the modular aspects of the motorized system. In applications where only a small amount ( $<2$  g) of sample is to be extruded, a secondary sleeve can be top-loaded that is of smaller inner bore diameter. The dies used in this work have a relatively small length to diameter ( $L/D$ ) ratio than is typical of similar extruders—specifically, the 16 mm die has a length of 4 mm, or  $L/D = 0.25$ . Although larger  $L/D$  ratios improve uniformity of the extruded rods, larger ratios also increase the material loss per extrusion. Moreover, the sleeve length would have to increase and, thus, the overall height of the extruder.

The vacuum cap (VC) subassembly seals the melt chamber from ambient conditions during heating and compression of the sample. The VC is machined of brass, flange-mounted to the heater block and vented through a barbed pipe fitting. The VC center-bore has a slightly larger diameter than the ram shaft and contains two grooves that house silicone O-rings. These gaskets have an inner diameter (ID) slightly smaller than the ram shaft diameter and remain in place while the ram is in motion. An additional O-ring completes the seal between the vacuum cap and sleeve. The bottom face of the VC adjacent to the sleeve has a counter-bored recess sized to the ram head dimensions. This enables completely filling the sleeve with material with the ram fully retracted. The seal configuration maintains an absolute vacuum level down to  $\approx 1$  mbar, sufficiently evacuating volatiles from the melt chamber interior and preventing the formation of bubbles in the extrudate.

### 2.3 Principles of Thermal Fiber Drawing

Thermal fiber drawing (TFD) is the process by which a bulk solid (preform) transitions controllably and locally to a viscous state and pulled under load along an axis, thereby drawing out a molten strand that quenches and re-solidifies into an extended length fiber with reduced transverse area. With caveats dependent on the geometric complexity and material composition, the drawn fiber is a scaled-down replica of the preform and can therefore be imparted with features and compartmentalized functionalities on the micro- and nano-scale that would otherwise be difficult to achieve using "bottom-up" synthesis techniques. The scaling factor of fiber-to-preform area is known as the draw-down ratio (DDR) and is a powerful tool for characterizing the TFD process. For example, predetermining the DDR with a given preform construction informs the process parameters needed to produce desired fiber features. Conversely, measuring or calculating the DDR aids in predicting internal dimensions and other fiber properties by comparing to the preform. Conventions for explicitly defining the DDR vary and typically adopt a form that simplifies modeling of the draw dynamics for a specific preform architecture.

Figure 2.3 depicts a simplified schematic overview of the TFD process including ram extrusion of the preform rods. The critical process control parameters are 1) the fiber preform down feed rate, 2) the draw temperature profile (furnace), and 3) the pulling speed of the drawn fiber. Together with the preform architecture and constituent material thermoviscous properties, these parameters mutually vary the resultant fiber dimensions and the draw stress on the melt in the neck-down region. Upstream and downstream in-line process can be incorporated to further control the fiber architecture and apply additional advantageous properties. For example, in an upstream process, pressurized gas (or vacuum) could be fed into axial hollows of a preform to alter the relative dimensions of the fiber cross-section. A commonly employed downstream process in the optical fiber manufacturing industry involves passing the drawn silica fiber through an extruder or immersion

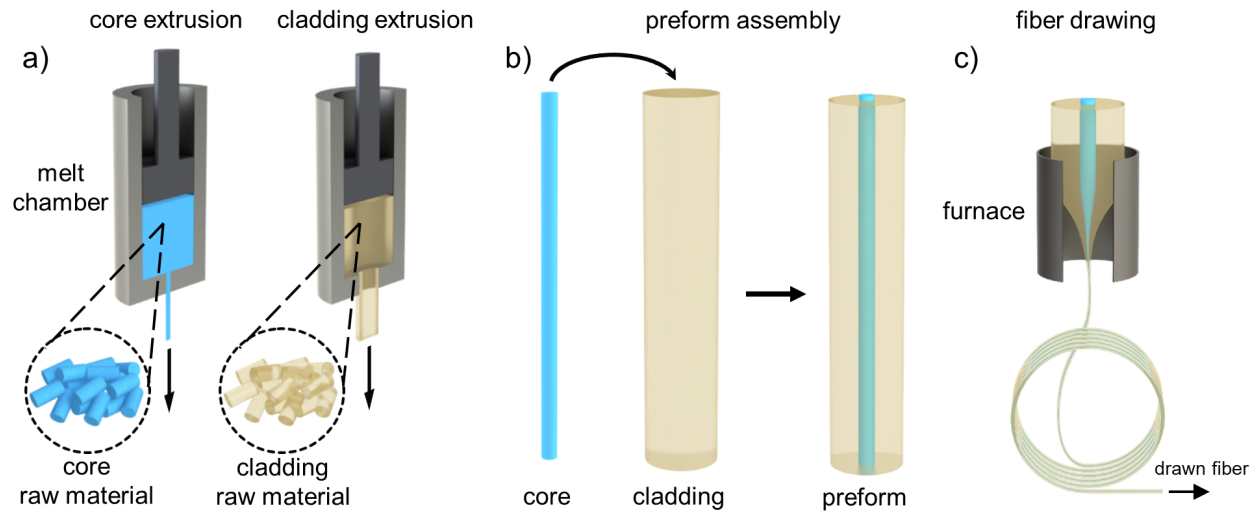


Figure 2.3: Schematic overview of thermal fiber drawing from extruder multimaterial preforms. a) Raw materials for the core and sheath (cladding) are extruded into rods with appropriate diameter. b) Preform assembly follows by machining a center-bore into the sheath rod and inserting the core rod. c) Assembled preform is thermally drawn in a system that controls the preform feed rate, furnace temperature profile, and fiber pulling rate.

bath to apply a thin coating for added mechanical robustness and flexibility.

As previously mentioned, adjusting the control parameters throughout the draw effects a change in the fiber characterized by the neck-down shape (DDR) and tensile load required to continuously pull from the neck-down region. Although predicting the DDR follows relatively directly from mass conservation for a homogeneous system, it is quite a challenge for preforms with multiple disjoint materials or axially continuous hollow structuring [38]. In fact, analytically determining the neck-down shape and draw dynamics for even the simplest case of a uniform cylindrical preform comprised of a single material requires accounting for capillary fluid instabilities, thermal profile and convection air currents in the furnace, preform surface emissivity and thermal conductivity, temperature-dependent density and viscosity changes, ambient and forced quenching effects, and stress- and shear-dependent viscosity for non-Newtonian fluids such as thermoplastic polymers [39–43]. That said, modeling the shape of the neck-down region has been well-studied

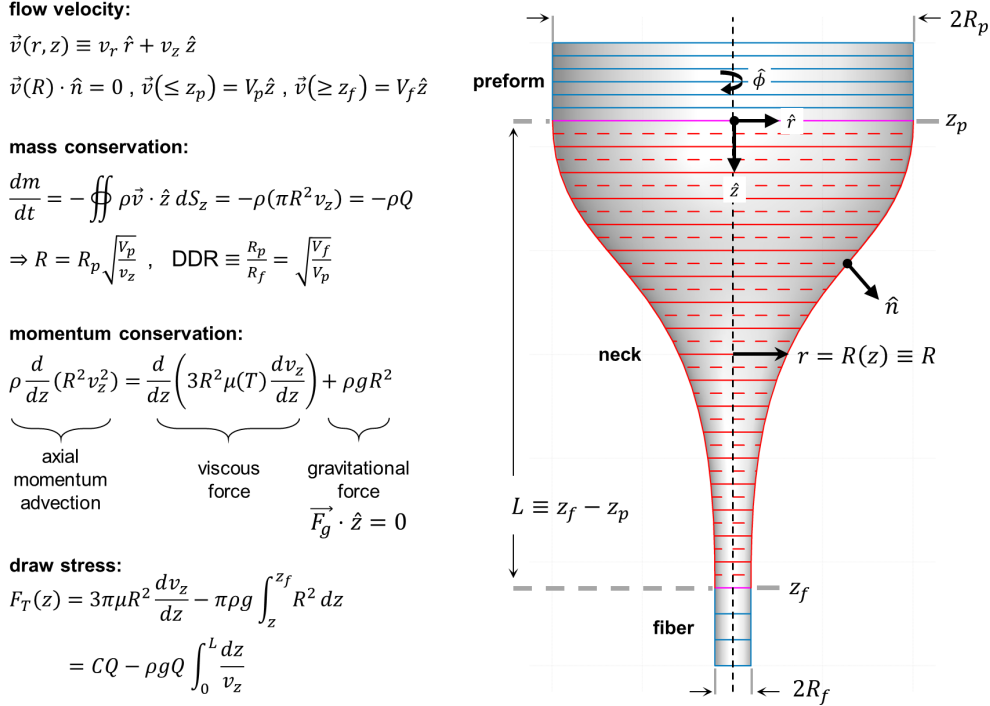


Figure 2.4: Schematic depicting modeling parameters a homogeneous preform with density  $\rho$  and viscosity  $\mu(T)$ . The red hatching highlights the neck-down region in which the material deforms due to thermal transition into a molten viscous state. The solid preform (quenched fiber) is fed (pulled) at a constant rate  $V_p$  ( $V_f$ ). Equating the mass flux along  $\hat{z}$  at  $z = z_p$  and  $z = z_f$  yields the overall DDR, while the generalized neck shape  $R(z)$  and axial flow velocity  $v_z$  are determined by applying the boundary conditions at the solid-molten transitions to the constitutive mass and momentum relations. The draw stress  $F_T(z)$  follows accordingly by balancing the tension with viscous and gravitational forces while neglecting the experimentally validated small contribution of advection [47, 48]. Closing the system entirely for modeling of the full process involves incorporating energy conservation of heat supplied by the furnace, preform surface emissivity, and internal thermal transport via conductance [49].

for the case of silica optical fiber drawing, in which various assumptions regarding material behavior and process conditions have been experimentally validated [44–46].

Figure 2.4 depicts the schematic overview of the necking process for a homogeneous preform. Efforts to model the radial neck profile during thermal deformation involve numerically solving the constitutive relations for viscous flow in a gravitational field (valid for the vertical orientation of the draw tower). The Navier-Stokes equations describe fluid motion and, compared to the

related Euler equations, additionally incorporate the effects of inertial and viscous forces in the context of mass and momentum conservation. Determining the tensile (draw) stress on the melt flow follows by balancing the gravitational, inertial, and viscous forces with the cohesive tension at the free boundary neck surface aligned with  $(\vec{n})$ . Due to the fairly high viscosity in the molten neck (compared to inviscid, water-like fluids and gases), the Reynolds number is sufficiently small and so the contribution from inertial forces is negligible. Additionally, it has been shown that contributions from non-Newtonian (viscoelastic) effects [50] and from capillary instabilities [51] are negligible following validation of modeling results with drawn fibers, again attributed to the relatively high viscosity and additionally to the short residency time in the molten state. With these considerations, general relations describing the draw dynamics follow accordingly.

Examining each relation provides insight into the fiber drawing process. From the DDR, it is clear that adjusting any of the input speeds necessarily alters the drawn fiber diameter and thereby alters the overall DDR for a fixed preform diameter. Likewise, if instead the DDR is predetermined so that, for instance, the dimensions of the internal preform architecture are reduced to a desired value, then the process speeds can be set to appropriate values given the preform diameter. The relations governing the preform shape inherit the preform thermoviscous properties along with the temperature profile in the furnace. Together, these subsequently influence the draw stress exhibited on the neck. In some applications, fiber functionality is heavily influenced by the "locked-in" stress during the draw. It is a bit more challenging to tease out the influence of preform (neck) diameter and axial velocity at first glance, but validated numerical simulations for typical draw tower configurations yield a general increase in draw stress for increasing radial extent and for increasing axial velocity (with fixed fiber pulling rate and furnace parameters). Alternatively, increasing the residency time by slowing the preform feed, increasing (decreasing) the preform temperature (viscosity), increasing the heating length, and decreasing fiber pulling speed will all decrease the draw stress in the neck.

Although the dynamics modeled and discussed pertained to a homogeneous preform system with solid, cylindrical geometry, the results and considerations apply quite sufficiently as a first-order approximation when the conditions are transitioned to multimaterial preform constructions, provided the majority comprises a comparably thermoplastic material with sufficiently high viscosity so as to maintain the low Reynolds number condition. As such, the preform can be cross-sectional "averaged" as a pseudo-homogeneous system with predictable thermoviscous behavior [20]. General constraints can be imparted on such multimaterial preforms to best assure feasible and stable drawing conditions. The primary preform material should be amorphous (glassy) with characteristic reversible softening behavior, and additionally should resist crystallizing in the melt. To preserve the geometric integrity of the fiber at large, that material should constitute the outer surface and thereby acts as the skeletal support for the fiber. If there are more than one such amorphous materials, all should have overlapping softening transitions while crystalline preform materials should melt below the process (draw) temperature, itself below the vaporization temperature of all constituents. Thermal expansion up to the draw temperature should be considered, as excessive mismatch can lead to fracturing upon quenching. Finally, fluid instabilities are always at play, especially when crystalline materials are incorporated into the preform as these tend to transition sharply to relatively low viscosity upon melting. Surface tension and relative miscibility likewise will inform and restrict preform architecture, as vertices and straight edges at material phase interfaces will tend to curve and deform as tension acts to minimize the surface energy. Finally, care must be taken to prevent intimate contact between crystalline materials, as they will mix once transitioned to liquid-scale viscosity.

## 2.4 Benchtop Draw Tower

With the principles of thermal drawing understood, and the utility and goal of rapidly prototyping multimaterial fibers for validation of concept and functionality in mind, the design and manufacture of a Benchtop Fiber Draw Tower (BDT) was executed. Depicted in Figure 2.5, the system is vertically orientated with an overall height of 111 cm and a base area of 31 cm × 31 cm. The mechanical support structure of the system is constructed of aluminum t-slotted extrusion framing and 9.5 cm thick sheet. The base area is 30.5 cm × 30.5 cm and the framing is cut to 30.5 cm in length. As in the BEX, the critical design feature of the frame assembly is to minimize shaft misalignment—in this case, between the down feed assembly, the axis of the furnace, and the high friction zone of the pulling assembly. Assuming now that the center of the furnace bore is the BDT origin with x-axis to the right, y-axis to the back, and z-axis oriented along the furnace axis, the support frame assembly is once again symmetric about the yz-plane against which all hole pattern dimensions are referenced.

Down feed of the preform into the furnace is provided by a linear slide table featuring a carriage operating on an Acme threaded rod with pitch of 1 mm. The slide table is vertically aligned with an overall travel of the carriage is 20 cm. Rotation of the Acme screw is provided by a servomotor in series with a 100:1 gearhead. Maximum linear travel speed of the positioning slide table is 12 mm/min with typical operating preform feed rates ranging from 0.5 mm/min to 2 mm/min. Use of a servomotor ensures tight tolerance of the linear speed of and torque delivered to the system, providing precise control over propagation of the neck during the draw. The fiber preform is mounted to the slide table via a centering lathe chuck and a custom-made bracket. The preform is first affixed to the end of a metal tube that is then secured into the jaws of the lathe chuck.

Control over the temperature is provided by a cylindrical tube furnace. The furnace used in the system has an inner diameter of 32 mm and maximum operating temperature of 500 °C. The length

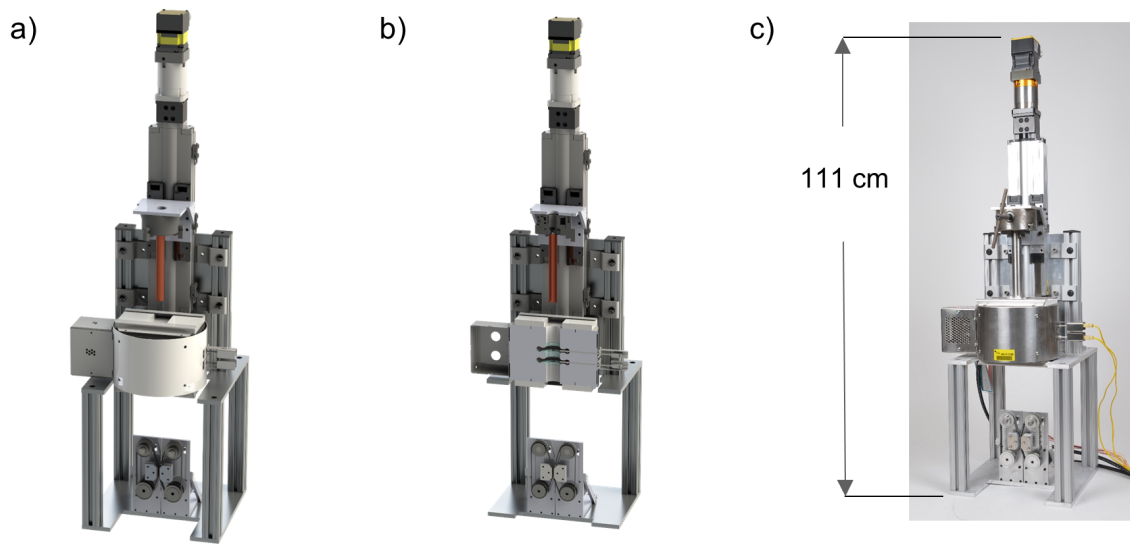


Figure 2.5: a) Rendered schematic of the BDT assembly. b) Section view of the BDT exposing the furnace interior. Two contiguous heating zones shape the temperature profile in the neck-down region. The preform axis aligns with the fiber pulling system below the furnace with a precision linear slide table and three-jaw centering lathe chuck. c) Actual photograph of fully assembled BDT system.

of the inner chamber is divided into four contiguous sections. The top and bottom sections are unheated and each measure 38 mm in length. The inner two zones each measure 25 mm in length and supply heat to the preform. As such, the overall bore length of the furnace is 12.7 cm. Each heated zone is independently driven so as to provide added control over the temperature profile inside the furnace. That is, different combinations of materials in the preform may require different thermal profiles within the furnace to optimize the neck propagation during fiber drawing. In most applications, as in the work described here, it is desirable to preheat the preform above the neck-down region. The thermal gradient outside the heated zones can be further controlled by the use of ceramic doors, irises, or insulation at the entrance and exit of the chamber.

The fiber pulling speed exiting the furnace is controlled by a tractor system employing timing belts, pulleys, and two stepper motors as depicted in Figure 2.6c. Without the tractor system, it is possible to draw fibers using only the furnace and control over position of the neck via the down



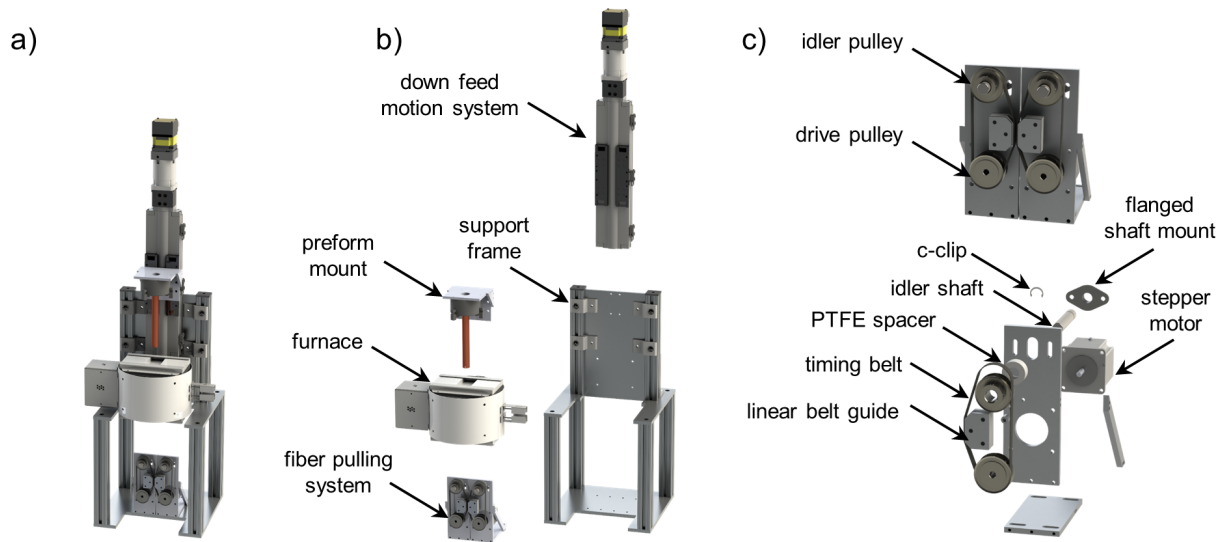


Figure 2.6: a) Rendered schematic of the BDT assembly. b) Exploded view highlighting the primary BDT subassemblies. c) Collapsed and exploded views of the fiber pulling tractor system.

feed mechanism. However, without the tractor, it is extremely difficult to control the ultimate fiber diameter and tension in the fiber. Depending on the draw down ratio and down feed of the preform, typical pulling speeds range from 0.25 m/min to 1 m/min. Since stepper motors have a tendency to impart ripples in the motion at small rotational speeds  $< 10$  rev/min, the use of a microstep drive becomes necessary. The rotational speed resolution of the microstepper is 0.0042 rev/s, or an equivalent linear travel speed of 26.9 mm/min. In order to accommodate the tractor system within the structure of the support stand, a rectangular section is removed from the bottom plate directly below the exit of the furnace. Situating the empty space over the edge of the table upon which the draw tower rests allows for the drawn fiber to be pulled vertically without the need for a spooling mechanism. The furnace axis aligns with the belt centers by appropriate positioning of the tractor, thereby gripping and pulling the drawn fiber collinear with the preform feed. There is  $\approx 200$  mm of separation between the furnace exit and the tractor to allow the fiber to harden and thus avoid deformation at the tractor.

## 2.5 Case Study: Polymer Light Pipe

A multimaterial fiber comprised of polystyrene (PS) and a cyclic olefin polymer (COP) was drawn in the BDT to validate the performance. The PS/COP fiber was previously drawn in a more traditional draw tower designed for operation up to 550 °C. In previous work, the PS was placed in the sheath (cladding) with the COP in the core. This fiber was fabricated for the purpose of generating in-fiber COP spheres using fluid instabilities in a controlled fashion. To build on the previous work, the same materials were drawn in opposite architecture, with the COP instead comprising the external sheath and the PS now in the core. The motivation for the architecture stems from the higher refractive index of the PS ( $\approx 1.59$ ) compared to that of the COP ( $\approx 1.53$ ), both values provided by respective manufacturers for visible wavelengths. The intended fiber will be validated at a wavelength of 635 nm with a large core diameter, so that the fiber is better characterized as a flexible light pipe.

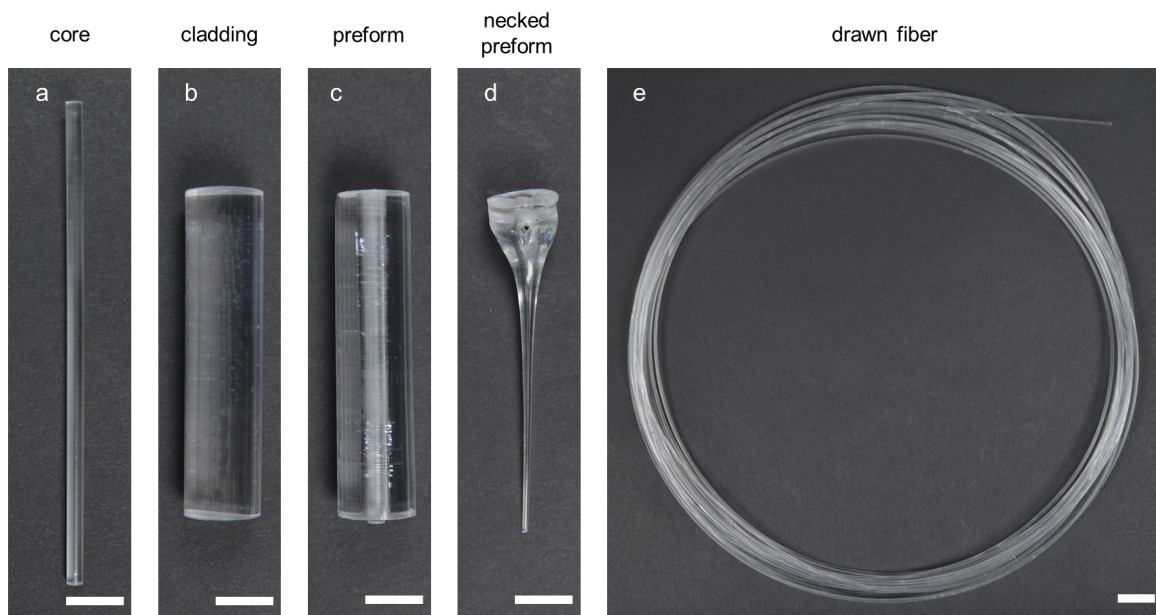


Figure 2.7: Photographs of the a) extruded PS core rod, b) extruded COP cladding rod, c) assembled preform, d) necked preform after the draw, and e) coil of drawn fiber.

COP granules are extruded into 15 mm rods using the large bore sleeve configuration and 16 mm die (Figure 2.7b). The cladding extrusion process begins with loading 20 g of COP pellets into the sleeve with the die installed. The ram and vacuum cap are fully retracted to permit top-loading of the sleeve into the heater block at room temperature. The end cap is then secured to the bottom of the sleeve. The ram and vacuum cap are then lowered so that  $\approx 20$  N are applied to the pellets in the sleeve. The vacuum cap is then sealed and mounted to the heater block via clearance holes in the flange at the top of the sleeve. With the end cap and flange secured, the melt chamber local atmosphere is controlled by degassing through the barbed vacuum. The chamber is pumped down to  $\approx 3$  mbar (absolute) pressure and heated to 185 °C. The sample dwells at that temperature and pressure for at least one hour to ensure uniform heating and softening. The ram is then lowered at 0.2 mm/s until the applied load on the sample reaches 1.33 kN, at which point motion is killed. This is the maximum recommended thrust delivered by the rod actuator, limited by the internal mechanisms of the gearhead and ball screw, so care must be taken to manually (or programmatically) shut off motion. With the PS compressed into a consolidated billet, the end cap is removed and chamber returned to atmospheric pressure by disconnecting the pump. In lieu of a pulling mechanism at the output of the die, a small weight ( $\approx 50$  g) is attached to the end of the rod at the onset of extrusion to ensure straightness of the extruded cylinder. However, constant tension applied by the weight requires compensation of the ram speed in order to offset necking and ensure diameter uniformity. With the parameters described, a ram speed of  $35 \mu\text{m s}^{-1}$  results in a 15 mm rod with  $< 50 \mu\text{m cm}^{-1}$  variation of outer diameter (OD) along the length. Of the initial 20 g, less than one gram of material remains inside the melt chamber and die.

Extrusion of the PS granules follows much of the same procedure as for the cladding with the 16 mm die replaced by the 3 mm die and bore-reducing sleeve configuration. The extrusion temperature is 185 °C as in the case of the COP cladding. Three grams of PS can be loaded into the reduced bore sleeve, resulting in small residual material loss on the order of tens of milligrams.

With a small weight (25 g) attached to the end of the rod, a ram speed of 10  $\mu\text{m/s}$  results in 3 mm extrudates of comparable uniformity as that of the larger diameter rods. An extruded diameter range of  $\pm 10\%$  above and below the die aperture diameter is feasible by varying the attached weight, ram speed, and temperature. Along with the 3 mm die, two additional dies were fabricated with aperture diameters measuring 1.5 mm and 4.5 mm. Extruded rods from these dies showed similar uniformity and reproducibility.

Assembling the preform begins with machining the extruded COP rod (Figure 2.7c). Both ends of the extrudate are faced on a lathe so that the overall length of the preform is  $\approx 75$  mm. Typically, several grams of material are machined from each end during this process. After facing each end of the cladding, the center is bored through from face to face along the cylinder axis at an ID that accommodates the extruded core diameter. The core is then inserted into the cladding, wrapped in PTFE tape, and consolidated above the glass transition ( $T_g$ ) in a vacuum furnace set to 150  $^\circ\text{C}$  for a duration of 45 minutes. The consolidation step serves the dual purpose of fusing the interface between the two materials without trapping air, and of desiccating the preform so that trapped moisture does not form bubbles when heated to the draw temperature.

Once consolidated, mounting holes are machined 3 mm offset from each end facet and orthogonal to the cylinder axis, four in all with two holes on each end of the preform (Figure 2.7d). Using small gauge steel wire, one end of the preform is tied to the metal pipe of the down feed mechanism in the BDT. At the other end, a 50 g weight is similarly attached but with sufficient length so that weight extends below the exit of the furnace. The fiber preform mounting rod is then secured into the lathe chuck and lowered into the furnace. The weight is then marked with a flag indicating the position prior to drawing.

Both furnace zones are then set to 150  $^\circ\text{C}$  for preheating of the preform. Preheating for at least 30 minutes is recommended to raise the background and baseline temperatures of furnace and

preform. Fiberglass insulation is placed at the entrance (top) of the furnace to mitigate upward air currents arising from the thermal gradient between the inside and outside of the furnace. Ceramic doors at the exit of the furnace serve a similar purpose as the fiberglass. Initiating the draw requires raising the temperature of the bottom (zone 2) to 280 °C while maintaining the top (zone 1) at 150 °C. Within a few minutes, the neck will begin to form, indicated by the downward movement of the flag on the hanging weight. The ceramic doors at the exit of the furnace are opened to permit passage of the preform bottom. The air-quenched drawn fiber that follows is then fed into the tractor pulling system that has been set to slow speed. Initiating the preform feed propagates the draw while ramping the pulling speed until the desired fiber diameter or DDR is achieved. In the case of a 15 mm COP cladding with a 3 mm PS core at the given process temperatures, setting the preform feed to 1.2 mm/min and the fiber pulling to 215 mm/min will yield a 1 mm fiber with  $\pm 50 \mu\text{m}/\text{m}$  diameter variation along the length (Figure 2.7e).

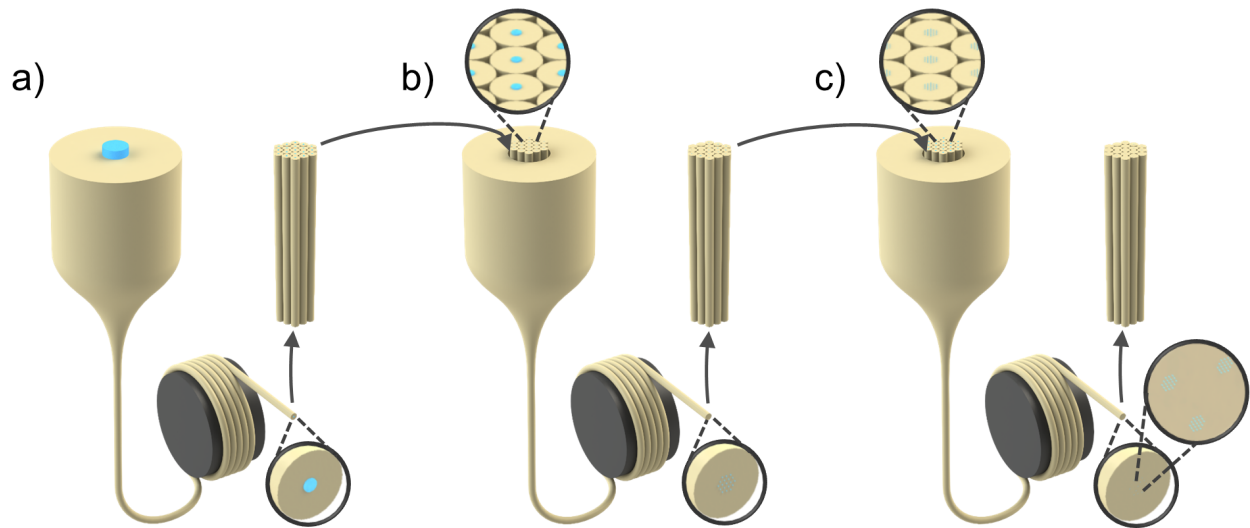


Figure 2.8: Schematic overview of the Stack and Draw process. a) A single core preform is drawn into fiber. b) One or more sections from the first draw are loaded into a new sheath rod to form the preform for the second draw. c) The process is repeated, with fiber sections from the second draw loaded into a new sheath rod. Additional iterations continue to geometrically reduce each core diameter until process instabilities limit the dimensions. Scale bars are 1 cm long.

The measured DDR provides accurate approximation for the core diameter in the drawn fiber. For the above, the expected core diameter is 200  $\mu\text{m}$  based on the ratio of preform to fiber outer diameter, and separately according to the initial relative dimensions in the preform. However, based on the process speeds and preform diameter and inputting into the DDR relation of Figure 2.4, the expected fiber diameter is 1.12 mm, larger than the actual fiber. This can be attributed to a slightly oversized drilled hole for the core during the preform construction. The effect of is that the COP cladding collapsed and filled the gap, leading to an overdraw of the outer wall down to a smaller diameter. The consolidation step sufficiently evacuated the gap of trapped air and was sealed from intrusion at the preform end, but the compression stress of the PTFE tape wrapped the outer surface was not enough to fuse the core and cladding throughout the middle section of the preform. Smaller core diameters can be achieved by employing the stack-and-draw technique whereby a new preform with the same cladding material is constructed with one (or more) section(s) of fiber from the previous draw, so that the core dimension is geometrically reduced by the DDR in each step. Figure 2.8 schematically depicts this process.

Fiber attenuation measurements were performed on the polymer optical fiber by coupling light from a 635 nm laser diode (Visible Diode Lasers, LLC) through an f/10 optical geometry into the 295  $\mu\text{m}$  core of a fiber drawn in the manner described above. The optical power, before and after the fiber, was measured using a power meter (Ophir-Spiricon, LLC: Model PD300). The fiber ends were polished by affixing the fiber to a jig and manually lowering onto rotating polishing paper with 300 nm grit. Accounting for Fresnel reflection at both facets, the attenuation of the fiber was 7.4 dB/m, equivalent to 18% of the incident power transmitted over 0.98 m length of test fiber. The loss is primarily attributed to intrinsic scattering in the PS core along with scattering due to particulate impurities trapped during extrusion and to dimensional modulations at the core/cladding interface.

The output profile of the fiber is recorded by imaging onto a CCD camera (Figure 2.9). The

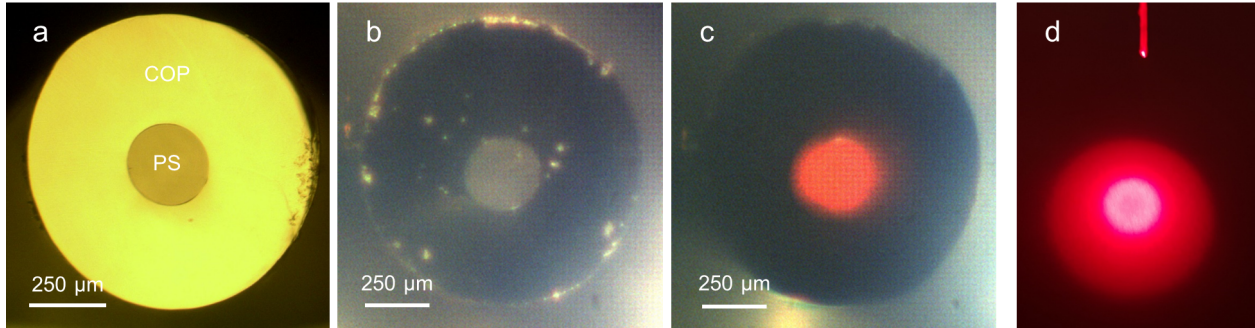


Figure 2.9: a) Reflection micrograph of the light pipe cross-section. The end facet was then imaged b) without and c) with the incoherent source coupled into the core at the other fiber facet. d) Photograph of the far-field output from the fiber on the benchtop.

fiber end is mounted to a 3D-stage and a spherical lens with  $f = 7.5\text{ cm}$  is positioned  $\approx 10\text{ cm}$  from the output facet. The camera is positioned  $\approx 30\text{ cm}$  from lens in an imaging geometry with 3x magnification. The facet is initially illuminated in reflection with a white light to adjust the contrast of the CCD output. A collimated incoherent beam ( $\lambda = 680\text{ nm}$  with  $FWHM = 7\text{ nm}$ ) is then coupled into the fiber core at the input facet. Coupling was achieved by mounting an objective lens with 10x magnification and 5 mm working distance to a 3D-stage, permitting fine-tuning of the focus onto the core. An incoherent source was selected for imaging the output to eliminate speckle due to higher order modes and scattering.

## 2.6 Case Study: High-Concentration Additive Doping

The ability to extrude rods for preforms containing high concentrations of additives was a pre-defined goal of the benchtop fiber fabrication system. Often, additives that impart technical functionalities are expensive due to limited availability, costly ingredients, or process-intensive synthesis. A recently developed methodology (discussed further in Chapter 5) for producing structured and functional spheres from multimaterial fibers provides a relevant and useful implementation to



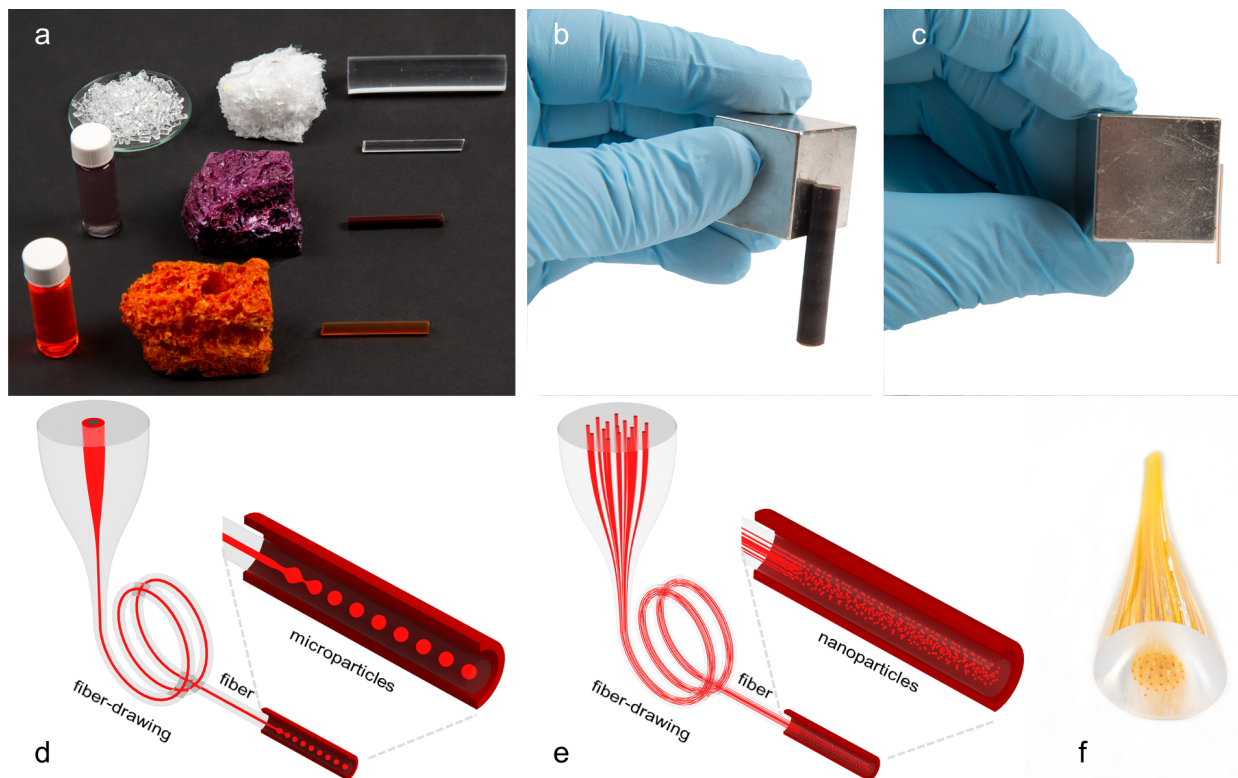


Figure 2.10: a) Photograph of the solution compounding process. A mixture of dissolved virgin polymer and additive (here, COP and two fluorescent dyes) results in a compounded foam after volatilizing the solvent in a vacuum furnace. b) Photograph of an extruded COP rod compounded with high concentration of magnetic nanoparticles. c) A fiber with a single micro-core still exhibits meaningful magnetic properties. More complex fibers are produced by structuring at the preform level. d) A schematic of a magnetic PS core is encapsulated with a fluorescent COP shell and drawn with PS sheath into fiber. The generated microspheres inherit the core-shell structure. e) Nanospheres result from stack-and-draw technique to geometrically reduce the diameter. f) Photograph of the necked preform depicted in e) with multiple cores.

test the ability of the benchtop system [52]. The ability to controllably compartmentalize functional additives such as fluorescent dyes, inorganic quantum dots, magnetic nanoparticles, or gold nanoparticles, among others, enables utility in a range of applications across the bio-medical [53, 54], chemical [55], and physical sciences [56, 57].

The process involves compounding the host polymer with the additive using an appropriate technique. For small batches, the best method identified involved dissolving the polymer to form a



smooth solution, mixing the powdered (insoluble) additive, agitating to promote good dispersion, and then volatilizing the solvent in a controlled atmosphere (e.g. vacuum furnace). The resultant compound typically adopts a foam morphology if volatilized under vacuum. The compound is then loaded into the BEX and extruded into a small diameter rod and assembled into a preform with a suitable sheath (cladding) for subsequent thermal drawing into fiber (Figure 2.10). Sphere fabrication follows by heating sections of the drawn fiber to unlock capillary instabilities at the sheath/core interface until the viscous core pinches off into a string of uniformly sized spheres. Selectively dissolving the sheath extracts the spheres from in the sheath. Centrifuging the resultant suspension isolates the spheres in a pellet. If desired, the sheath solution is substituted with fresh solvent, the pelleted spheres re-suspended, and then centrifuged, the process repeated until the desired dilution of sheath polymer is achieved.

The process described produces mono-structured spheres. Geometrically compartmentalizing multiple functionalities in a single sphere is achieved by constructing the radial and azimuthal architectures into the preform. Preform drawing reduces the dimensions while maintaining the relative geometry of these structures in the core which are then imparted on the generated spheres. To demonstrate this process, fluorescent dyes and magnetic nanoparticles were individually compounded into COP polymer and extruded into cylindrical rods. The rods were then machined or polished into axially continuous geometries including semi-circle, quarter-circle, and annular (tube) cross-sections. The rods were then assembled into a preform as a single core with a PS sheath and drawn into fiber. For radial structuring (multi-shell), the capillary instability governing the break-up into spheres requires finite surface energy between the layers, achieved by using including compounded PS intermediate layers, with the outermost layer comprised of a COP compound to retain the surface energy difference with the surrounding PS matrix. Characterization of some of these structured spheres is given in Figure 2.11.

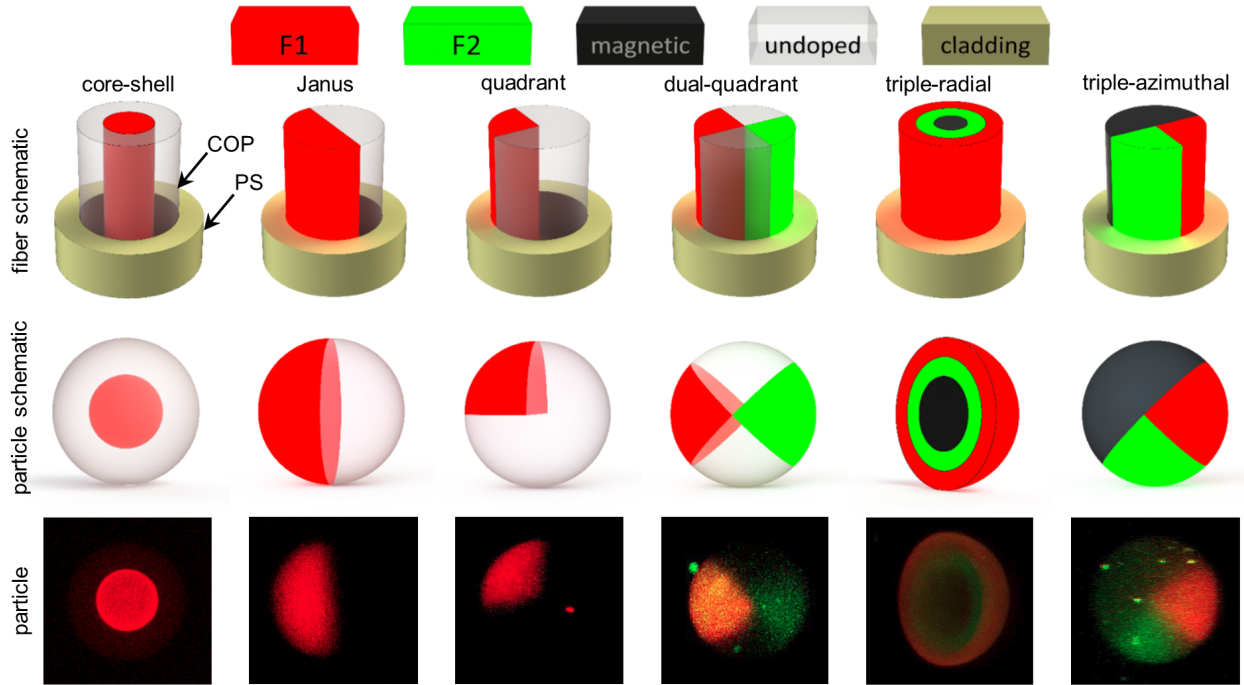


Figure 2.11: Schematics of the fiber structure, resultant particle structure, and confocal fluorescent microscopy micrographs of the extracted spheres following thermal drawing, capillary break-up, and extraction. Radially discontinuous structure with azimuthal symmetry (e.g. core-shell) require alternating the host polymer to ensure surface energy mismatch at the interface. Azimuthally discontinuous structures (e.g. quadrant) instead require the same host polymer.

## 2.7 Case Study: 3D-Printed Fiber Preforms

The complexly structured architectures constructed into the preforms in the prior section required subtractive mechanical processes to shape cylindrical rods into alternative cross-sections. In doing so, the material removed counteracts the design measures taken to minimize the unconsumed precursor during extrusion. An attractive complement to the benchtop drawing process would accordingly transition the multimaterial preform fabrication to a process that permits the construction of complex architectures directly in a single step. 3D-printing is an increasingly popular technique employed by hobbyists and scientific researchers alike to produce monolithic objects from raw material using computer-aided digital designs. The mechanical design of the printer limits the res-

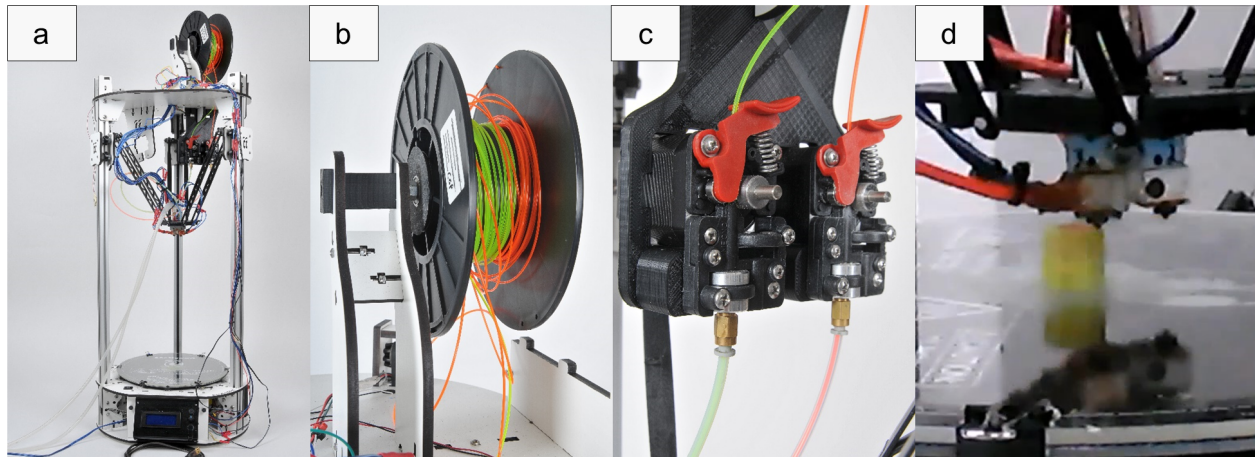


Figure 2.12: Photographs of the a) benchtop 3D-printer with dual-material extruder, b) custom filaments thermally drawn from ram-extruded compounded rods, c) mechanism for independent feed of each filament, and d) video still captured during dual-material print of a sheath-core preform with different fluorescent dyes in each region.

olution of the printed macroscale objects, typically on the order of  $20\ \mu\text{m}$  to  $2000\ \mu\text{m}$  with current commercially available technology. Such thermoforming style printers feed monofilament with millimeter-scale diameter into a small extruder mounted in a positioning scheme with at least two degrees of freedom in transverse motion. The printed object fills in volume by translating either the printer bed away from the extruder or by moving the extruder up and away from the bed.

Employing 3D-printing for multimaterial preforms fabrication necessarily requires that at least two different materials can be simultaneously processed (Figure 2.12). Such systems are commercially available as pre-built configurations, or as modifications to simpler single-material systems. Combining this capability with the modularity provided by the BEX additionally requires that the printer is equally compatible with filaments comprised of a range of materials, compounded or otherwise. Manufacturers typically service the needs of the general consumer and as such are unlikely to produce small batches of customized functional filaments for specialized technical research applications at a cost commensurate with the primary goal of cost-efficiency designed into the benchtop fabrication system. As such, a methodology was developed to produce these custom

filament.

Following the protocols established for extrusion of compounded rods, single-material preforms were drawn into fiber in a precursory step and subsequently fed into a dual-material 3D-printer as custom filaments. Although the 3D-printer extrusion temperature and feed rates are settable, poly-(lactic acid) (PLA) was used for the matrix polymer as standard process parameters are readily available. Examples of printed preforms and resultant spheres following capillary break-up are shown in Figure 2.13. The 3D-printed preform structures shown would otherwise require fabrication of custom dies using the standard benchtop methodology described whereby extruded rods are mechanically assembled into a preform. Each die would need to be the negative of the other in order to properly mate the two structures. This method would require multiple extrusion trials to account for die swelling and surface tension effects as the extrudate would likely exhibit deformations at vertices and axial bending due to uneven flow/pressure for asymmetric geometries. An alternative would be to fabricate a custom die for the core alone and then machine a solid sheath rod to mate with the extruded core geometry. However, for best results, the curved geometry would require first precisely measuring the extruded core (e.g. with CMM machine) and then using advanced (CNC) machining practices to ensure intimate mating between core and sheath. In either case, the time and access to resources required would counteract the overall goal of cost-efficient rapid-prototyping of complexly structured fibers. Although adding to the overall fabrication time, the precursory processing steps of first extruding and then drawing into custom filaments are generally completed in less time and at a reduced cost in comparison. That said, deploying the 3D-printer methodology only makes sense for fiber architectures that are too complex for subtractive machining, or for architectures that vary along the fiber axis.

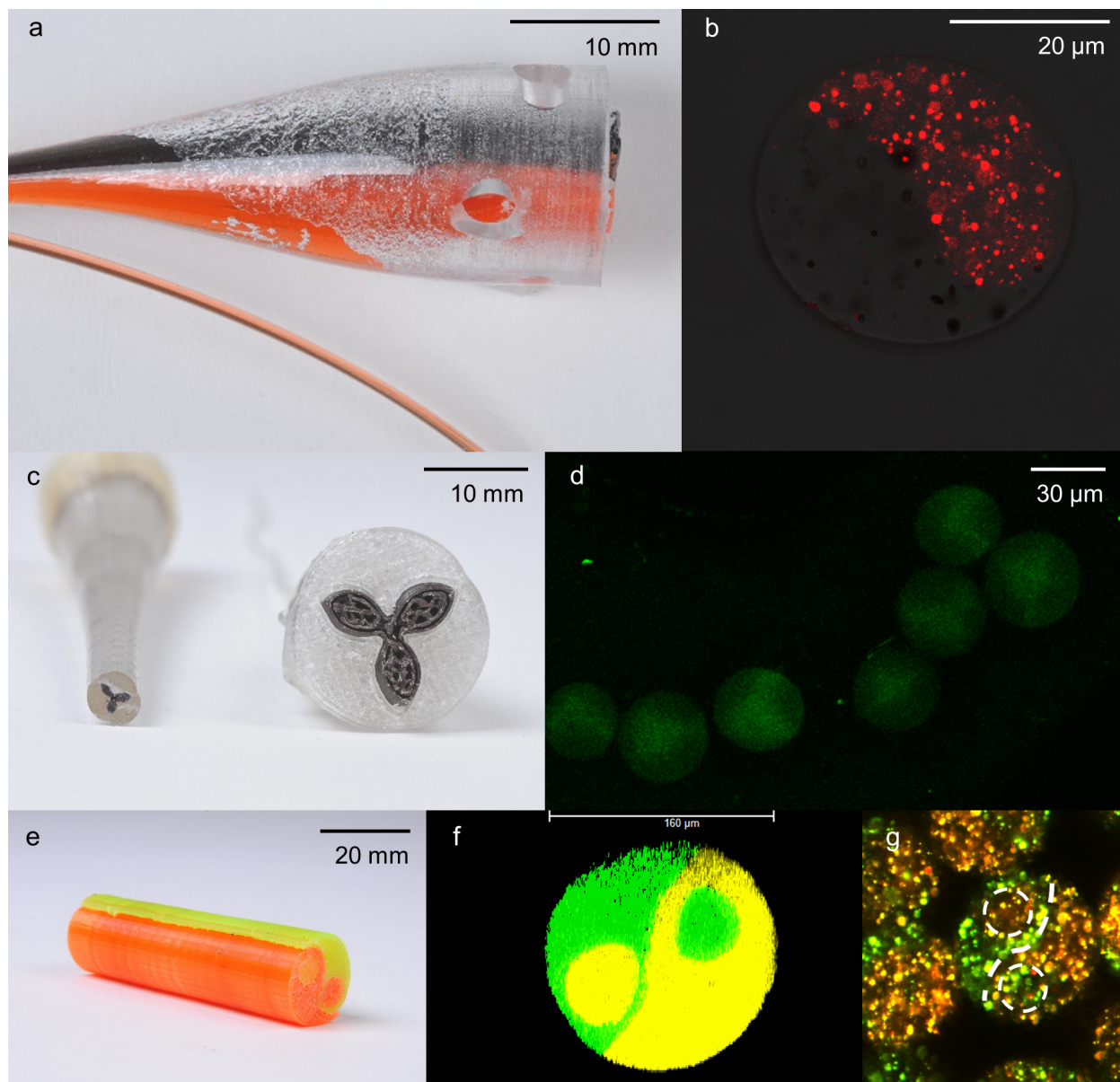


Figure 2.13: a) Photograph of drawn fiber with a PS sheath and 3D-printed Janus PLA core with a curved interface. The custom filaments are separately doped with magnetic nanoparticles and a fluorescent dye. b) Confocal fluorescent micrograph exhibiting fluorescence from the Janus fiber cross-section. c) Photograph of the drawn fiber tip (left) from a 3D-printed preform (right) with virgin sheath surrounding a "tri-lobal" fluorescent core. d) Micrograph of spheres extracted from fiber drawn from a second preform with a PS sheath and tri-lobal core. e) Photograph of a "yin-yang" preform 3D-printed from custom filaments doped with different fluorescent dyes. f) Micrograph of the yin-yang core cross-section after a second draw with a PS sheath. g) Micrograph of extracted spheres following the third draw depicting the intact yin-yang structure.

## CHAPTER 3: ROBUST MID-IR OPTICAL FIBERS

Chapter 2 established an efficient and rapid methodology for prototyping new fiber structures and material systems at a laboratory scale. Several case studies were discussed to validate the efficacy of benchtop equipment. Although these fiber examples were novel in either their specific material composition, structure, fabrication strategy, or combination thereof, they were however derivatives of previous efforts using traditional fabrication equipment since confidence in the validation increases when compared to existing functional systems. Now, with the benchtop system characterized, and the capabilities and limitations understood, future work can proceed with either fabrication of entirely novel fiber prototypes or by integration of the benchtop system with tighter-tolerance, scalable, and proven techniques. With the latter approach, fiber prototypes are closer to dissemination as reliable academic research tools or as commercial products. Presented here is such a fiber in which experience with thermal fiber drawing of polymer and chalcogenide glass is married with the tight tolerances and refinement of a commercially available product.

Optical fibers capable of handling high power with low loss and dispersion in the mid-infrared spectrum are of interest to many fields, including atmospheric sensing, thermal imaging, and nonlinear optics [58–63]. These mid-IR fibers require careful material selection and processing as only a small family of thermoplastics possess the requisite transparency window and control over refractive index to successfully produce the step-index profile for low-loss single-mode waveguide operation. Chalcogenide (ChG) glasses are among the materials used for fabricating such fibers as their transparency windows are quite broad, ranging from 1  $\mu\text{m}$  to 12  $\mu\text{m}$  depending on the chemical composition of the glass. However, fibers made from ChG alone inherit the mechanical properties of the glass and thus suffer from poor mechanical robustness which can limit their use in certain practical environments.



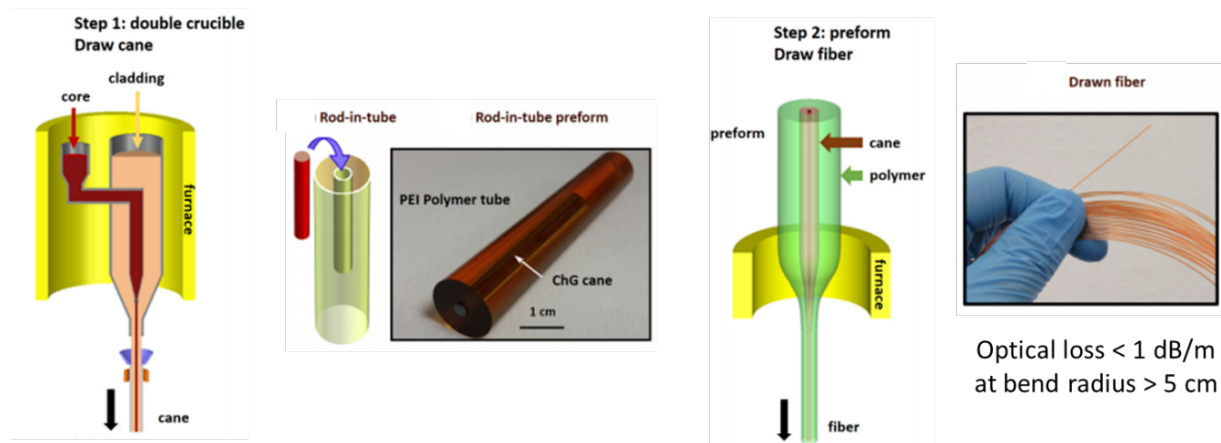


Figure 3.1: Overview of the hybridized fiber fabrication process in which a double-crucible is used to make the ChG cane and a thermal draw tower is used to make the fiber [64].

### 3.1 Hybridized Polymer/ChG Fiber Fabrication

To overcome this limitation, a hybridized fabrication strategy (Figure 3.1) was developed in which a high-purity step-index-profile ChG glass rod is co-drawn with a polyetherimide (PEI) jacket thereby enhancing the mechanical strength of the resulting fiber [64]. The modularity and flexibility of the approach enabled integration of the fiber with downstream processes in a manner not otherwise supported by traditional optical fibers developed for mid-IR transmission. In particular, the methodology combines the mechanical strength and chemical properties of the thick PEI jacket with the superior glass purity and dimensional control of commercially available ChG fibers produced using a double-crucible extrusion system. Although these commercial fibers currently feature a polymer coating for added mechanical support, they are limited in the type of polymer and the thickness of coating that can be readily applied as an in-line processing step. This coating process is itself adopted from the manufacture of traditional silica optical fibers for telecommunications, and thus imparts a similar level of added strength. However, ChG has comparatively much less tensile and flexural strength as compared to amorphous silica and so the coated fibers do not possess the same level of resilience to operational and environmental conditions.

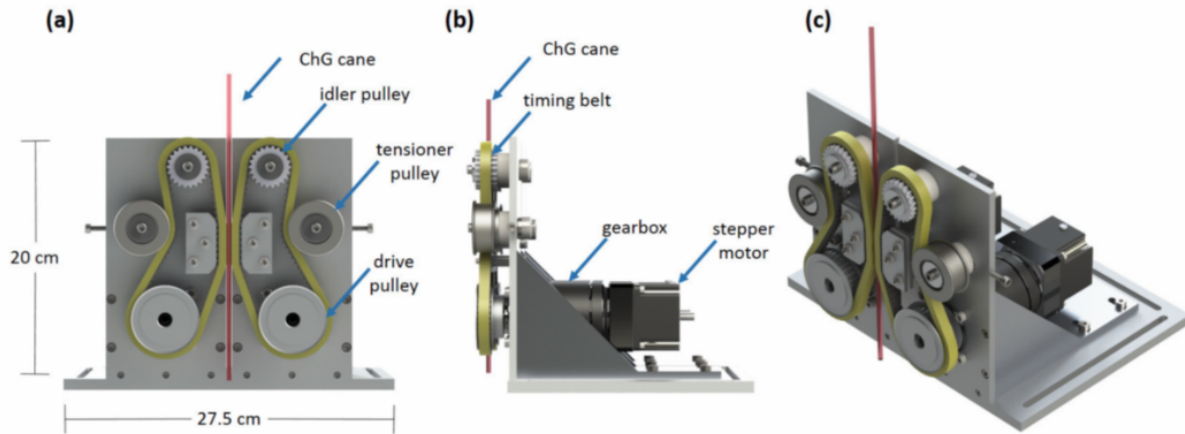


Figure 3.2: (a) Front view, (b) side view, and (c) 3D view of the cane puller used to maintain constant cane diameter and straightness during drawing from the double-crucible furnace. The system consists of two synchronized stepper motors, a gearhead to achieve torque and speed requirements, in addition to soft belts which grab the cane and pull it on it at a very low speed of  $\approx 0.5$  cm/min to 1 cm/min. [64]

The ChG core and cladding rod (cane) was produced using a quartz-glass double crucible loaded into a fiber drawing furnace. The compositions were  $As_{39}S_{61}$  for the core and  $As_{38.5}S_{61.5}$  for the cladding, resulting in a numerical aperture (NA) of 0.2. Once the ChG reached process temperature, pressure was applied to the melts and adjusted to achieve the desired core/cladding diameter ratio in the cane. The cane is initially pulled into fiber at high speed which is then smoothly reduced to increase the diameter to the target range of 2 mm to 3 mm. Simultaneously, the process temperature was reduced  $10^{\circ}C$  to  $15^{\circ}C$  thereby increasing melt viscosity and minimizing capillary fluid instabilities. Temperature adjustments were needed at the beginning of the process to ensure that the cane viscosity allowed it to hold its own weight. Diameter variations (minimum-to-maximum) were less than 10% after establishing crucible temperature, core and cladding pressures and pulling speed.

Producing cane diameters ten times that of typical fiber diameters using the same manufacturing equipment required reducing the pulling speed by at least two orders of magnitude, as dictated by the DDR calculation discussed in Chapter 2.3. The speed requirements fell outside of the



limits of the equipment, which therefore necessitated the design and manufacture of a specialized ‘cane-puller’. The cane-puller (Figure 3.2) consists of two synchronized stepper motors, a 100:1 gearhead for torque and speed requirements, and timing belts with robust sponge foam to grab the cane and pull on it at a very low speed of  $\approx 0.5$  cm/min to 1 cm/min with step resolution of  $\approx 400$   $\mu$ m/min. All of the components were specified individually, imported or mocked up in SOLIDWORKS®, and subsequently assembled into a full system. Custom idler pulleys were built with low friction, press fit bearings assembled into machined timing pulley stock to mitigate transferring vibration onto the cane. Precision spacers were used to precisely locate the mid-plane of the belts to coincide with the axis of the double-crucible. Transverse adjustment of the mounting plate was included to accommodate unanticipated misalignment as the system was designed at CREOL and then shipped to industry collaborators for installation into their production system. Dowel pins and tolerances were incorporated into the support structures for added precision over the transverse and angular positioning of the various components with respect to the cane axis.

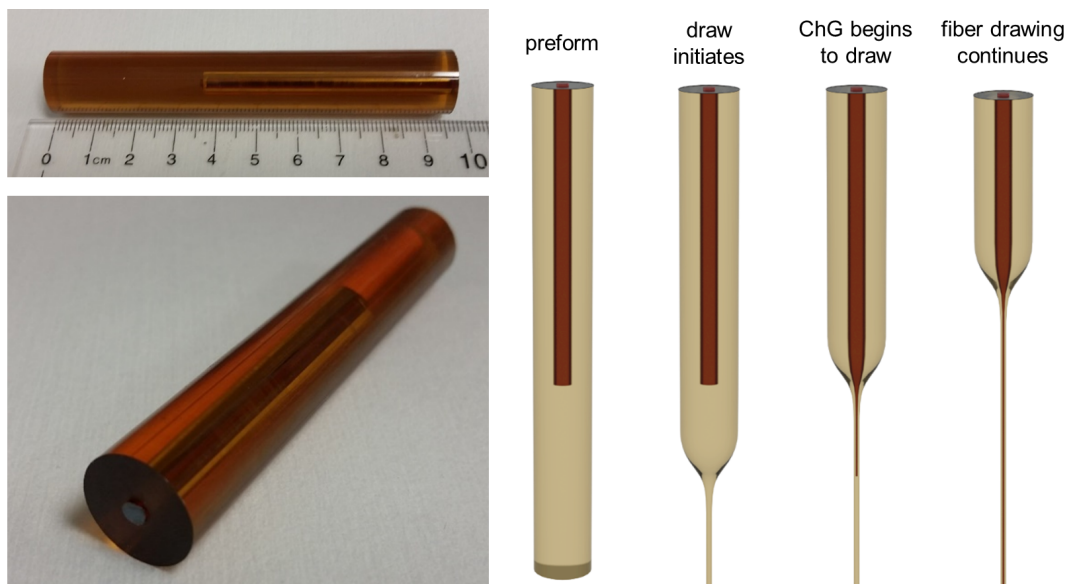


Figure 3.3: (Left) Photograph of the extruded PEI rod with machined facets and center-bore followed by assembled preform with ChG cane. (Right) Schematic depicting the draw highlighting the initial location of the neck below the cane to maximize useful fiber length.

With the ChG cane fabricated to the appropriate relative core/cladding dimensions for either single-mode or multi-mode operation, the next step involved preparing the preform for subsequent thermal drawing (Figure 3.3). PEI pellets were loaded into the BEX system (Chapter 2.2) and extruded into a 15 mm diameter rod. The rod was next machined into a stepped tube and the ChG cane then assembled into the bored rod. PEI was selected for its thermal compatibility with the ChG cane and for its robust mechanical properties, both of which were previously validated [65]. The fibers were next drawn in BDT system with the first (second) zone was held at 250 °C (380 °C), and drawing speeds up to 50 cm/min were employed to produce PEI-jacketed fibers with a core diameter in the range of 10 μm to 12 μm. Using these parameters, 20 m of useful fiber were drawn from a 6 cm long, 3 mm diameter ChG cane. Although not able to provide the level dimensional stability and in-line measurement capability of the traditional polymer draw tower located at CREOL, the BDT was nevertheless capable of producing enough control over fiber properties to permit the at-present record-high power handling capabilities and low-loss transmission results presented in the following sections. Moreover, the miniaturized scale of the BDT actually increased the yield of usable drawn fiber produced, in that nearly all of the cane was consumed and drawn into fiber due to the better matched furnace dimensions and temperature profile compared to that of the larger tower. Figure 3.4 depicts characterization of the drawn fiber cross-section.

### **3.2 Low-Loss Transmission with AR Coatings**

The optical and mechanical properties of the PEI/ChG fibers were then probed in a few experimental schemes. In a first effort, as SWIR and MWIR sources continue to demonstrate higher output powers with improvements in beam quality, it was of interest to characterize the transmittance through the fibers. Although providing a low-loss transparency window through the spectrum of interest, ChG additionally exhibits relatively high refractive index. This accordingly leads to high

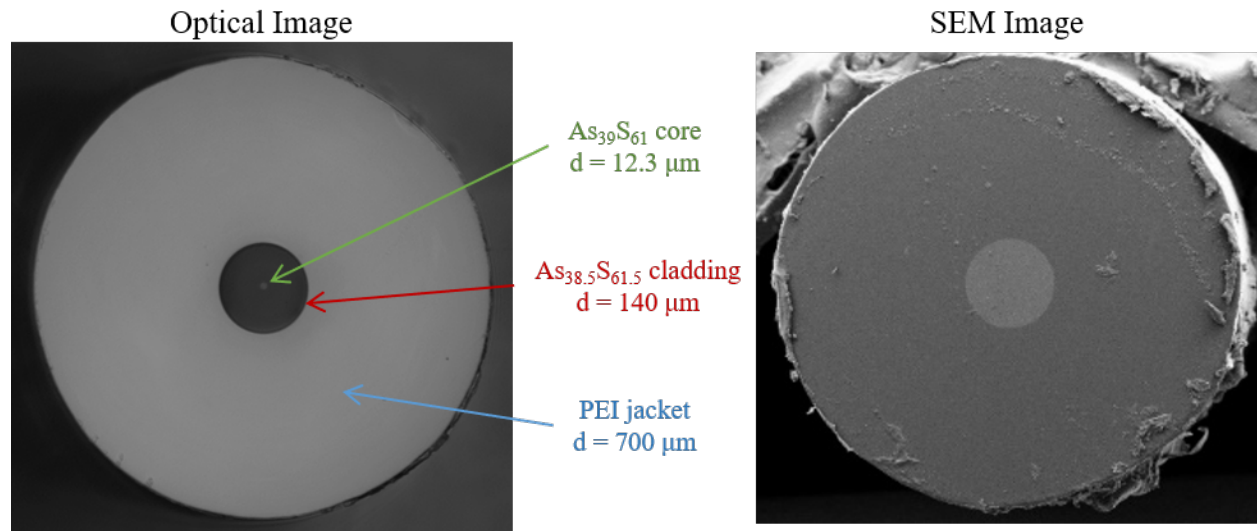


Figure 3.4: (Left) Reflection micrograph with a low-power 1550 nm source coupled into the fiber core. The jacket and cladding diameters were measured directly, while the core diameter was calculated from the preform ratios. (Right) SEM micrograph of the same fiber facet.

reflection losses at fiber facets in similar ChG optical fibers. A straightforward optical solution to reduce the reflection losses is application of a dielectric coating as is commonly done in numerous applications. However, the typical oxide materials and coating processes have proven difficult to adapt for use on bare ChG fiber facets. The mismatch between thermomechanical properties, in particular thermal expansion, and of the relative surface chemistry leads to delamination and fracturing of the coating. This in turn can exacerbate failure mechanisms by focusing incident energy into higher intensities.

This limitation was overcome with the hybrid fibers by utilizing the large majority of the cross-section area occupied by the PEI jacket. Standard evaporative vapor deposition technique was used to apply a single-layer of alumina with a coating thickness selected to minimize loss at the experimental wavelengths. Adhesion of the coating was enhanced by the elastic properties of the PEI whereby the thermomechanical stresses were distributed and mitigated compared to bare ChG fiber. The large surface area additionally provided suitable substrate for the alumina so that

AR Coating	Calculated/%	$\lambda_0 = 1.55 \mu\text{m}$	$\lambda_0 = 1.95 \mu\text{m}$
		Experimental/%	Experimental/%
none	67.8	$65.7 \pm 1.0$	$63.0 \pm 3.0$
entrance facet only	82.3	$80.0 \pm 1.0$	$78.0 \pm 3.0$
both facets	100	$97.7 \pm 1.0$	$98.0 \pm 3.0$

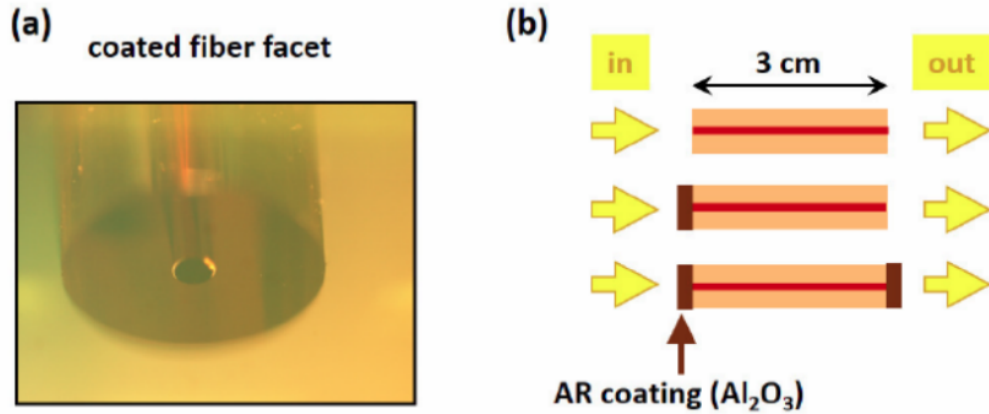


Figure 3.5: (a) Optical micrograph of the fiber tip with a single layer, quarter wave, anti-reflection  $\text{Al}_2\text{O}_3$  coating. (b) Diagram of fiber transmission measurements.

the aspect ratio of thickness to area further inhibits brittle fracturing as the coating relaxes and cools. This is analogous to the bend radius decrease exhibited by brittle materials such as silica optical fibers when drawn into small diameters with large length. The surface chemistry of the PEI polymer as well contributed favorably; in fact, PEI is often deployed as a bed for 3D printers due to its advantageous adhesive properties coupled with mechanical strength and temperature resistance. Characterization of the coating mechanical strength is described in Figure 3.5 with optical efficacy measurements of the AR coatings printed in Table 3.1 [64].

Low-power CW coherent light was then coupled onto the coated fiber facets at three wavelengths:  $\lambda = 1.55 \mu\text{m}$ ,  $1.95 \mu\text{m}$ , and  $4.55 \mu\text{m}$ . Transmission losses measured  $< 1.1 \text{ dB}$  through meter-long fibers not including remaining reflection losses at the fiber facets. Figure 3.6 depicts detailed experimental results at for the  $1.95 \mu\text{m}$  case [64]. The beam profile at the fiber output maintained

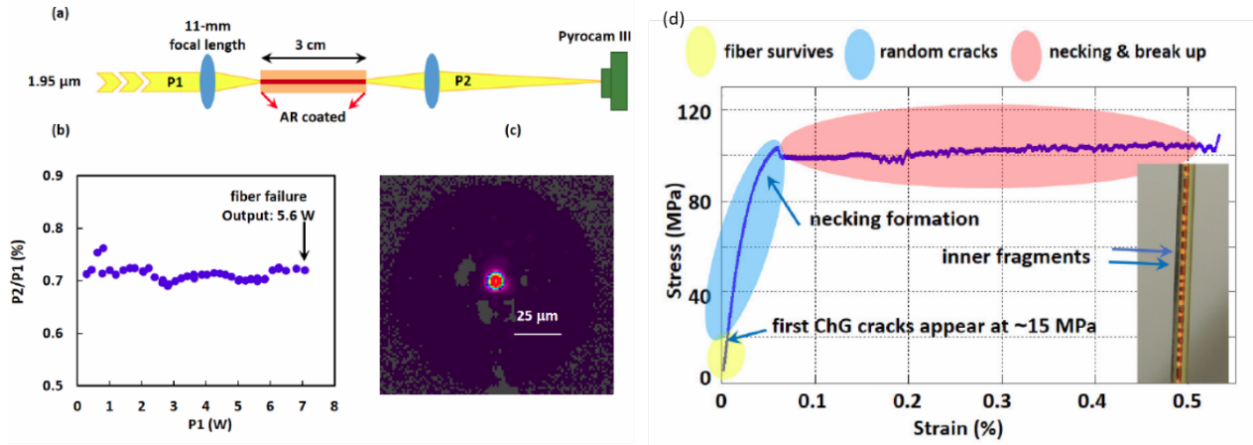


Figure 3.6: a) Experimental setup schematic of fiber transmission measurement at  $1.95\ \mu\text{m}$ . b) Measurement of the output (P2) to input (P1) power ratio. c) Output beam profile captured with Pyrocam III at a power level just below damage. d) Measurement of fiber tensile strength. Inset photograph depicts fractured ChG glass upon cold-drawing of the PEI jacket.

excellent single-mode profile throughout all input powers launched. Measurement of the optical fiber tensile strength was shown to be enhanced by a factor of 1000 when compared to bare ChG fibers without a PEI jacket. Additionally, interruption of the transmitted optical power was shown to coincide with the tensile yield stress of the jacket at which point the jacket undergoes plastic deformation in a process known as *cold-drawing*. As shown in the plot inset, the brittle ChG glass fractures into uniformly sized rods, the lengths of which are related to the Young's modulus of the glass and the initial diameter prior to break-up. This interesting phenomenon was investigated in detail by Shabahang et al [65].

### 3.3 High-Power Transmission

In a second effort, power handling capabilities were tested empirically at 2053 nm, 2520 nm, and 4102 nm. Transmission of  $>10\ \text{W}$  with the 2053 nm source was demonstrated with AR coatings applied to the facets of a 20 cm long fiber (Figure 3.7) [66]. At the time, this was believed to be

highest CW power delivered at that wavelength through a single-mode ChG core fiber. However, the AR coatings were also shown to be the primary failure mechanism via cracking after exposure to high power. Fibers with no coating survived intensities of  $\approx 12 \text{ MW/cm}^2$  without failure.

Inspired by the high-power transmission measurements, additional testing was performed to better characterize the failure mechanisms with respect to power and intensity incident on the fiber facets. If coatings are avoided, or beneficial micro-structuring applied, the primary limitations were determined to be SBS, SRS, and thermal failure, the characteristics of which were modeled with simulations. Overall, SBS was concluded to be the prime factor limiting power handling of single

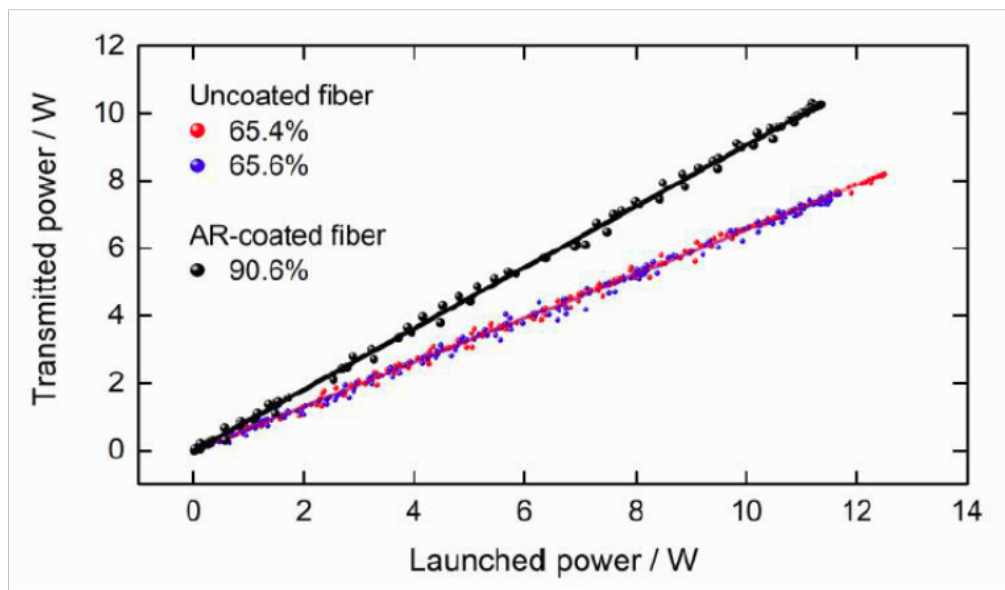
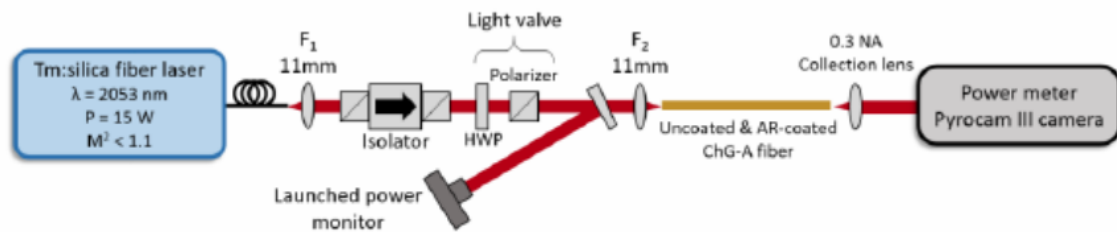


Figure 3.7: (Top) Experimental setup for high power coupling of a 2053 nm source into a hybrid fiber with no AR coating. (Bottom) Measurements yielded  $>90\%$  transmission and 10.3 W delivered with AR coatings applied.

frequency beams in single-mode ChG fibers that are more than a meter long. For example, SBS will limit power handling to  $\approx 1$  W through a 1 m length of fiber, but can be avoided by using a spectrally broad source. For broadband sources, power handling is limited by either heating effects or SRS; which one is dominant depends on the details of incident power, passive loss, core size, wavelength, and heat transfer rate [67].

### 3.4 Efficient QCL Coupling

Advances in commercial quantum cascade lasers (QCL) systems over recent decades has been met with renewed interest from researchers seeking to implement high power outputs in the MWIR spectrum [68, 69]. However, the characteristic large divergence of single emitters like QCL sources typically inhibits their utility in many free-space applications. The ability to efficiently couple QCL

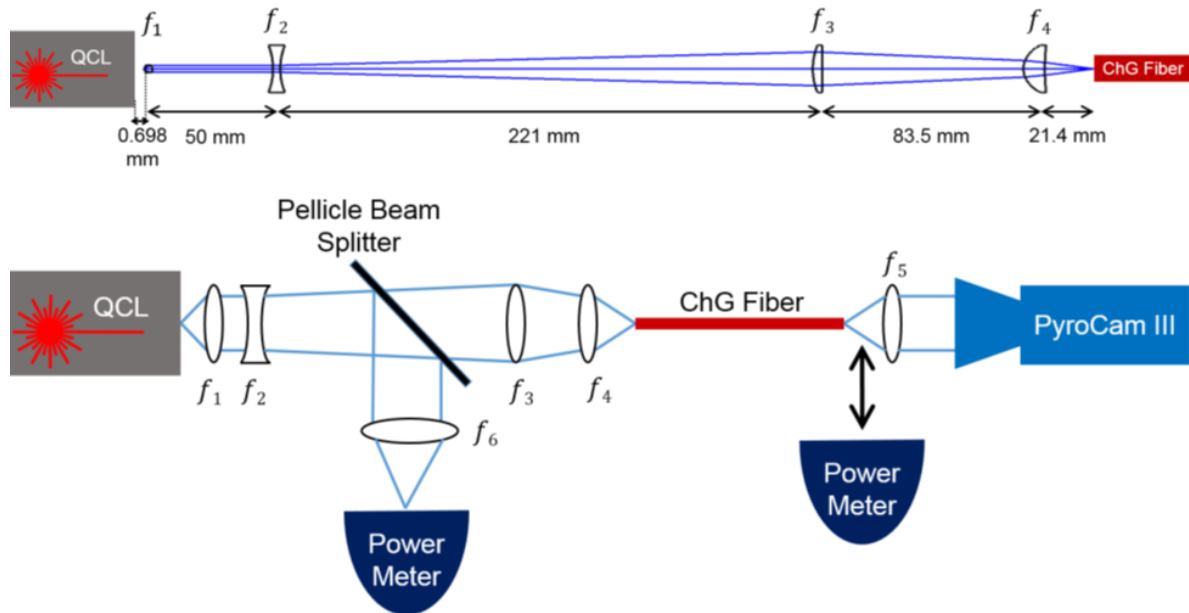


Figure 3.8: (Top) Optimized layout of the QCL coupling system. (Bottom) Overall setup including input/output power monitoring and output coupling scheme. Focal lengths for lenses  $f_1$  through  $f_6$  are 1.873 mm,  $-50$  mm, 100 mm,  $-40$  mm, 37.5 mm, and 40 mm, respectively.

outputs into low-loss, robust, and flexible optical fibers would overcome this limitation, potentially enabling new applications in the defense, sensing, and medical industries. Strategies for delivery of QCL outputs through optical fibers have thus far relied on either hollow core structures or highly multimode fibers [70–74]. Although hollow core fibers can deliver near fundamental mode outputs, high losses are often incurred due to contamination. In contrast, typical large-diameter solid-core fibers are easier to fabricate but deliver poor mode quality due to large V-numbers. An optical fiber with a low-loss transmission, a solid core, and single-mode beam output, such as the hybrid fibers described here, would represent an attractive vehicle for QCL delivery.

Accordingly, Zemax® modeling was employed to solve for the optical setup geometry and lens shape that would maximize the free-space coupling efficiency of a QCL into the hybrid PEI/ChG fibers [75]. The results from the modeling were then experimentally validated (Figure 3.8) with more than 160 mW at 4550 nm was coupled into a 12  $\mu\text{m}$  core with near single-mode excitation. With AR coatings on both facets,  $\approx 89\%$  transmission was measured through the fiber with  $>70\%$  of the QCL output coupled into the core (Figure 3.9). These combined represent excellent results considering the mismatched numerical apertures between the QCL source (0.82) and fiber (0.2).

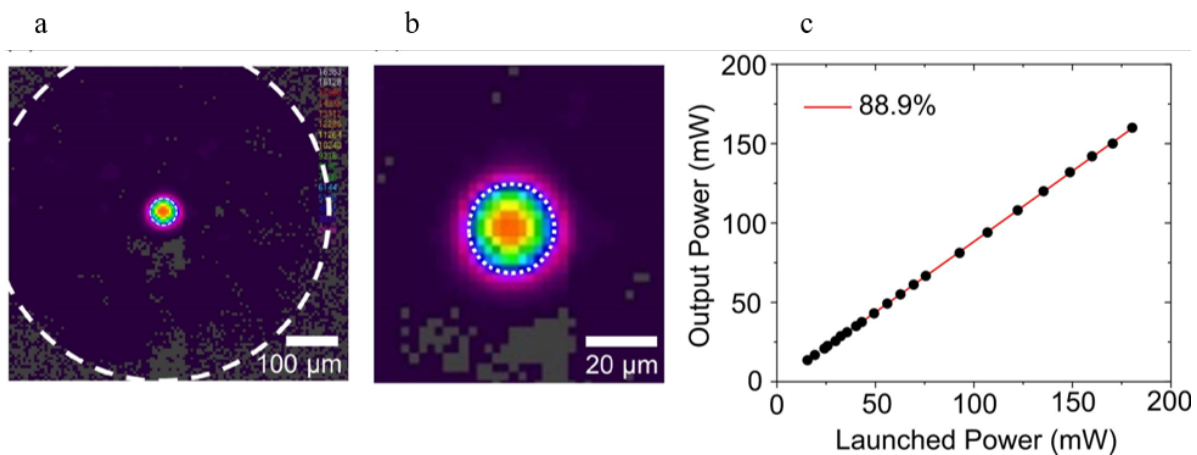


Figure 3.9: a) Pyrocam capture of the transmitted mode profile with dashed line corresponding to ChG cladding/PEI jacket interface. b) Zoomed view of the core mode profile with dotted line indicating core/cladding interface. c) Measured output power versus launched power.



## CHAPTER 4: MONOLITHIC OPTOELECTRONIC FIBER DEVICE

Electronic devices are at the cornerstone of modern technology, touching every facet of research and industry alike. Integrated circuit devices enable transformative medical breakthroughs; change the way society ingests, digests, senses, and interacts with our surroundings; and, deliver energy, resources, information, and connectivity across thousands of kilometers over imperceptibly short timescales. These devices are packaged in a wide variety of form factors, with varying degrees of complexity, size, and combination of materials. The past few decades have witnessed Moore's Law march steadfastly towards an inevitable convergence, itself likely to inspire the next paradigm shift in industrial manufacturing. As the transistor size approaches the atomic scale, researchers have been increasingly motivated to innovate alternative architectures and implementations to squeeze more function and processing power from the same family of devices. One such branch of study aims to discard with the rigid, brittle semiconductor substrate in favor of light-weight, flexible, and equally scalable form factors. From experience with textiles and telecommunications, fibers emerge as an attractive substitute for the two-dimensional wafers and devices that dominate the current market. The primary challenge hindering this effort has been designing fiber systems and scalable fabrication methodologies that combine the "triumvirate" electronic properties of the insulator, conductor, and semiconductor into a flexible monolithic package without also sacrificing performance, low-cost, and ease of integration.

Multimaterial fiber technology has grown substantially in recent years and presents as a potential solution to the flexible electronic dilemma (Figure 4.1). Thermoforming techniques dominate the literature as they are the most commonly deployed strategies for commercial production of simpler sheath/core structures and single-material fibers. In the case of the photonic crystal fiber, for example, itself classified as a single-material fiber, the fabrication followed fairly directly from the well-established and well-characterized optical fiber manufacturing technology with the ingenuity

of the PCF arguably contained in the translation and analytical description of the photonic crystal lattice in the context of a cylindrical fiber. The development of the PCF into more sophisticated structures with tighter dimensional stability enabled a new adaptation whereby "hole-y" fibers, now commercially available products, could be modified with a post-fabrication treatment into a multimaterial structure by impregnation [76–78]. This class of sequential, hybrid manufacturing indeed produces a monolithic structure, however the additional fabrication step operates on a finite length of drawn fiber and so does not readily permit scaling to a production-style, long-length manufacturing scheme. An example of this approach produced a Schottky diode junction in fiber by HPCVD deposition of n-type silicon with a platinum electrode. However, applying the second electrode to complete the device required carefully deploying a focused ion beam (FIB) to etch and then deposit additional platinum region on the fiber tip [79]. Although it produced a working optoelectronic device, the methodology again is impractical to scale as it requires highly specialized equipment and techniques, is sensitive to impurities, and only produces finite length batches from existing fiber precursors.

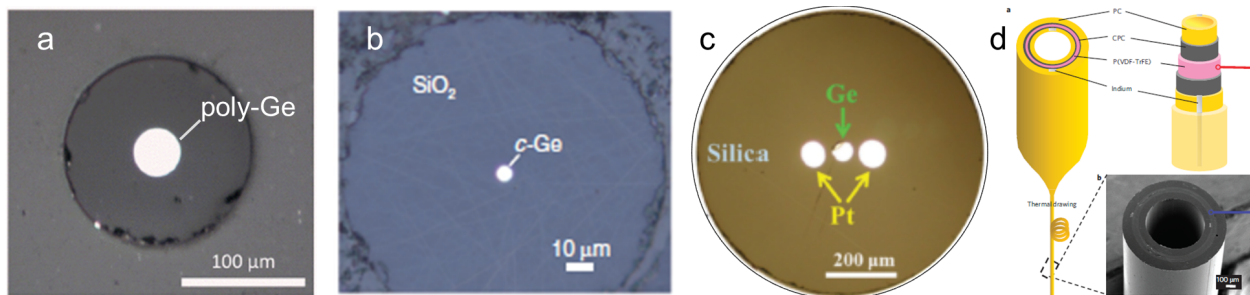


Figure 4.1: Review of Metal-Insulator-Semiconductor fiber strategies. a) Thermally drawn fiber with a glass sheath and polycrystalline Ge core highlights successful dimensional control despite viscosity mismatch [80]. b) Single-crystal Ge core fabricated by HPCVD in a previously drawn hollow glass fiber highlighting ability to control crystallinity [81]. c) Thermally drawn fiber with axially continuous metallic conductors and Ge core. This core underwent axial break-up via capillary instability forming electrical junctions at discrete locations along axis [82]. d) Thermally drawn low- $T_g$  fiber with low viscosity regions separated by electrically conductive amorphous compound. Suggests a strategy for transitioning to higher process temperatures [22].

Whereas the previous strategy incorporated electronic materials into previously drawn fibers, the next class encompasses efforts to co-draw three distinct triumvirate materials into a monolithic device in one fabrication step. Early work successfully produced working devices combining low glass transition temperature ( $T_g$ ) polymer insulators and ChG glass semiconductor with low melt temperature (low- $T_m$ ) metal alloy conductors into a single preform and co-drawn into fiber [83–89]. However, ChG is a weak semiconductor with electronic properties that are difficult to predict, and so these devices are limited in their performance and modularity. Traditional semiconductors, on the other hand, transition to molten states well above 550 °C due to their crystallinity and are as such incompatible with these low- $T_g$  polymers that readily degrade and volatilize at these temperatures [90]. Crystalline materials additionally exhibit rapid transitions to low viscosity upon melting which imposes further restrictions in that drawing from a preform in which two or more crystalline phases are in intimate contact would consequently result in mixing thereby disrupting the structural and electronic integrity of the device.

Consequently, efforts to incorporate crystalline materials into drawn fibers at high process temperature have only proven successful for preform architectures with disjoint crystalline phases separated by viscous amorphous barriers. For instance, crystalline silicon was first successfully drawn as the single-core of a silica cladding only a decade prior [91], but efforts since to connectorize axially continuous conductors on the semiconductor have required breaking axial continuity of core [92]. In other work, a multiplicity of axially continuous crystalline metals were successfully drawn in high-temperature processes, however the semiconducting element of these fibers was not incorporated [93]. Accordingly, thermally co-drawing traditional electronic materials directly into a monolithic fiber requires a novel strategy to overcome mixing of the crystalline phases while preserving the advantageous structure and electrical pathways of the device (Figure 4.2).

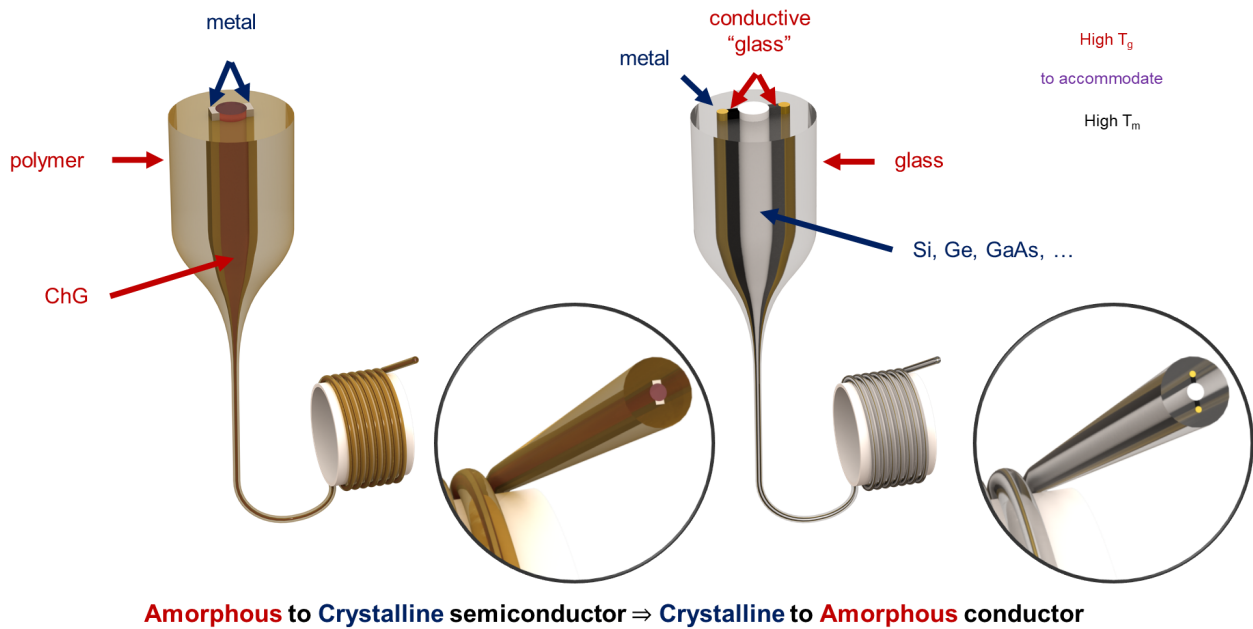


Figure 4.2: Schematic detailing the motivation behind development of an amorphous conductor. In prior work, low-temperature materials (polymer, tin, and ChG) were co-drawn into an electronic device. Prior work with crystalline materials at high temperature suggests that substituting ChG for a traditional semiconductor requires an electrically conductive viscous barrier to prevent mixing during the draw.

#### 4.1 Electrically Conductive Composite Glass

The ability to structure a glassy, high-temperature, and electrically insulating preform with disjoint, axially continuous conductive and semiconductive crystalline phase while maintaining in-fiber conduction would produce a thus far elusive fiber with potential utility in a wide range of applications seeking flexible and robust device platforms. So, addressing directly the inability to preserve preform architecture through the draw if two or more crystalline phases are in contact, a fabrication strategy was developed and executed involving the introduction of a fourth material class into the preform. In order to best assure successful co-drawing into a monolithic fiber, the new class should exhibit, at the minimum, sufficiently high electrical conductivity, sufficiently high viscosity at compatible draw temperatures, exhibit compatible thermomechanical expansion

to minimize stresses during quenching, preserve glassy (amorphous) properties from preform to fiber, and present an immiscible and axially continuous viscous barrier to the crystalline phases.

Comparing these requirements to the properties of the insulating glass matrix, only the electrical conductivity would need to be enhanced in order to satisfy all conditions. To that end, an electrically conductive composite glass was fabricated and characterized. Glasses offer a unique set of mechanical and optical properties that underlie their wide-spread utilization in everyday commodities, and are typically electrically insulating [94–96]. The strength of glasses in conjunction with thermoforming processing in addition to low density and cost facilitate their utilization in

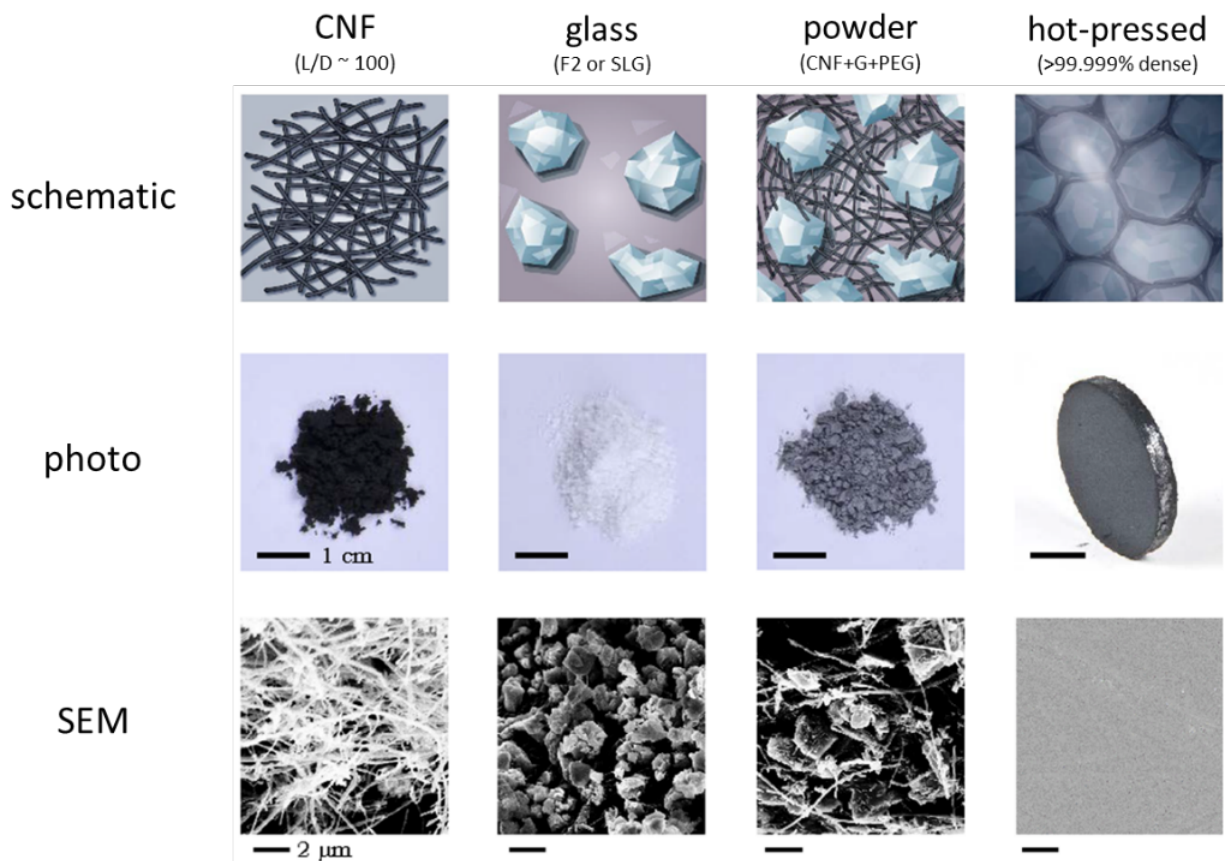


Figure 4.3: Overview of the conductive composite fabrication, shown in schematic, photograph, and SEM at various stages of the process. The raw materials are dry-mixed into a powder that is then hot-pressed into a densified solid.

large-area windows, enables thermal drawing into extended fibers for optical telecommunications, in addition to their use in utensils, screens for electronic devices, and decorations. The most widely used oxide glasses are extremely poor conductors featuring conductivity on the order of  $10 \times 10^{-15}$  S/m to  $10 \times 10^{-10}$  S/m [97]. Developing an electrically conductive oxide glass would have significant applications in novel multimaterial electronic fibers. The higher density and thermal expansion coefficients of metals preclude their utility in such applications, while the operating and processing temperatures of conductive polymers are too low.

A ceramic-inspired process called *sintering* was exploited to produce highly conductive bulk oxide glass loaded with CNFs (see Figure 4.3). The aim was to form a composite that features the mechanical properties of glass, including strength and thermoformability, while also exhibiting high electrical conductivity at room temperature. Composites with different surfactants, loading concentrations, and CNF aspect ratios were synthesized to determine the optimal combination that would provide sufficient electrical conductivity while not detracting from the other aforementioned advantageous properties. At high temperatures and long exposure time, certain compositions were shown to exhibit unfavorable behavior attributed to the CNFs chemically reacting with the surrounding glass matrix. This behavior was identified and characterized by producing densified bulk samples and subjecting them to thermal treatment in a controlled environment. For some compositions, the adverse effects were clear, with samples exhibiting evidence of volatile reactions in the form of porosity and trapped bubbles throughout the volume. It was determined that certain glass chemical compositions were broadly incompatible with CNFs at elevated temperatures independent of the loading fraction or surfactant.

A key discovery during the development coincided with the trade study over the type of surfactant used to uniformly disperse the CNFs throughout the composite. It was shown that high conductivity could be achieved even with CNF loading fractions at or below than predicted percolation threshold. This was determined to be a consequence of using low molecular weight organic sur-

factants. Upon thermal treatment near the glass softening temperature, the organic polymer would carbonize *in situ* and, if well dispersed throughout the composite, consequently boost the background conductivity of the surrounding matrix. In effect, this would enhance the tunneling conductivity for neighboring but disjoint CNFs while likewise enhancing the percolation efficiency for networked CNFs. Using this approach, an amorphous composite with thermoviscous behavior intact was produced with record high bulk conductivity measured.

## 4.2 Design and Construction of an Intermediate- $T_g$ Draw Tower

Fabrication of these electronic fibers comprising predominantly intermediate- $T_g$  oxide glasses required the design and manufacture of a new thermal drawing tower (see Figure 4.4). The tower features a single-zone tubular furnace with a heated length of 37 mm along with unheated adiabatic zones 15 cm and 10 cm long above and below the heated zone, respectively. The furnace bore accommodates preform diameters up to 30 mm, and can achieve stable draw temperatures up to 1100 °C. The preform is fed into the furnace using a slide table attached to ball-screw linear positioner. The screw is driven by an 8000 count/rev servomotor with a 100:1 gearbox to achieve a minimum linear speed of approximately 0.5 mm/min and a resolution of 2  $\mu\text{m min}^{-1}$ . The maximum preform length supported is  $\approx 1$  m. On the furnace exit, there is an additional meter of clearance before the drawn fiber contacts the pulling system, with draw speeds ranging from 5 mm/min to 5000 mm/min with a speed resolution of 0.4 mm/min.

As discussed, the preform consisted of stacked concentric tubes. As such, ensuring that the tube walls collapse to form a dense fiber during the draw necessitates the ability to controllably evacuate the preform interior. The design of the vacuum fitting incorporates high-temperature silicone gaskets with square cross-section into a two-piece brass housing. A tapered conical face on the bottom piece applied compression to one of the gaskets on the preform exterior to ensure a tight seal

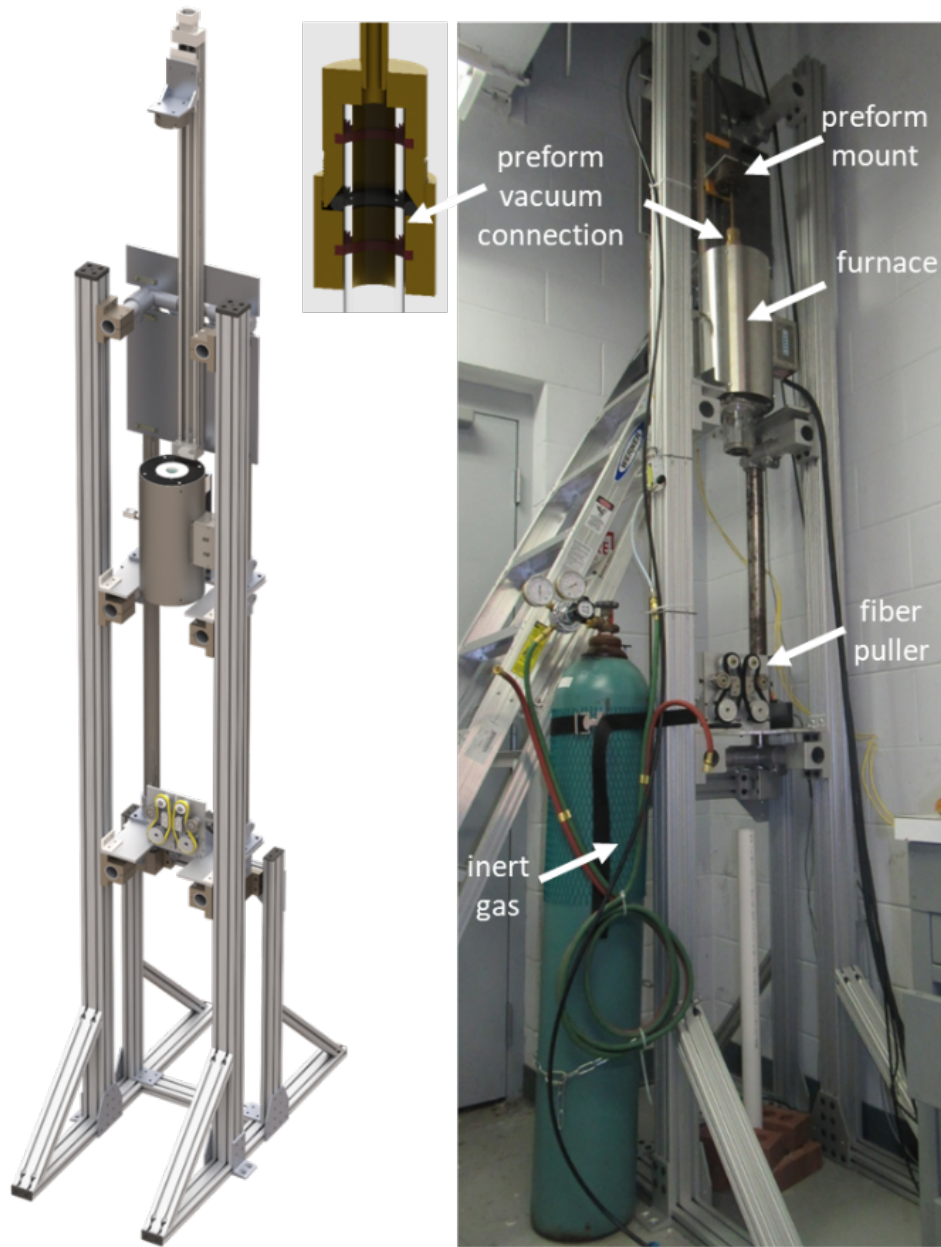


Figure 4.4: (Left) Schematic depicting the custom-built intermediate- $T_g$  fiber draw tower. (Right) Photograph of the system with the primary components referenced. The inset shows a cross-section schematic of the preform vacuum connection through which the interior of the glass preform is degassed to promote collapse of the preform into a densified solid fiber.



while simultaneously securing the preform end to the vacuum fitting. The top piece had a stepped-diameter center-bore to accommodate the top end of the preform while providing a path for the evacuated gas up through a pipe nipple. The pipe passes through the center of the lathe chuck that secures the preform and vacuum fitting assembly the linear positioning carriage, thereby preserving the alignment of the preform with the furnace axis and fiber puller below. A tee-junction connected in-line with the vacuum permitted monitoring of the absolute pressure of the preform interior. Additionally, the pressure could be dynamically controlled as needed with an installed precision regulator valve.

### **4.3 Fiber Fabrication and Structural Characterization**

Fiber drawing proceeded following the preparation of the electrically conductive composite glass and manufacture of the new draw tower. Initial fiber drawing trials consisted of a single core with varying composite properties to characterize the behavior during and after the draw in comparison to the preform (Figure 4.5). The resulting fibers exhibited varying behavior in a similar manner as that observed during the development of the conductive composite. Changing the initial of the morphology of the composite would result in different core morphologies following the draw. Namely, it was observed that, for certain compositions, loading the composite as a powder without first sintering and hot-pressing into a densified bulk would produce favorable core continuity and conductivity related to the porosity. Likewise, changing the composition but fixing the initial morphology resulted in an optimum loading fraction that both exhibited uniform viscous flow with smaller diameter variation while maintaining useful electrical conductivity through the fiber.

The next step involved incorporating a crystalline phase into the preform structure in addition to the composite. A thermally compatible metal alloy was selected with melting temperature below that of the draw temperature, but not too low so that the wire liquefied during the preform heating

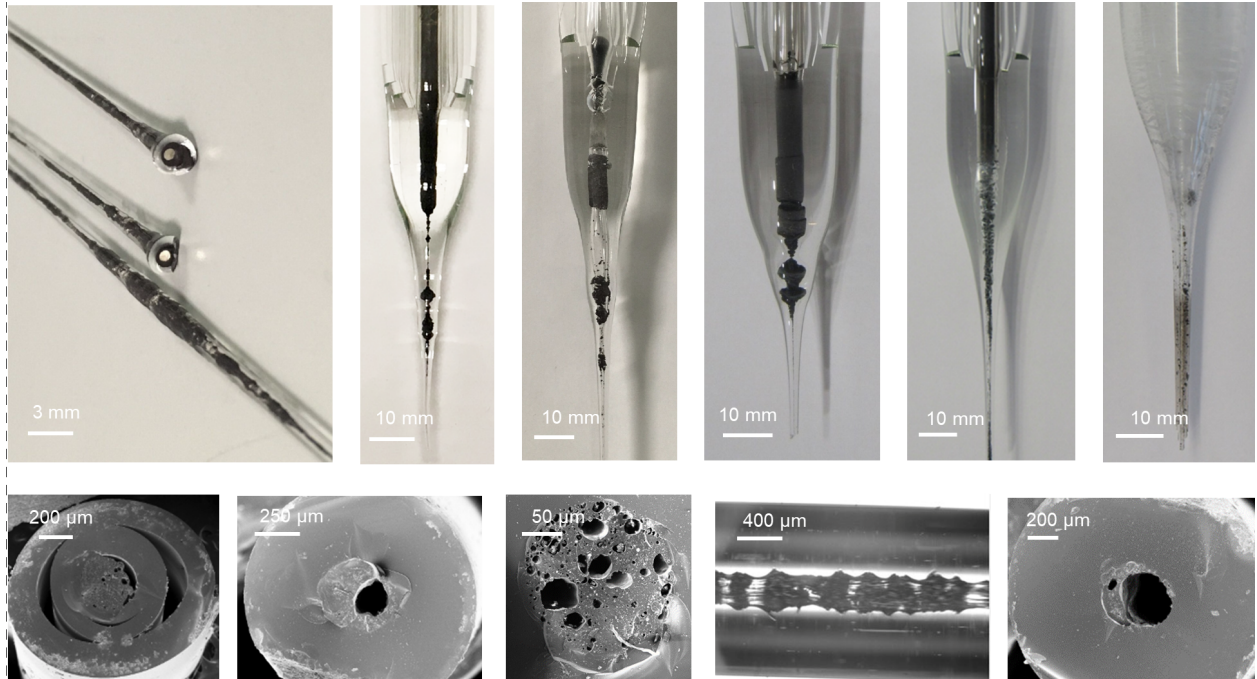


Figure 4.5: (Top) Photographs depict the drawn fiber neck-down regions from early trials with a single conductive composite glass core. Variations to the loading fraction, glass matrix, and preform construction all impacted the resultant fiber core continuity. SEM micrographs depict various failure mechanisms ranging from incomplete preform collapse to more typical porosity in the core due to volatilized products and phase separation of the CNFs.

stage at the draw outset. Typically a difference of 80 °C to 120 °C below the draw temperature would result in favorable fiber. It was determined additionally that the quality and composition of the metallic alloy could affect the draw significantly if de-alloying and phase separation occurs in the neck-down region. Best results were achieved with a bronze allow.

With the draw dynamics for the composite and metal conductors understood, the next step was to incorporate a crystalline semiconductor. Based on availability and melting point, GaSb was initially tested as a single-core, as a core embedded in a composite sheath, and finally as a three-layer composite/GaSb/composite structure with parallel interfaces in the preform. The drawn fiber provided useful insight into the relative ratios of semiconductor to composite to glass cladding needed for the given draw parameters. Upon inspection of the cross-section with EDXS and SEM,

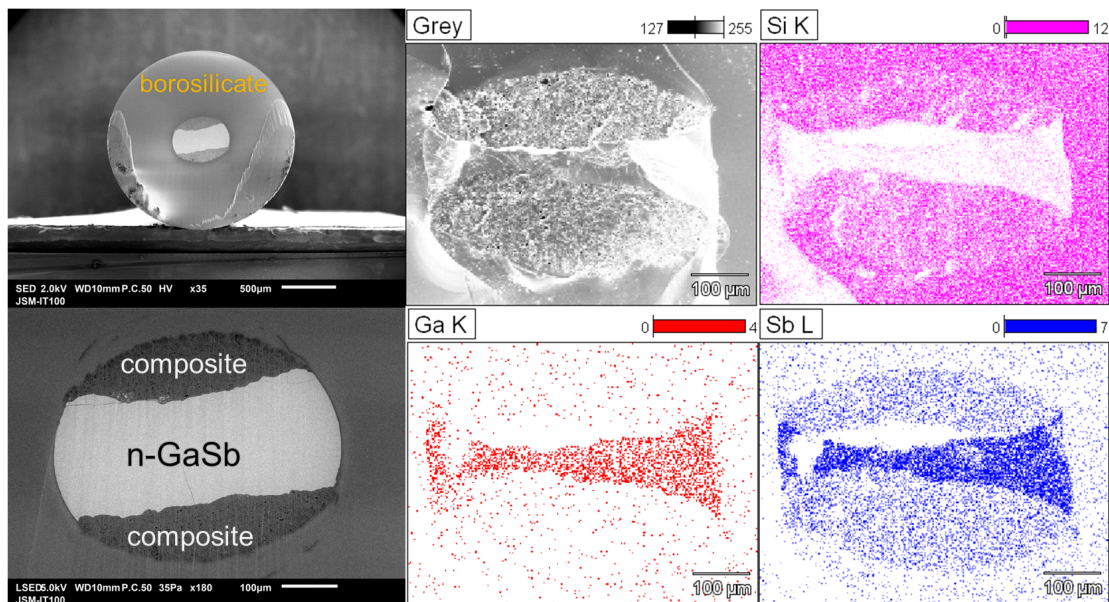


Figure 4.6: SEM micrographs in the left column depict the polished cross-section and zoomed-in core of the 3-layer device fiber. SEM and EDXS in middle and right columns characterize the integrity of the structure. The higher relative vapor pressure of the Sb caused clear diffusion out of the core and into the surrounding composite and glass during the draw.

it was evident that the higher relative vapor pressure of the Sb in the compound semiconductor led to partial disassociation and diffusion from the core (Figure 4.6). The behavior both reduced the electronic properties of the semiconductor region and contributed to diameter and continuity variations exhibited during the draw.

The results from the 3-layer device informed the next step in the fabrication. It is clear that for the prototype effort, it would eliminate a process unknown if an elemental semiconductor were used in place of the compound GaSb to avoid adverse effects related to diffusion and disassociation. From prior work, the melting and draw dynamics of Ge cores were well-described. A new alloy was selected to better match with the increased draw temperature required (from 900 °C to 1030 °C) along with appropriate adjustments to the composite composition. After initial trials with single-core and 3-layer structures, a complete 5-layer preform was constructed with two metal conductors along either side of the Ge core. The metal and Ge were separated by a region of composite glass

to prevent mixing of the two phases during the draw. Preform construction for the more complex structure required careful machining and shaping of the glass tubes to compact the geometry as best possible. The resultant drawn fiber is the first of its kind, consisting of an axially continuous architecture with a traditional semiconductor and two metallic conductors electrically connected at two junctions that span the length of the fiber (Figure 4.7).

#### **4.4 Characterization of Optoelectronic Properties**

Upon exiting the furnace, the fiber quenches relatively quickly down below the melting and softening temperatures of the Ge core and glass sheath, respectively. The metallic conductors are expected to solidify first due to closer proximity to the fiber exterior and to their smaller diameter than the core. Rapidly quenching molten states produced from originally crystalline solids typically results in polycrystalline solids as the randomly oriented atoms characteristic of liquids are essentially locked into their energetically favorable disordered lattice. Unlike the core, the crystallinity of the metal does not significantly alter their electronic properties with respect to their in-fiber function as electrodes. The semiconductive properties of the Ge core are, however, altered between single-crystal and polycrystal lattice structures as is generally typical of traditional semiconductors. Validation of this behavior was quickly performed by comparison of the fiber electronic properties before and after undergoing an annealing cycle.

With the drawn fiber annealed, the optoelectronic behavior of the 5-layer device was probed in a series of three measurements (Figure 4.8). In all three cases, the fiber was irradiated from the side (along the radial direction) with a 1.55  $\mu\text{m}$  laser focused to a 5 mm spot size targeted at an exposed area of the Ge core (avoiding the metallic and composite conductors). The electrodes were then connected to the poles of a sensitive source meter. The photocurrent, responsivity, and I-V behavior were measured in response to changing laser power. Additionally, the dark current behavior was

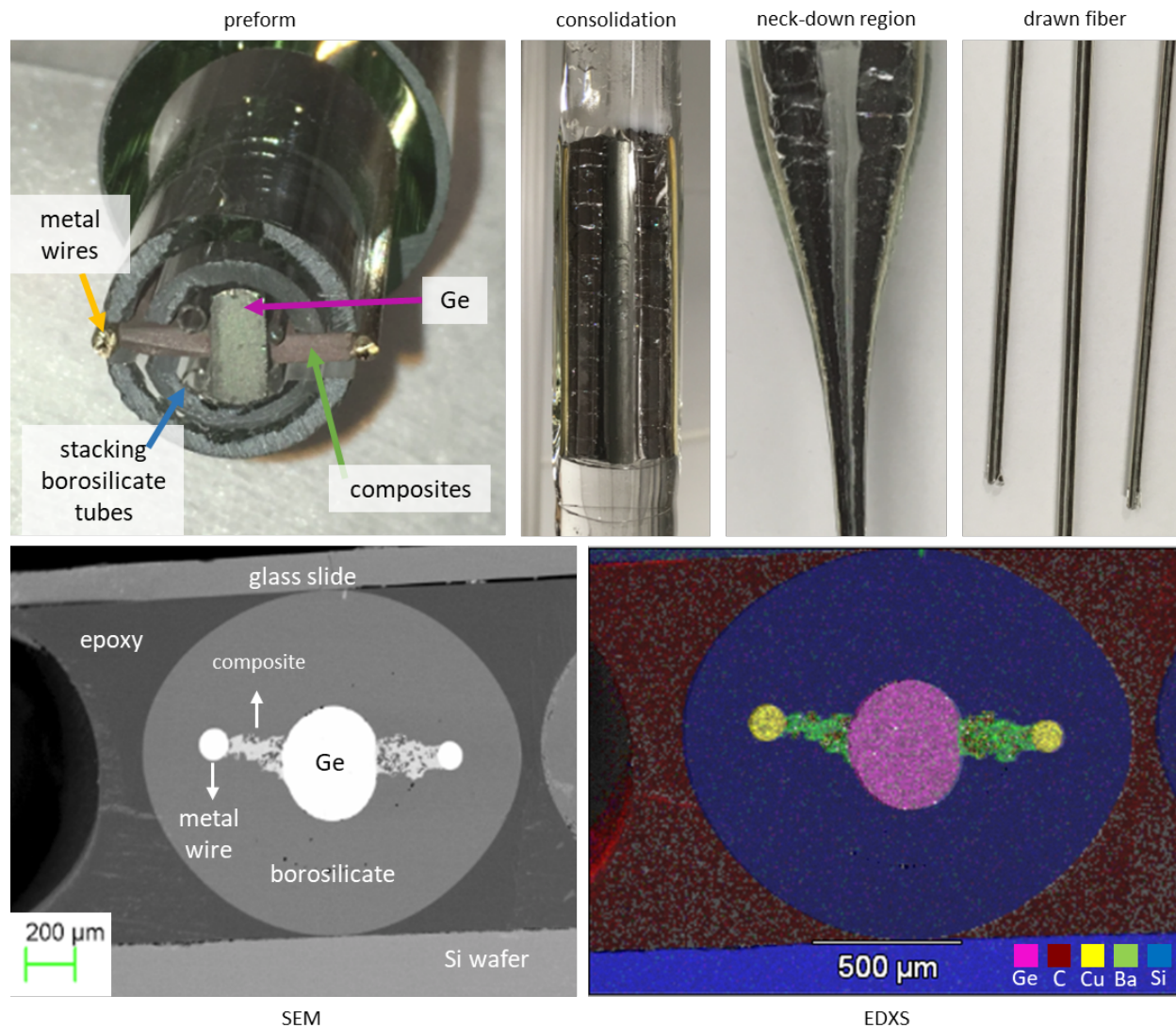


Figure 4.7: Top row photographs depict the electronic fiber device at successive stages in the fabrication process, from preform to fiber. The composite acts as a viscous barrier during the draw that prevents the crystalline wires and semiconductor from mixing while maintaining a conductive path in the fiber following re-solidification. The bottom row depicts the fiber cross-section, polished using a focused ion beam (FIB). On the left, the cross-section is shown in SEM. The colored micrograph to the right was produced on the same cross-section using energy dispersive x-ray spectroscopy (EDXS) and verifies that the various material phases did not mix during the fiber fabrication.



probed by applying a square wave duty cycle to the laser, switching the power between On/Off states. In all cases, meaningful photoresponsivity was observed in a manner consistent with typical semiconductors. Interesting behavior of the sensitivity with low bias voltage was observed that is somewhat akin to the behavior exhibited by irradiated thermoelectric materials, although further investigation is warranted prior to drawing conclusions. Additionally, the non-unity power-law fit of the photocurrent to the applied laser power suggests some complex dynamics involving electron-hole generation, recombination, and trapping occurring throughout the semiconductor.

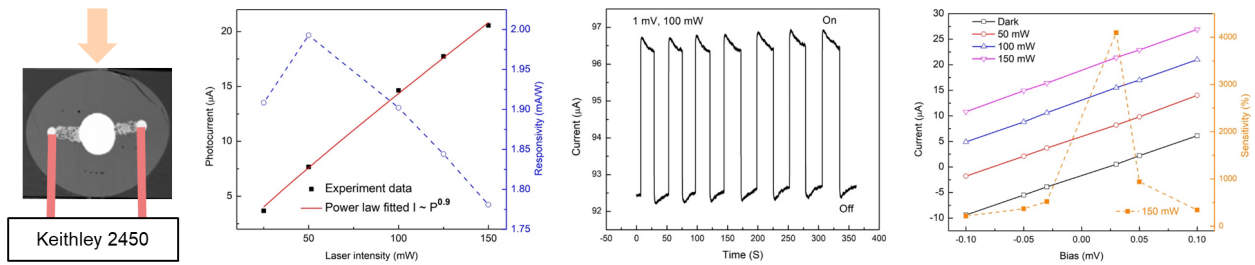


Figure 4.8: Fiber cross-section at left depicts the measurement scheme with connected source meter and incident laser direction. The plots depict behavior consistent with photo-induced responses characteristic of traditional semiconductors.

## CHAPTER 5: DESIGNER COMPOSITE MICROSPHERES FOR TUNABLE OPTICAL SCATTERING

Thus far, the fiber devices discussed possess functionalities that are facilitated by or based on the preservation of the cross-sectional architecture over an extended length. In this section, the fiber will instead act as intermediate device through which multimaterial, structured, functional, and uniformly sized micro- and nano-scale spheres are produced. The process by which such spheres are generated from fiber is described in Kaufman et al, developed in the MOFD Group at CREOL, and harnesses the fluid instabilities occurring at the interfaces throughout multimaterial fibers [52]. These instabilities manifest as a “push-pull” between surface tension and viscosity, realized as a superposition of waves oscillating along the interface, with tension acting to change the geometry so as to minimize surface area (energy) while viscosity resists against the changing morphology.

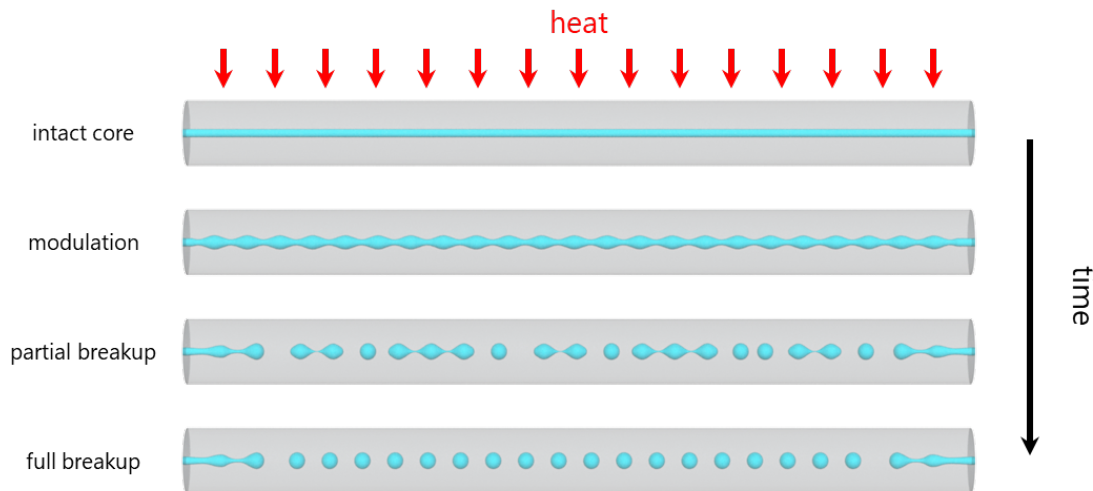


Figure 5.1: Schematic of in-fiber sphere formation via PRI. A fiber section with intact core is heated until both the sheath and core polymers are softened to lower viscosity state than that during the draw. After some time, typically a few minutes, the softened core begins to modulate at a spatial frequency related to the core dimension. Eventually, surface tension minimizes the surface energy between the core and the sheath fluids, driving the modulated core to “pinch-off” and form spheres. The result is a necklace of spheres with smaller “satellite” spheres in between the primary spheres.

A special case of these generalized instabilities is the Plateau-Rayleigh Instability (PRI) whereby a fluid capillary jet immersed in a second fluid breaks up into a necklace of uniformly sized and evenly spaced spheres (Figure 5.1). The process requires two immiscible fluids and is functionally described in Tomotika's work [98]. Given that the geometry of a simple sheath/core multimaterial fiber mimics that of a solidified fluid capillary (core) immersed in a sufficiently extended, solidified fluid matrix (sheath), one would expect PRI to arise at the interfaces during fiber fabrication while the materials are in a melt state, as is the case during thermal drawing. However, due to the low residency time in the furnace, the instabilities are not able to resonate and grow to the point of driving the core discontinuous – the instabilities are in effect “frozen” in place. Kaufman showed that these locked-in instabilities could be “reanimated” by thermally transitioning the fiber to a lower viscosity state compared to that during the draw, causing the viscous core to modulate at the resonant spatial wavelength along the fiber axis and eventually pinch-off into spheres. It was further shown that radial and azimuthal structures at the preform would be inherited by and preserved in the spheres generated through this process (Figure 2.11). This ability to produce complex structures provides a pathway for introducing a range of compartmentalized functionalities into the spheres by selectively doping the core at the preform level [37, 57, 92, 93, 99].

The framework for producing structured and functional spheres from multimaterial was established using thermal fiber drawing as a fabrication platform. Although an effective method for maintaining tight dimensional tolerances across a range of materials and structures, the process suffers from its inherent batch-scale nature and is thus limited when considering scaling to commercial volumes. Many, if not most end-use applications involving micro- and nano-spheres communicate demand in terms of metric tons, and so a new approach whereby kilogram-scale preforms are converted to spheres would not represent a viable or cost-effective fabrication route despite the attractive and often irreplicable features and functionalities of such spheres when compared to traditional fabrication methods.



It follows logically that if the same methodology of PRI-induced sphere fabrication could be translated to a more conventional, continuous-style manufacturing process, then the potential to meet commercial demand would be viable. By volume, fiber extrusion spinning unequivocally produces the vast majority of the global synthetic fiber demand. As described in Chapter 6, incorporating proprietary melt distribution technology with multicomponent screw extrusion enables the direct fabrication from raw material of fiber, multifilament threads, and non-woven fabrics with complex and axially continuous internal architectures. This methodology is easily scalable to production levels on the order of one metric ton per hour, more than sufficient to meet commercial demand.

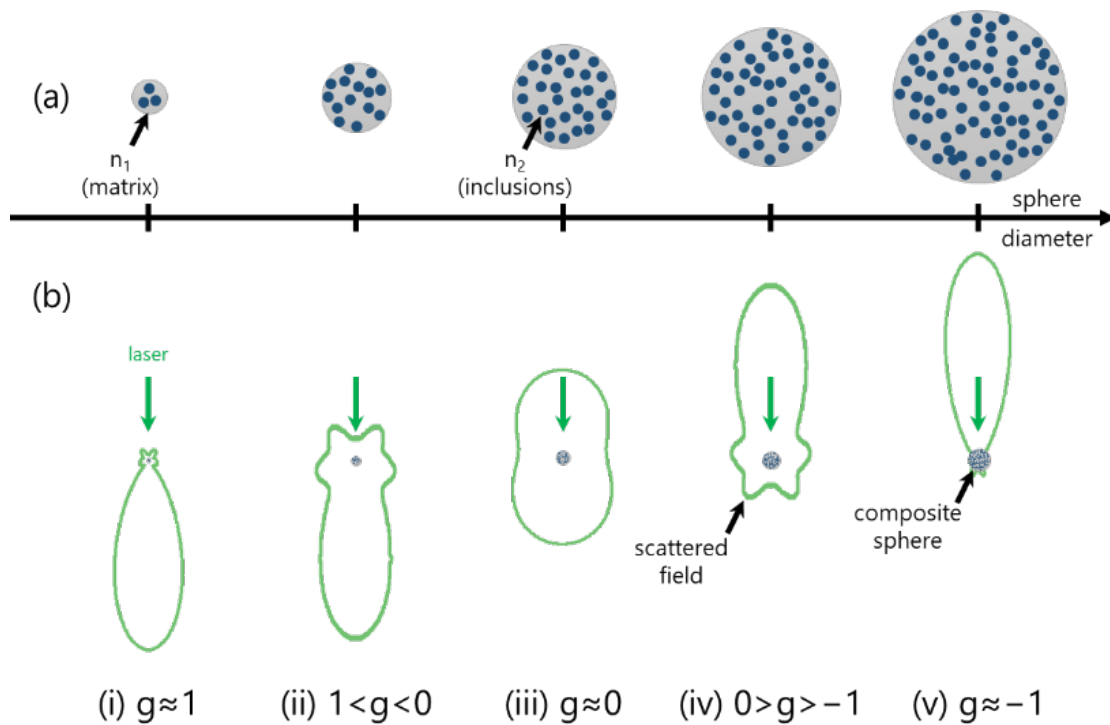


Figure 5.2: (a) Using the fabrication approached described, spheres of arbitrary size can be fabricated with fixed concentration of high-refractive-index ( $n_2$ ) nano-scale inclusions embedded in a low-refractive-index ( $n_1$ ) polymer matrix. (b) The direction of the scattered field from the sphere when irradiated by a plane wave is quantified by the asymmetry factor  $g$ . (i) For small sphere diameters, Mie scattering results in dominantly forward scattering ( $g \approx 1$ ). Increasing the diameter from (ii) to (v) results in a shift to backward scattering ( $g \approx -1$ ) transitioning through a configuration with uniform ( $g \approx 0$ ) "dipole-like" scattering. [100]

## 5.1 Motivation: "Macroscopic Dipole" Scattering

With the PRI process described, and a method for scaling to commercial volumes established, a research effort was undertaken to address specific need from an industry sponsor. White paint is a ubiquitous commercial product manufactured and delivered globally on a massive scale. The primary pigment that provides the characteristic white color are high-index, inorganic, and transparent nanoparticles uniformly dispersed throughout the paint. In most cases, titanium dioxide is selected as the pigment due to its relatively advantageous properties when compared to similar inorganic materials in the same family. However, although readily available in sufficient quantities to meet demand,  $\text{TiO}_2$  nanoparticles are, by mass, the most expensive component in these paints. As such, it is of commercial interest to paint manufacturers to minimize the amount of  $\text{TiO}_2$  used without sacrificing the high-quality standard, performance, and appearance of the finished paint.

The principle governing the white appearance of  $\text{TiO}_2$  is optical scattering from small particulars. When dispersed in a polymer coating, the index contrast of the  $\text{TiO}_2$  with respect to the surrounding matrix is fairly large ( $\Delta n \approx 1$ ). Along with the small average diameter of the  $\text{TiO}_2$  nanoparticles ( $\approx 300$  nm), scattering theory predicts fairly uniform scattered redistribution of incident visible light. An additional feature of  $\text{TiO}_2$  is the negligible absorption through the visible spectrum, so that all colors scatter elastically. Combining these features, the effect is strong, omnidirectional scattering throughout the visible spectrum, and hence the white appearance.

Mie theory instead describes the scattering of light from similarly homogeneous dielectric spheres but with dimensions much greater than the wavelength of the incident radiation. For typical microspheres, visible light will scatter strongly in the forward direction as might be expected using geometric ray tracing technique. However, as the sphere reduces in size, the scattered field begins to redistribute more and more into the side and backward directions. Now, although the omnidirectional scattering from  $\text{TiO}_2$  nanoparticles is effective for the purpose of applying a white ap-

pearance to coatings, the system is disadvantaged by the small physical extent of the nanoparticles. That is, at low concentrations, ballistic light readily passes through the coating without interacting with spheres, so that the amount of back scattered white light is significantly diminished with decreasing concentration. This effect is counteracted by increasing the concentration to a level that requires treatment of the coating as an inhomogeneous random media (a granular material).

The interaction of coherent light with such granular systems, due to the large index contrast between the constituent materials, can be characterized as a series of multiple scattering events. In contrast to a single scattering event, speckle patterns resulting from such multiply scattering media exhibit spatially varying polarization states with little resemblance to that of the incident field. In the context of granular coatings, this would imply that the relationship between the degree of scattering and the polarization properties of the scattered field can provide useful insight.

Now, an advantageous feature of the aforementioned methodology for generating spheres from multimaterial fibers is the ability to disperse additives throughout the sphere volume by first com-

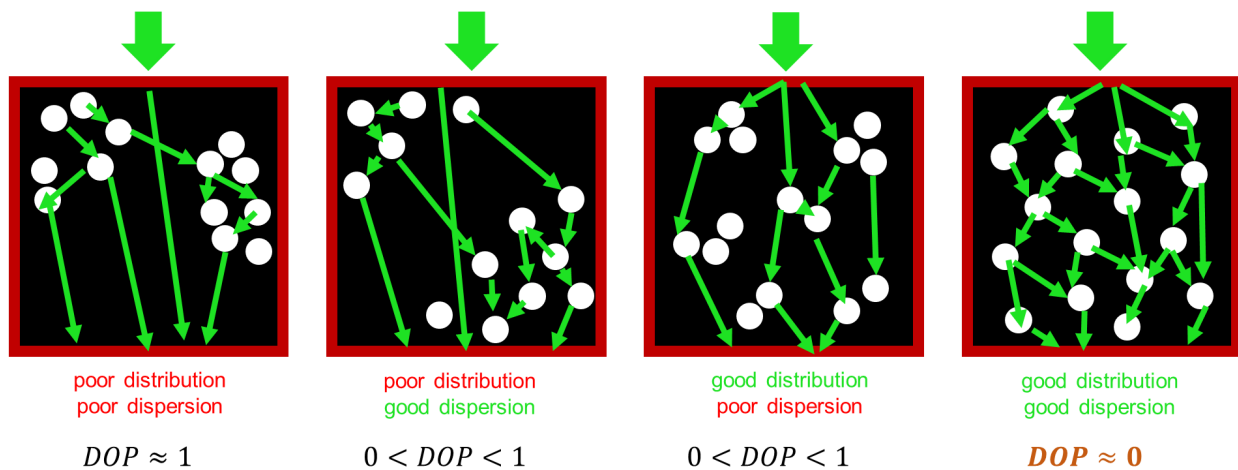


Figure 5.3: Schematic comparison between distribution and dispersion of additives in a compound or granular material. High degrees of both minimize the ballistic light that propagates through the material thereby enhancing diffusive scattering. Each scattering event scrambles the incident polarization so that the Degree of Polarization (DOP) can be used a metric to characterize the randomness, uniformity, and separation of nanoparticle additives.

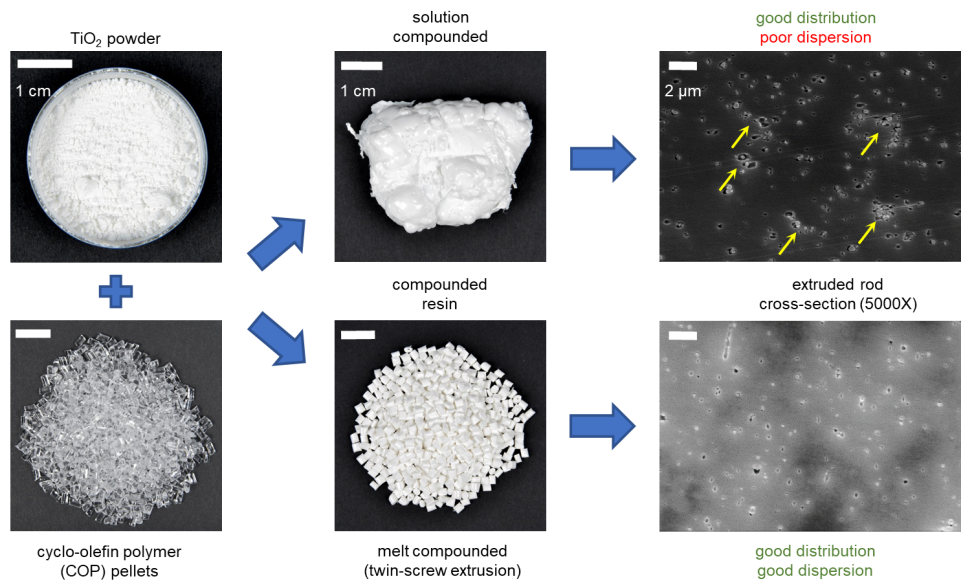


Figure 5.4: Photographs and SEM micrographs of the compounding process proceeding by either solution (top) or twin-screw (bottom) method. The arrows highlight clustering characteristic of solution method.

pounding the core at the preform level. With careful selection over material properties, granular microspheres are readily produced that marry the omnidirectional scattering behavior of individual  $\text{TiO}_2$  nanoparticles with the diffusive scattering characteristic of random inhomogeneous media. Moreover, these composite microspheres consequently no longer scatter in a manner consistent with Mie theory.

So, it has been established that varying the size of homogeneous spheres consequently varies the spatial distribution of scattered light. It has likewise been established that varying the concentration of small scattering particles will transition the system from mostly ballistic with single scattering events to diffusive scattering with enhanced back scattering due to multiple scattering events. Combining these two behaviors, it is reasonable that the varying either the size of the composite (granular) microspheres or varying the concentration of granular inclusions throughout the volume will likewise vary the properties of the resulting scattered field. It is also reasonable that there exists, for a given microsphere diameter, inclusion diameter, and index contrast, an inclusion

concentration that maximizes diffusive scattering and therefore enhances the scattered field in the side and back directions (Figure 5.2). The amount of diffusive scattering is related to the number of multiple scattering events occurring throughout the volume, and since multiple scattering increasingly severs the polarization states of the scattered field from the incident, it follows that the degree of polarization can be used as a figure of merit to interrogate the diffusive field and therefore provide a measure of the degree to which the inclusions are randomly and uniformly dispersed throughout the microsphere volume.

## 5.2 Thermal Fiber Drawing Approach

Thermally drawn fibers with composite cores follows the procedures outlined in Chapter 2 apart from one crucial difference. In the previously discussed work, additives were compounded into polymer hosts by mixing into solutions and volatilizing away the solvent. Although sufficient for most practical prototyping purposes, this method does not properly *disperse* the additive to the same degree to which the additives *distribute* throughout the volume of the compound. The difference is subtle but underlies the scattering mechanism in question (Figure 5.3). Specifically, agglomeration (or "clumps") of nanoparticles do not scatter in the same manner as individual nanoparticles since multiple scattering, in a rigorous sense, describes observations made from groups of scatterers sufficiently separated such that each is located in the far-field with respect to each other. That is, tight clustering of nanoparticles would behave in a manner somewhere in between a group of individual nanoparticles and a single larger particle from which scattered fields preserve polarization of the incident field. To overcome this tendency to agglomerate, an industry-proven method for compounding nanoparticles into thermoplastic polymers was used to great effect (Figure 5.4).

Extrusion of the compounded resin proceeds as previously described in Chapter 2.5 except that the

die dimensions for the COP and PS are reversed. The PS sheath is selectively soluble in several solvents, with dimethylacetamide (DMAC) typically used. As discussed, tuning the optical scattering from the resultant composite microspheres can be done by either varying the concentration of the inclusions and fixing the sphere diameter, or by fixing the concentration and varying the sphere diameter (as in Figure 5.2). The latter is presented here as multiple diameters are readily produced by varying the draw parameters dynamically throughout each fiber reduction. In this way, a range of core sizes are produced that subsequently break-up into a range of sphere diameters to pro-

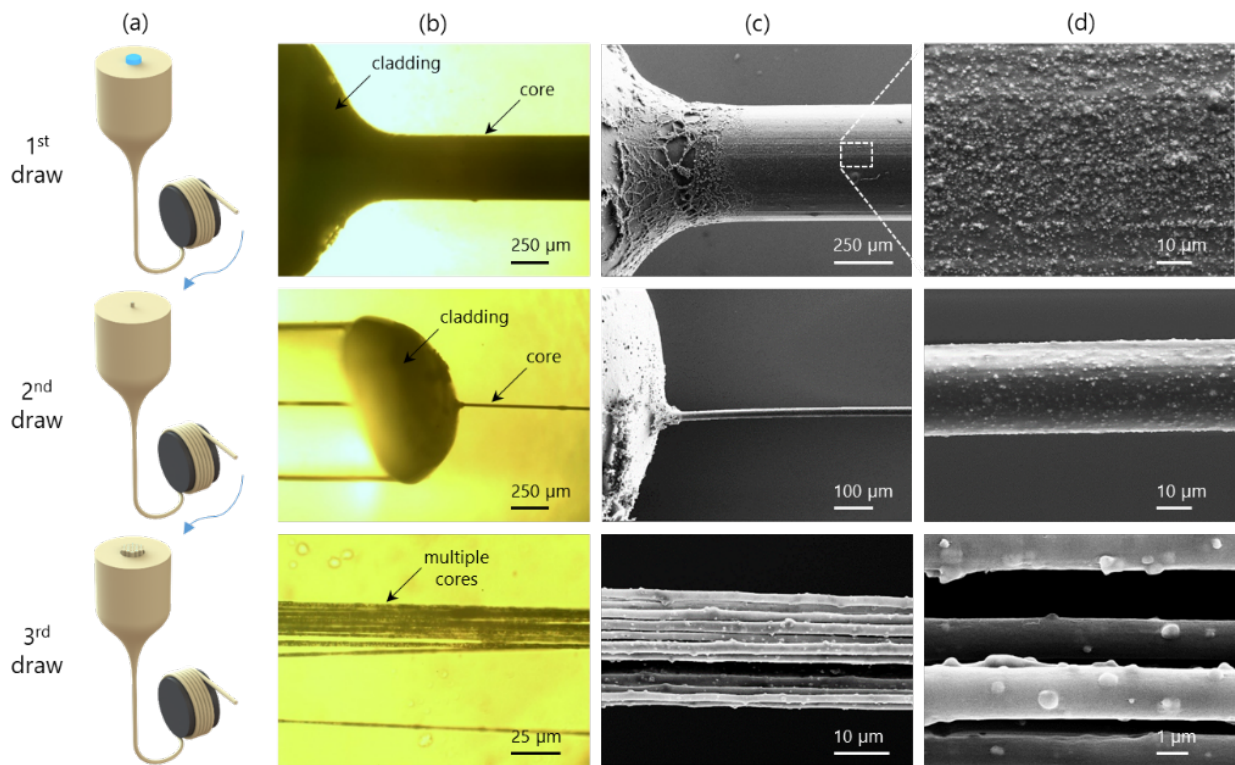


Figure 5.5: Fabricated composite fibers from the millimeter scale to micron scale at fixed concentration of  $\text{TiO}_2$  nanoparticles through stack-and-draw. First row depicts the fiber resulting from the initial preform drawing. Second row results from drawing a preform in which the previous fiber is included as the core. Third row depicts a multi-core fiber resulting from stacking the previous (second draw) fibers into the core of a new preform. (a) Schematic of preform to fiber drawing. (b) Side-view transmission optical micrograph of the exposed core at the fiber tip after dissolving the cladding. (c) SEM of the exposed fiber core in (b). (d) Higher magnification SEM of the fiber core surface highlighting the  $\text{TiO}_2$  additives protruding from the surface.

vide more data during optical experiments. Figure 5.5 depicts characterization of a select number fibers from each draw step. The high surface energy and poor miscibility between the COP and PS core(s) and sheath prevents diffusion of the TiO<sub>2</sub> inclusions. The composite spheres were first fabricated using single-core (and then multi-core for smaller diameters) fiber comprising a COP core compounded with TiO<sub>2</sub> nanoparticles and a sacrificial polymer sheath. This fabrication method allowed for rapid turnaround for varying concentrations, although suffered from poor overall yield per unit length of fiber.

Sections from the drawn fibers are then heated on glass microscope slides at a slight higher temperature than the draw. The time required for capillary break-up scales with the viscosity and diameter of the core. For spheres depicted in Figure 5.6, break-up typically occurs in 8 min to 10 min with the oven set to 280 °C. Following break-up, the suspended spheres are released from the PS sheath by dissolution in DMAC. The solution is then centrifuged with the spheres pelleted at the bottom of the tube. Excess solvent is removed and replaced with clean DMAC. The spheres are then re-suspended in the solvent, agitated, and then centrifuged again. The process is repeated 3 to 4 additional cycles to ensure residual PS is sufficiently diluted so as to not adversely affect optical experiments.

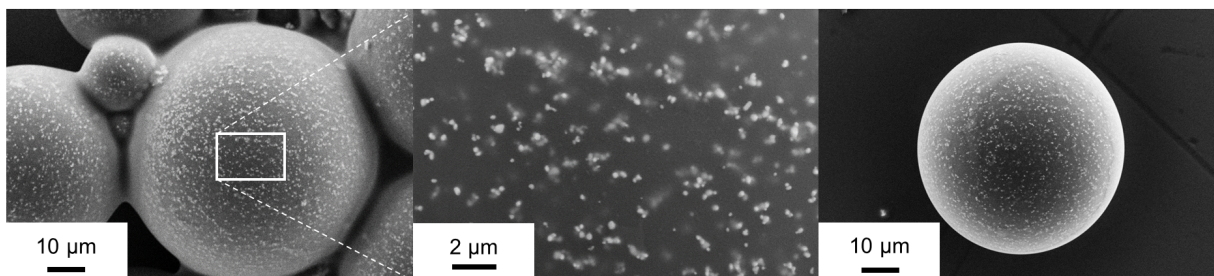


Figure 5.6: SEM micrographs depict extracted composite microspheres following dissolution of the PS sheath. The primary sphere diameters average 60 μm. Smaller satellite spheres are visible. Optical experiments were performed on individual spheres.



### 5.3 Characterization of the Optical Scattering Properties

Optical experiments were carried out on a single composite sphere. A 532 nm laser (Lightwave electronics, 142II-532-200) was focused down to the mid-plane of the sphere and the scattered field imaged in the forward, backward, and dark-field directions. A half-wave plate at the laser output tuned the polarization. The beam then splits into two channels with the transmission (forward) in one leg. The reflection (back) and dark-field excitation beams share a leg. Mirrors guide the transmission excitation to a long working distance objective lens (Nikon CF Plan 50X/0.45 EPI SLWD). In the reflection/dark-field leg, the beam is first expanded and spatially filtered then directed to a second objective lens (Zeiss - LD EC Epiplan-Neofluar, 20X or 100X). The magnification was changed depending on the size of the particle. In lieu of a dark-field objective lens, a mask was inserted into the beam path to produce an annular profile prior to focusing onto the sphere. In all configurations, the scattered fields were imaged and recorded using another objective lens and a CMOS camera (Jenoptik ProgRes CT5, color-version). For measurements of the DOP, an analyzer was placed before the camera. The complete setup and selected captured micrographs are shown in Figure 5.7.

The captured micrographs of the scattered field imaged at each sphere mid-plane were used to calculate the power by integrating inside a fixed area box for a set measurements. In one study, the scattering from a 70  $\mu\text{m}$  composite sphere is compared to a 10  $\mu\text{m}$  homogeneous sphere. The DOP was calculated from polarization measurements for each sphere in the transmission, reflection, and dark-field directions. Polarization was measured by rotating the analyzer in  $5^\circ$  increments and recording the imaged scattered field. As expected, single-scattering from the homogeneous sphere preserves the polarization state of the incident field, resulting in near unity DOP in the forward and backward direction (Figure 5.8). The DOP for the dark-field configuration indicates that the measured field is still slightly polarized for the homogeneous sphere. This is due to the use of



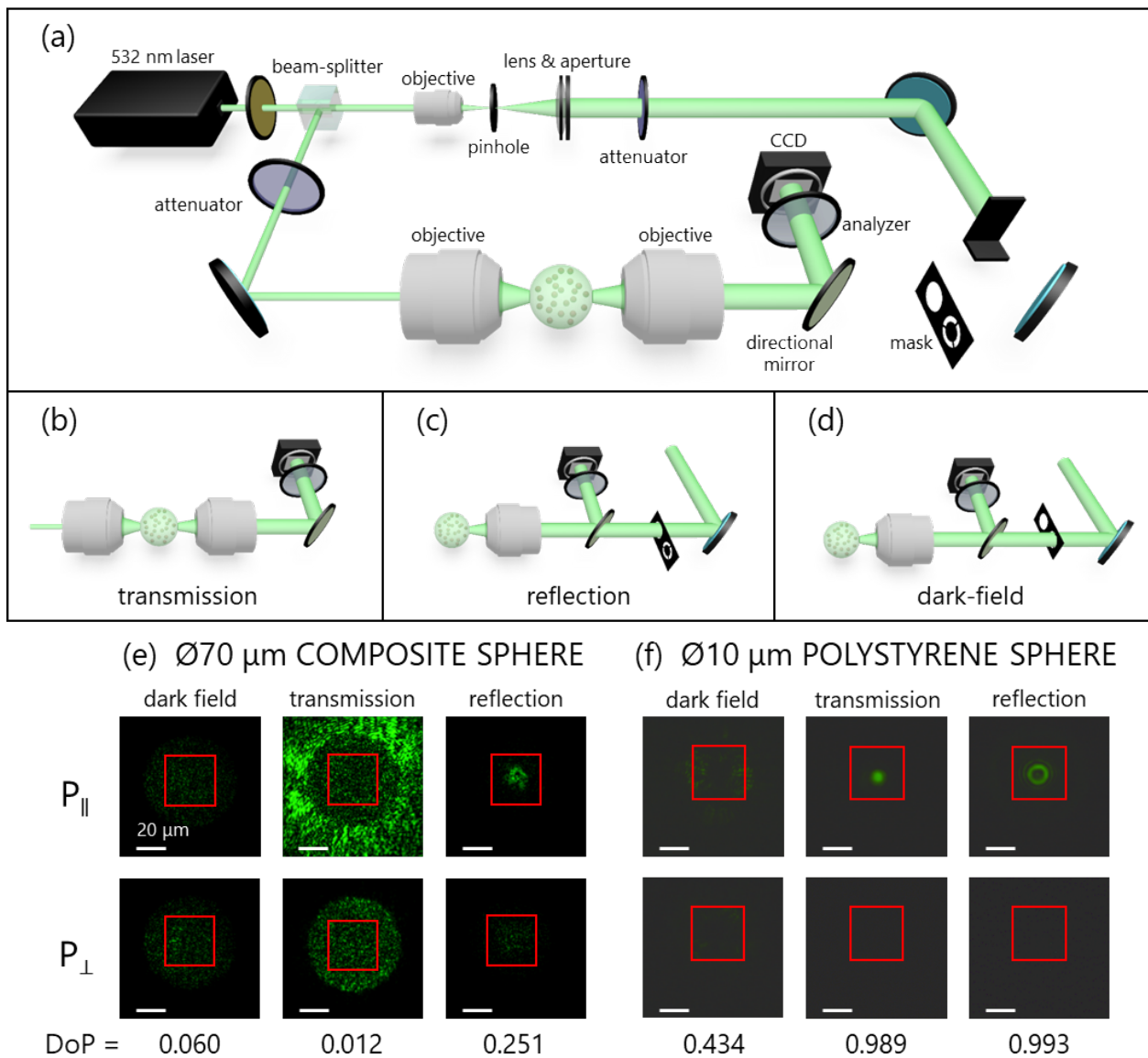


Figure 5.7: a) Schematic depiction of the overall optical configuration. A single sphere is positioned between two objective lenses. The laser and components can be adjusted for: b) transmission, c) reflection, d) or dark-field (DF) configurations, the latter using a mask in lieu of a DF objective lens. e) Optical measurements carried out in all three configurations on a 70  $\mu\text{m}$  diameter composite sphere. The degree of polarization (DoP) is near zero in all configurations. f) Similar to e) but for a 10  $\mu\text{m}$  diameter polystyrene sphere (no inclusions). The DoP instead approaches unity in reflection and transmission. The use of a mask for the DF leads to elliptical polarization and hence a non-zero DOP. In both e) and f), the red box corresponds to the integration area for the purpose of calculating the scattered intensity. [100]

a mask to produce the annular beam profile. The angle of the impinging beam generates finite elliptical polarization which is preserved through the linear analyzer at the CMOS input. The composite sphere shows similarly expected behavior as well. In the forward direction, the DOP is near zero, indicating highly diffusive scattering characteristic of granular inhomogeneous media. Likewise, in the dark-field configuration, the DOP is again small despite the elliptical polarization incident on the composite sphere. This is again indicative of diffusive multiple scattering. The reflection case, however, retains meaningful DOP compared to the other two cases. This again is expected as primary (single-scattering) reflections from the granular surface retain polarization state with respect to the incident beam.

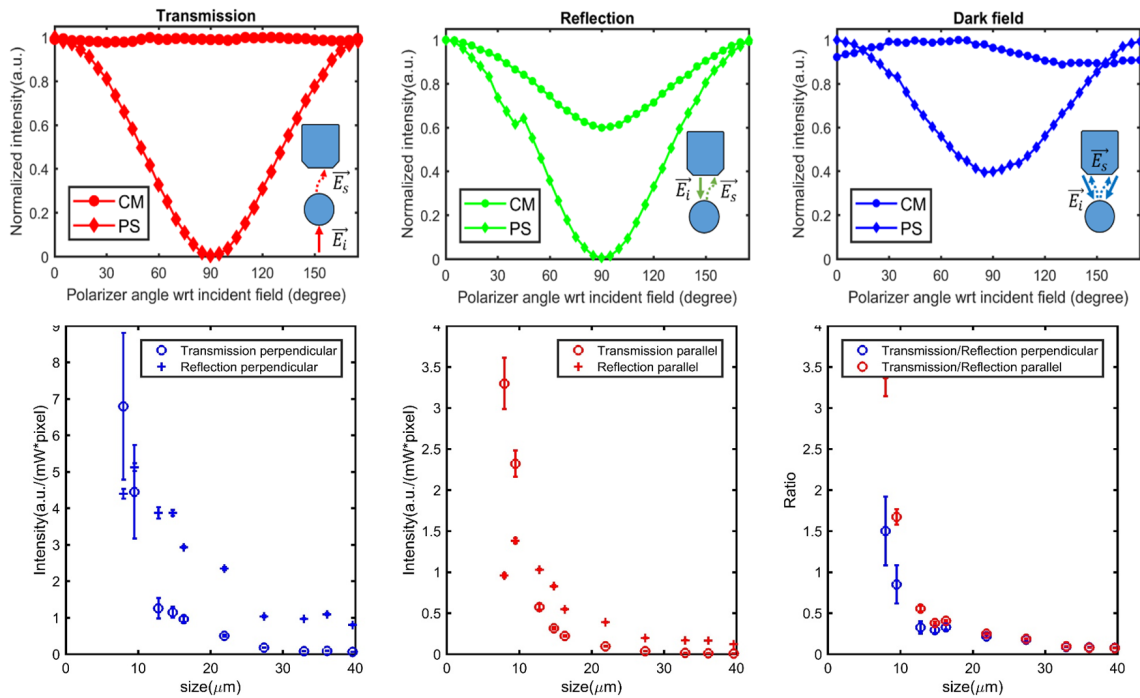


Figure 5.8: (Top) Data plots depict polarization measurements for a 70 μm composite microsphere and a 10 μm homogeneous PS sphere in the three scattering directions. (Bottom) Data plots depicting the orthogonal and parallel polarization measurements from composite spheres with fixed TiO<sub>2</sub> inclusion concentration and varying sphere diameter. Each sphere was measured in the forward and backward direction for each polarization. The ratio of transmitted to reflected scattered power depicts uniform distribution for sphere diameter of ≈10 μm.

Finally, the tunability of the scattering direction is probed by recording the scattered field in the parallel and orthogonal polarization states for the forward and backward direction. Several spheres with fixed inclusion concentration and varying diameter were probed to determine the relative distribution of scattered power. It is clear that, for the case here of 10% mass fraction of  $\text{TiO}_2$  inclusions in a COP matrix, the scattered power is evenly distributed in the both forward and backward directions for  $\approx 10 \mu\text{m}$  diameter spheres. Increasing the sphere diameter at this concentration enhances the back scattering and diffusive scattering, while decreasing diameter enhances forward direction and polarized ballistic light.

## CHAPTER 6: MULTICOMPONENT EXTRUSION OF NOVEL FUNCTIONAL FIBERS

In the preceding chapters, thermal drawing from a preform was the mechanism selected for fabrication of the multimaterial fiber devices presented. Benchtop production of fiber prototypes progressed into two fiber devices, namely a mid-IR optical fiber and an optoelectronic fiber, that exhibited sophisticated functionality and incorporated both novel and proven fabrication techniques. A third fiber system served as a precursor for producing uniformly sized composite spheres using a fabrication methodology that enabled tunable control of the optical scattering properties. In all cases, scaling fabrication to commercial levels readily ensues by adopting the proven strategies employed by the telecommunications industry for the manufacture of silica optical fibers. These strategies are optimized to produce long continuous lengths of fiber with extremely precise dimensional tolerances from a single draw tower as rapidly as possible—typical production rates are on the order of 2 km/min for standard step-index single-mode fibers. However, due to the finite preform size and weight, and to limitations on the feed rate set by heat transfer and preform thermal conductivity, typical production volumes *in terms of mass* are only on the order of a few kilograms per

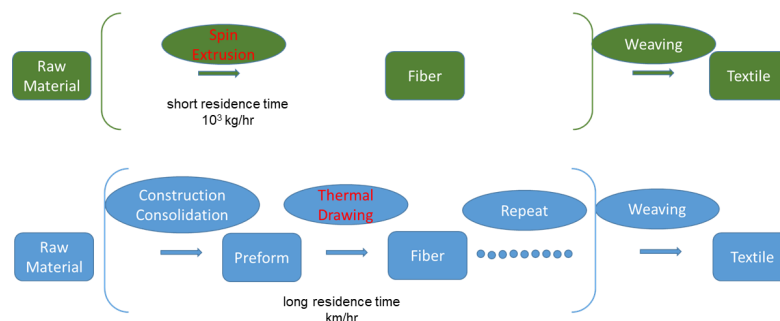


Figure 6.1: Example process flow chart for textile prototype based on woven fabric made with a novel fiber design. Polymer fiber extrusion systems permit direct fabrication from raw materials in easily scalable process.

hour (per draw tower). In contrast, the textile industry readily processes raw material into fiber at a rate of metric tons per hour *from a single machine*. The vast majority of synthetic textile fibers are made of thermoplastic polymers using melt extrusion through specialty dies called *spinnerets* with the continuously melted and delivered by screw extruders. Although such large-scale production systems typically occupy tens to hundreds of square meters in footprint, production-scale draw towers with conservatively estimated footprints of a single square meter would need to process tens of kilograms per hour to match the mass throughput of the textile industry.

Screw extrusion, as briefly discussed in Chapter 2, differs from ram extrusion by the mechanisms for heating, transporting, and forcing the extruded material through the die and into the finished morphology. In particular, whereas ram extrusion can be used for a wider range of materials and even performed at room-temperature, screw extrusion is typically limited to the thermoforming of polymers or the precipitation of filaments from liquid solutions. This is due to the high shear imparted by the screw on the material. In fact, shear on the material primarily drives the heating and melting process by a phenomenon known as *viscous dissipation*. Elastic deformation of the viscous melt increases internal energy thereby raising the temperature under constant shear and driving the melt to a lower viscosity. For non-Newtonian materials, such as most thermoplastic polymers, the shear itself will further reduce the viscosity. Combined, both effects in fact assist the extrusion process at large by reducing relative melt pressure for increasing production throughput. Screw extruders are readily integrated into a range of thermoforming manufacturing processes by design and installation of appropriate melt distribution system, extrusion die, and upstream/downstream support equipment. The ease of integration stems from the primary function and operation: input raw material, melt it, mix it, and meter (deliver) the melt on through to the next state. Sophisticated screw geometries, customization of the feed and metering mechanism, and internal atmospheric control are often found in specialty systems, but these should not obfuscate the simple input/output function served by these extruders.

The strategy for transitioning to multicomponent extrusion over thermal drawing for large-volume production of polymer fibers or textile applications is outlined in Figure 6.1. Especially in the case of textiles, the availability of proven industrial practices and downstream processes more than tips the scale in favor of fiber extrusion systems. The corollary to the availability of these systems, however, is that they typically are not easily accessible for small-batch laboratory-scale trials. A typical *small* production loom at a textile mill in North Carolina, for instance, requires about 6000 yarn ends precisely wound onto the warp beam (spools) that, when full, can total several hundred kilograms of fiber. Smaller woven fabric trial runs are possible, but are then only completed in the weft (fill) direction, resulting in a fabric sample containing prototype fiber along only one dimension.

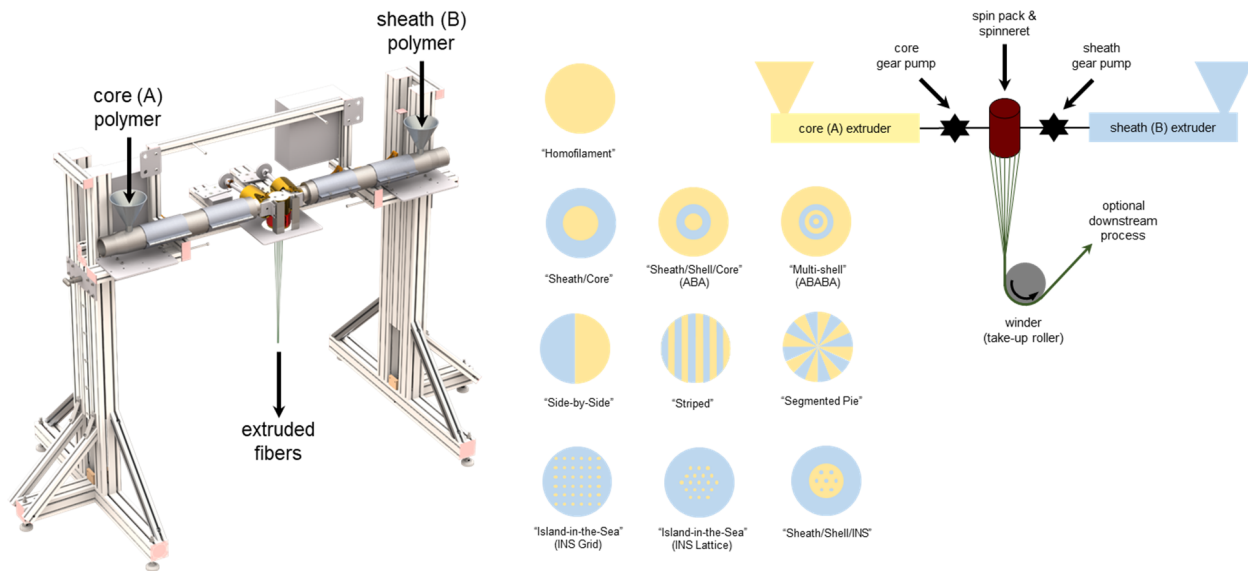


Figure 6.2: Schematic overview of laboratory scale bicomponent extrusion. (Left) Rendered image depicting multifilament extrusion from raw material. Spin pack at machine center houses the melt distribution technology and spinneret. (Center) Schematics of a subset of available off-the-shelf bicomponent cross-sections highlight radial and azimuthal control. (Right) Schematic overview of bicomponent extrusion with melt-metering gear pumps providing tight tolerance volumetric flow to the spinneret. Extruded fibers can be spun directly onto a spool (bobbin) or re-directed to downstream processes e.g. application of spin finish or cold-drawing.

Although thus far referred to by name, multicomponent extrusion has yet to be detailed as fabrication methodology. Mono-material fiber extrusion systems dominate the textile industry, as the need for structured multimaterial fibers is not typically required for commodity products. The breadth of thermoplastic polymers available satisfy most needs for small adjustments to fiber properties such as tensile strength, chemical resistance, etc. In some cases, multimaterial (multicomponent) fibers provide the additional functionalities required, especially in specialty textiles for filtration, medical applications, personal protective equipment, and anti-counterfeiting measures. Co-extrusion of two or more materials is more widely practiced by manufacturers of larger extruded goods such as long-haul cables, industrial wires, and the like. However, the small fiber diameters typically for textiles make it difficult to efficiently co-extrude custom architectures at production quantities without sacrificing modularity. Fortunately, commercially available and proprietary technology was developed to address this limitation. The manufacturer of this equipment has sophisticated the technology across multiple scales, from laboratory bicomponent (two-material) machines (Figure 6.2) with throughput of a few kilograms per hour, to full-scale production systems capable of continuous processing of metric tons per hour [101, 102].

### **6.1 Continuous Multifilament and Non-Woven Fabrics**

In a next step, the fibers were instead fabricated through melt spinning of multifilament threads once a suitable nanoparticle concentration was identified. With this method, the amount of sacrificial polymer sheath needed was reduced, although the sphere diameter distribution was increased compared to those produced from thermally drawn fiber.

To validate the bicomponent system, previously drawn fibers were instantiated into continuous multifilament yarns. As discussed in Chapter 2, polystyrene (PS) and cyclic olefin polymer (COP) are an attractive multimaterial fiber system as their negligible miscibility, selective solubility, high

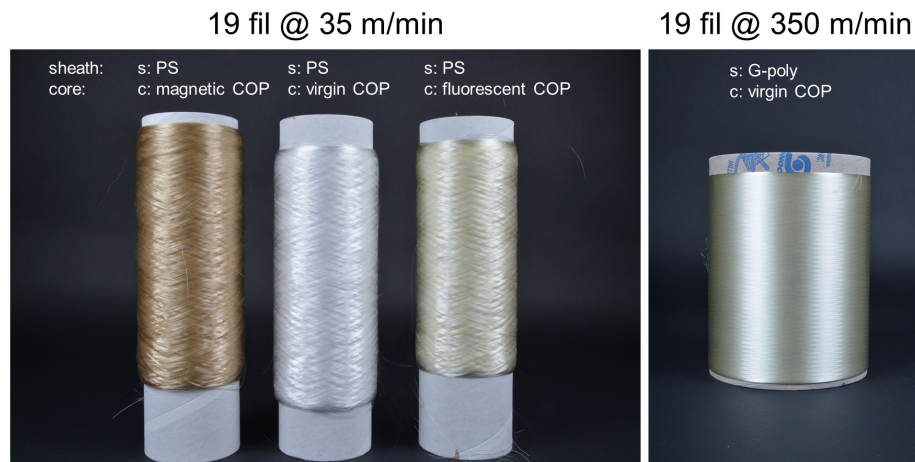


Figure 6.3: Spun fiber bobbins with 19 filaments per thread. The bobbins to the left are fiber architectures and compositions previously produced using thermal drawing from preforms. The bobbin on the right, however, has a G-polymer sheath that transitions rapidly to low viscosity and proved incompatible with the extrusion and drawing equipment described in earlier chapters.

transparency, and overlapping thermoviscous properties accommodate a range of functionalities in both the fiber and sphere form factors. However, in contrast to thermal drawing from preforms, fiber extrusion is not typically well suited for highly amorphous polymers due to their relatively high viscosity, low shear-thinning, and resistance to plastic deformation in the melt state (i.e. viscoelastic). However, as shown in Figure 6.3, multifilament threads were successfully produced with a simple sheath/core (cladding/core) structure at process speeds not typically achieved on the benchtop system or in the meso-scale polymer draw tower at CREOL. In addition to the PS/COP threads shown, a fourth bobbin highlights the broader range of polymer viscosity compatible with fiber extrusion. "G-polymer" is a commercially available specialty thermoplastic that is a modified polyvinyl alcohol (PVA). Standard PVA is not typically thermoplastic and therefore not easily adapted for thermoforming processes. However, PVA and its G-polymer derivative are water-soluble, making it an attractive alternative to PS as extraction of generated spheres, for instance, can be performed using tap water instead of harsh, hazardous, and expensive organic solvents. Additionally, the wind speed was increased an additional factor of ten to again highlight the faster linear speeds capable on these systems in addition to the larger mass throughput.



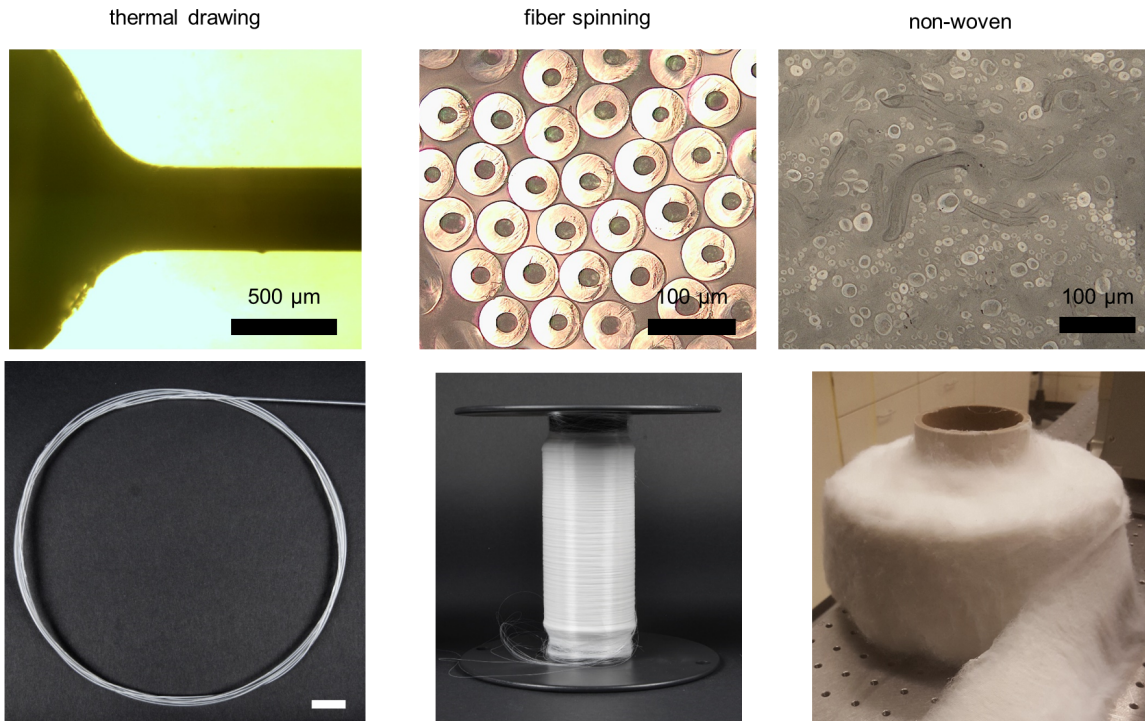


Figure 6.4: Each fiber depicted was produced directly from raw material (although the thermal drawing requires from extrusion and preform assembly. The core diameters in each are approximately 300  $\mu\text{m}$ , 50  $\mu\text{m}$ , and 10  $\mu\text{m}$  from left to right, respectively.

In a second validation step, the compounded fiber discussed in Chapter 5 was replicated in both multifilament and non-woven fabric form factors (Figure 6.4). The former follows directly based on the validation results just described. However, since the ultimate goal is produce functional spheres from these fibers for tunable scattering, the PS sheath was substituted for water-soluble thermoplastic resins to investigate the effect on break-up and to validate the less harsh extraction process. Non-woven fabrics is a general descriptor for extrusion of small diameter fibers (<50  $\mu\text{m}$ ) into a randomly oriented and entangled web. Two main types of non-woven fabrics directly result from melt extrusion systems: melt-blown and spunbond. In the former, a jet of hot air (air knife) at the spinneret forces the extruded filaments down onto a slow moving forming table. The air temperature both maintains the extruded melt in a softened state to draw-down to smaller diameters and also prevents cooling the spinneret thereby freezing the polymer and clogging the



on environmental changes to elicit color change. The key design feature that distinguishes those fabrics from these described here is the ability to locally change the temperature of the fibers on-demand. This active control is achieved by incorporating an electrical conductor within the fiber so that, through resistive heating, the temperature can be increased above the color change transition threshold by passing current through the conductor.

Fabricating such fibers comprising an electrical conductor encapsulated by polymer sheath loaded with thermochromic pigment can be achieved by a variety of methodologies. Practical considerations will tend to favor one fabrication approach over another, given the intended end-use of wearable textiles. For instance, industrial looms can handle a wide range of fiber (thread) sizes, but to achieve the tactile feel and appearance of fabric would require thread diameters below  $\approx 600\ \mu\text{m}$  while maintaining sufficient tensile strength. As always, scalability to industrial volumes is of keen interest.

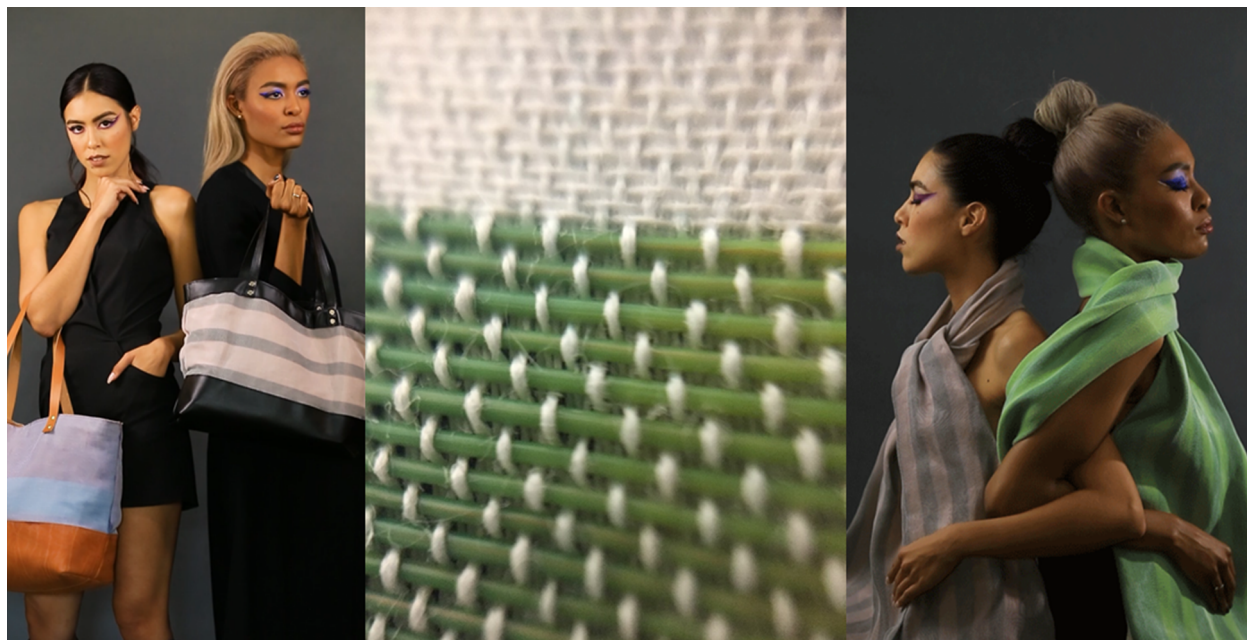


Figure 6.6: Photographs depicting textile garments and accessories produced using the thermochromic fabrics woven with novel extruded fibers.

Given that the general structure of these TC fibers mimics that of insulated electrical wires, a reasonable strategy would be to utilize common and established fabrication practices adopted by manufacturers of these wires. Most of these manufacturers would start with a large supply of bare conductor and then overcoat the sheath by either melt extrusion or thermal drawing (for thermoplastic) or by immersion coating and subsequent curing as in the case of PVC or enamel sheaths. However, this sort of process inherits the properties and limitations of the pre-fabricated precursor conductor, namely availability, mechanical strength, size, composition, and appearance among others.

That said, a first effort was initiated in which small diameter bare (uninsulated) copper wire was procured from commercial sources. The wire was passed through a melt coating spinneret in a ‘tubing’ configuration that applied a polymer sheath to the wire. The polymer used was a thermoplastic elastomer (TPE), selected for its flexible yet tear-resistant mechanical properties along with its thermal compatibility with the temperature-sensitive thermochromic pigment. Prior to extrusion, the pigment was compounded into a compatible host resin at high loading fraction into pellet form. These pellets were then mixed with virgin TPE pellets in the extruder hoppers so as to dilute the pigment to the desired volume fraction in the melt.

The coating-style spinneret features a small tube positioned at the center of a die aperture. The wire is passed through the bore of the needle and encounters the polymer melt that has been forced under pressure through the annulus formed by the inner wall of the die and the outer wall of the needle. This configuration is categorized as a tubing-style extrusion since the melt is forced into a hollow cylindrical cross-section that is then drawn down and collapsed onto the small-diameter wire. The counterpart to this configuration is the pressure-style process in which the melt is introduced to the wire internally within the spinneret and then subsequently co-extruded through a smaller diameter die aperture with no annulus (tube is recessed prior to the die entrance).



The resultant fibers exhibited color-changing behavior as anticipated. With sufficient quantity produced, often 35 km to 40 km on a single spool, the fiber was then shipped to an industry collaborator for weaving into fabric using a production-style textile loom. The fabrics were then cut, assembled, and connectorized into working wearable garments and accessories. Some examples are shown in Figure 6.6.

### 6.3 Capacitive Fibers for Electronic Textiles

Building from the thermochromic fabric work, in which a conductor is encapsulated in a sheath polymer impregnated with a functional additive, it became of interest to probe the utility of incorporating a structured bicomponent sheath along with adding a second conductive phase at the individual fiber level. One application that addresses a common concern among wearable technology is the ability to generate, store, and/or deliver electrical energy in the fabric itself. To that end, capacitive fibers were designed and fabricated featuring a two-shell sheath surrounding a small-diameter bare copper wire. The shells in the sheath are extruded onto the wire in a coating die as thinly as possible while maintaining good dimensional stability and uniformity along the length of the fiber.

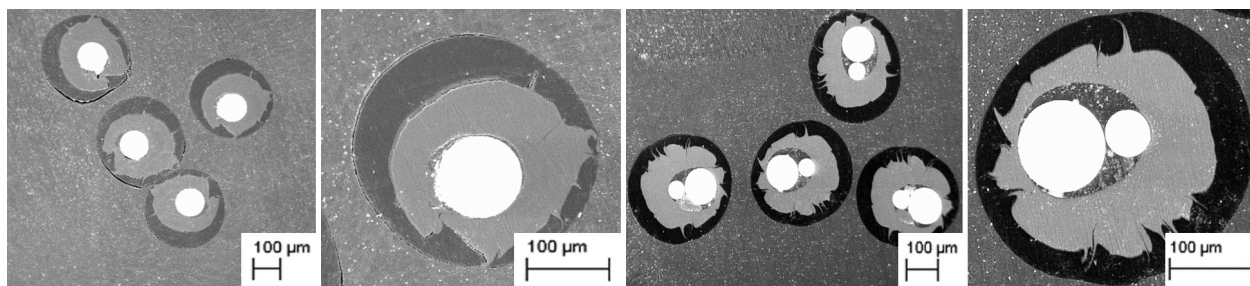


Figure 6.7: SEM micrographs depicting two different capacitive fibers zoomed-out and zoomed-in for each structure.

The capacitor structure was made into a single fiber with a single conductor by using carbon-doped polybutyl terephthalate (cPBT) in the outer shell and a virgin (undoped) thermoplastic dielectric in the inner shell in contact with the conductor (Figure 6.7). Various combinations of thermoplastics were investigated to identify compatible combinations that would stably extrude. Adding a second conductor with a thin enamel layer abutting the bare conductor was likewise produced. Inverting the shells so that the cPBT is in the inner region increases the surface area of the dielectric but requires a second processing step in which the original fiber is passed through the coating die along with a second bare copper wire. Both coated fiber and bare wire are then encapsulated in a bicomponent sheath with the cPBT again in the inner shell and the virgin polymer in the outer shell to act as an insulating sheath.

Initial characterization results from simple hand-woven fabrics show promising results as a measurable change in capacitance was observed (Figure 6.8). The work is currently ongoing, process improvements expected to elicit larger signals. Additionally, in place of the hand-woven fabrics, larger quantities of fiber will be sent to industry collaborator for weaving on a textile loom in a similar fashion as the thermochromic fabrics.

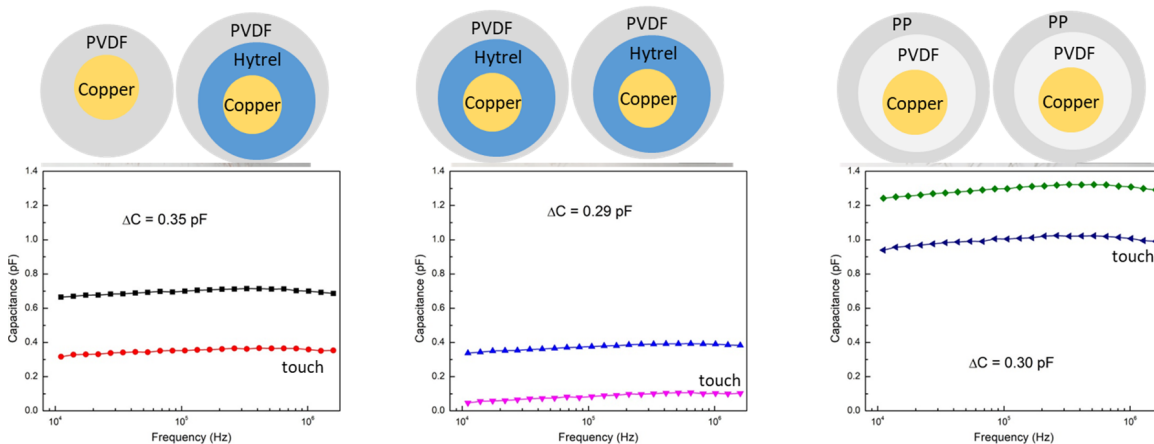


Figure 6.8: Data plots depicting change in capacitance for hand-woven fabrics assembled with the fiber architecture and composition shown above each plot. The pair of cross-sections represent the repeating pattern unit in the fabric.

## CHAPTER 7: DISCUSSION

Rapid-prototyping of multimaterial fibers on a benchtop scale enables efficient validation of novel fiber structures and material systems. The simplicity yet robustness of the system developed overcomes the intimidating entry barrier presented by traditional fiber optic manufacturing systems and larger-scale ram extruders. The system touts a raw-material-to-drawn-fiber production cycle in as little as a few hours consuming mere tens of grams while producing less than 10% waste. It is compatible with a broad range of thermoplastic materials with extrusion temperatures up to 330 °C and draw temperatures up to 450 °C. In the current configuration, preform volumes as large as 150 cm<sup>3</sup> are capably produced, resulting in mm-scale fiber diameter with lengths in the tens of meters. Tolerances have been demonstrated to better than a few percent variation per meter of fiber. Extrusion dies are highly modular. The current configuration employs die aperture diameters of 1.5 mm, 3 mm, 4.5 mm, and 16 mm. Adjusting the extrusion parameters permits extrudate diameters ranging from 1 mm to 6 mm with the smaller diameter die set, and 12 mm to 18 mm with the large die. Custom profiles are quickly validated by machining of an appropriate die with compatible external dimensions. The system is adaptable for longer extrudate lengths if needed by increasing the heating block height, support stand legs, extruder sleeve, and ram shaft length. Vacuum levels and maximum have proven sufficient to extrude consolidated rods reproducibly. The benchtop draw tower is similarly modular, with multiple fiber pulling systems proven to date. Increased quenching and preform length is readily achieved by increasing the support stand legs, furnace geometry, and linear positioning system accordingly.

Using the benchtop system, an all-polymer light pipe was produced to validate the efficacy of the process to reproduce fiber architectures previously proven on larger scale machines. Novel fiber systems were additionally produced, specifically extruded rods and drawn fibers with high-concentration functional additives otherwise too costly or limited in availability to extrude in larger

systems. From these rods, complexly structured preforms were assembled and subsequently drawn into fiber. Spheres generated by harnessing capillary instabilities in these fibers inherited the complex structuring to produce unprecedented compartmentalization of multiple moieties on a micro- and nano-scale. The benchtop methodology for rapid-prototyping was further extended to 3D-printing of yet more complexly structured preform architectures by first extruding and then drawing custom functionalized filaments. Despite the added processing steps of extruding rods and then drawing into fiber for the ultimate goal of drawing a second fiber, this methodology proves still more rapid and efficient for sufficiently complex structures that are too difficult to machine or extrude directly.

Stepping up in technical impact, subsequent work combined the mechanical robustness of a thermally drawn engineering plastic with the dimensional tolerances, material purity, and process refinement exhibited by commercially available step-index chalcogenide canes. The resulting hybrid fabrication strategy produced robust optical fibers for use in mid-IR applications. These fibers demonstrated record-high power delivery at  $1.95\ \mu\text{m}$  and survived intensities up to  $12\ \text{MW}/\text{cm}^2$  on a solid-core single-mode fiber. Additionally, the large surface area and favorable adhesive properties of the polymer jacket enabled deposition of AR coatings that were not only effective but also mechanically robust, boosting transmission to near 100% and surviving a barrage of military specified abrasion testing, respectively. The modularity of the thermal drawing process enabled fabrication of larger core fibers as well without increasing the overall diameter of the fiber. These large core fibers exhibited similarly low transmission losses and power handling capabilities. To better characterize the limits, modeling and simulation efforts were executed and experimentally validated to identify the primary mechanisms for catastrophic failure. Optical failures were identified as primarily SBS related, especially for single-mode fibers over one meter in length. Additional modeling was presented from a submitted manuscript describing an efficient free-space coupling scheme for a QCL source. Better than 70% coupling efficiency was achieved between the 0.82



NA of the QCL and the 0.2 NA of the fiber. Over 89% of the coupled radiation was transmitted through a 1 m long length of fiber.

A subsequent step in technical impact involved the thermal co-drawing of a functioning optoelectronic fiber device. Despite the technical complexity of the system, the process is fully scalable as the methodology employed utilized proven academic and industrial practices readily implemented in the ceramic sciences and optical fiber manufacturing industries. The device fiber contained an axially continuous germanium core with metallic electrodes maintaining electrical connectivity along the entire length of fiber. The fiber was the first of its kind in that a traditional semiconductor was co-drawn with metal wires in intimate electrical contact. The structure was only feasible due to the innovative implementation of an electrically conductive amorphous glass composite that acted as a viscous barrier during the draw to prevent detrimental mixing of the crystalline phases. The composite itself exhibited record-high bulk conductivity at room temperature due to the advantageous dual purpose of the organic surfactant used. In addition to promoting excellent dispersion of the CNF additive, the surfactant carbonized *in situ* thereby boosting the background conductivity of the glass and increasing CNF conductivity when loaded to concentrations at or below the percolation threshold. Photoconductivity measurements of the device fiber were indicative of the expected semiconductor behavior, and inspire confidence in continuing the line of investigation in the near future.

Transitioning from multimaterial fibers as the end-use device, designer composite microspheres were developed that exhibited tunable control over the distribution of scattered optical power. The microspheres were produced using the aforementioned capillary instability method from functionalized composite fibers with well-dispersed and well-distributed titania nanoparticles. Optical experiments were performed on a single isolated microsphere at a time, and conclusively demonstrated the ability to diffusively scatter incident optical power in either the forward or backward direction by changing the sphere diameter while fixing the nanoparticle inclusion concentration.

The microspheres consequently behaved in a manner similar to a granular material in a spherical morphology. Additionally, the redistribution of energy mimicked that of a molecular dipole apart from not maintaining the polarization state of the incident field in the process. In this way, the microspheres can loosely be characterized as "macroscopic" dipoles with a two-material composition.

The final effort described deals with the transition of these multimaterial fiber fabrication strategies to larger scale production systems typical of pilot scale manufacturing in the textile industry. Melt extrusion systems represent the vast majority of global manufacturing for polymer fibers. A commercially available system was procured that contains specialized proprietary melt distribution technology that essentially pixelates the cross-section of extruded fibers. This system is readily adapted to industry proven techniques and practices, including the extrusion of continuous multifilament threads, monofilament, non-woven fabrics, wire-coating, and cable-jacketing. Fibers produced from this system readily integrate with equally established downstream processing techniques. Demonstrated here is the development of novel co-extruded fibers for production of user-controlled color-changing fabrics. These fibers were woven into fabric by industrial looms and formed into clothing articles. Additionally, the composite spheres previously developed using thermal drawing were instead produced from extruded fibers, producing unprecedented yield of spheres as a function of sheath-to-core diameter and mass ratio. This represents a potentially viable methodology for scaling production of in-fiber sphere fabrication for commercial use. Finally, initial results were presented of capacitive fibers that could be similarly woven into fabric for potential use in e-textiles.

## REFERENCES

- [1] E. Kvavadze, O. Bar-Yosef, A. Belfer-Cohen, E. Boaretto, N. Jakeli, Z. Matskevich, and T. Meshveliani, “30,000-Year-Old Wild Flax Fibers,” *Science*, vol. 325, no. 5946, pp. 1359–1359, Sep. 11, 2009.
- [2] E. J. W. Barber, *Prehistoric Textiles: The Development of Cloth in the Neolithic and Bronze Ages with Special Reference to the Aegean*, 3. print., for the Princeton paperback ed. Princeton, N.J.: Princeton Univ. Press, 1992, 471 pp., OCLC: 832146314.
- [3] M. Decker, C. Halbach, C. Nam, N. Wagner, and E. Wetzal, “Stab resistance of shear thickening fluid (STF)-treated fabrics,” *Composites Science and Technology*, vol. 67, no. 3-4, pp. 565–578, Mar. 2007.
- [4] A. L. Alesi, V. E. Stimpert, and R. A. Gagne, “Body Armor Construction,” U.S. Patent 3,897,239, Feb. 18, 1975.
- [5] C. B. Weldon, J. H. Tsui, S. A. Shankarappa, V. T. Nguyen, M. Ma, D. G. Anderson, and D. S. Kohane, “Electrospun drug-eluting sutures for local anesthesia,” *Journal of Controlled Release*, vol. 161, no. 3, pp. 903–909, Aug. 2012.
- [6] S. Rajendran and S. C. Anand, “DEVELOPMENTS IN MEDICAL TEXTILES,” *Textile Progress*, vol. 32, no. 4, pp. 1–42, Dec. 2002.
- [7] K. Yoon, B. S. Hsiao, and B. Chu, “Functional nanofibers for environmental applications,” *Journal of Materials Chemistry*, vol. 18, no. 44, p. 5326, 2008.
- [8] A. Mouritz, M. Bannister, P. Falzon, and K. Leong, “Review of applications for advanced three-dimensional fibre textile composites,” *Composites Part A: Applied Science and Manufacturing*, vol. 30, no. 12, pp. 1445–1461, Dec. 1999.

- [9] T. F. Cooke, "Inorganic Fibers-A Literature Review," *Journal of the American Ceramic Society*, vol. 74, no. 12, pp. 2959–2978, Dec. 1991.
- [10] A. Papadopoulos, "State of the art in thermal insulation materials and aims for future developments," *Energy and Buildings*, vol. 37, no. 1, pp. 77–86, Jan. 2005.
- [11] E. T. Thostenson, Z. Ren, and T.-W. Chou, "Advances in the science and technology of carbon nanotubes and their composites: A review," *Composites Science and Technology*, vol. 61, no. 13, pp. 1899–1912, Oct. 2001.
- [12] R. Dastjerdi and M. Montazer, "A review on the application of inorganic nano-structured materials in the modification of textiles: Focus on anti-microbial properties," *Colloids and Surfaces B: Biointerfaces*, vol. 79, no. 1, pp. 5–18, Aug. 2010.
- [13] R. Fan, R. Karnik, M. Yue, D. Li, A. Majumdar, and P. Yang, "DNA Translocation in Inorganic Nanotubes," *Nano Letters*, vol. 5, no. 9, pp. 1633–1637, Sep. 2005.
- [14] P. Greil, "Active-Filler-Controlled Pyrolysis of Pre-ceramic Polymers," *Journal of the American Ceramic Society*, vol. 78, no. 4, pp. 835–848, Apr. 1995.
- [15] L. Rapoport, N. Fleischer, and R. Tenne, "Applications of WS<sub>2</sub>(MoS<sub>2</sub>) inorganic nanotubes and fullerene-like nanoparticles for solid lubrication and for structural nanocomposites," *Journal of Materials Chemistry*, vol. 15, no. 18, p. 1782, 2005.
- [16] Y. Fink, J. N. Winn, S. Fan, C. Chen, J. Michel, J. D. Joannopoulos, and E. L. Thomas, "A Dielectric Omnidirectional Reflector," *Science*, vol. 282, no. 5394, pp. 1679–1682, Nov. 1998.
- [17] S. Johnson, M. Ibanescu, M. Skorobogatiy, O. Weisberg, T. Engeness, M. Soljacic, S. Jacobs, J. Joannopoulos, and Y. Fink, "Low-loss asymptotically single-mode propagation in large-core OmniGuide fibers," *Optics Express*, vol. 9, no. 13, p. 748, Dec. 17, 2001.

- [18] D. Torres, O. Weisberg, G. Shapira, C. Anastassiou, B. Temelkuran, M. Shurgalin, S. A. Jacobs, R. U. Ahmad, T. Wang, U. Kolodny, S. M. Shapshay, Z. Wang, A. K. Devaiah, U. D. Upadhyay, and J. A. Koufman, “OmniGuide photonic bandgap fibers for flexible delivery of CO<sub>2</sub> laser energy for laryngeal and airway surgery,” presented at the Biomedical Optics 2005, K. E. Bartels, L. S. Bass, W. T. W. de Riese, K. W. Gregory, H. Hirschberg, A. Katzir, N. Kollias, S. J. Madsen, R. S. Malek, K. M. McNally-Heintzelman, L. P. Tate Jr., E. A. Trowers, and B. J.-F. Wong, Eds., San Jose, CA, Apr. 25, 2005, p. 310.
- [19] A. F. Abouraddy, M. Bayindir, G. Benoit, S. D. Hart, K. Kuriki, N. Orf, O. Shapira, F. Sorin, B. Temelkuran, and Y. Fink, “Towards multimaterial multifunctional fibres that see, hear, sense and communicate,” *Nature Materials*, vol. 6, no. 5, pp. 336–347, May 2007.
- [20] G. Tao, A. M. Stolyarov, and A. F. Abouraddy, “Multimaterial Fibers,” *International Journal of Applied Glass Science*, vol. 3, no. 4, pp. 349–368, Dec. 2012.
- [21] M. A. Schmidt, A. Argyros, and F. Sorin, “Hybrid Optical Fibers – An Innovative Platform for In-Fiber Photonic Devices,” *Advanced Optical Materials*, vol. 4, no. 1, pp. 13–36, 2016.
- [22] S. Egusa, Z. Wang, N. Chocat, Z. M. Ruff, A. M. Stolyarov, D. Shemuly, F. Sorin, P. T. Rakich, J. D. Joannopoulos, and Y. Fink, “Multimaterial piezoelectric fibres,” *Nature Materials*, vol. 9, no. 8, pp. 643–648, Aug. 2010.
- [23] W. Zeng, L. Shu, Q. Li, S. Chen, F. Wang, and X.-M. Tao, “Fiber-Based Wearable Electronics: A Review of Materials, Fabrication, Devices, and Applications,” *Advanced Materials*, vol. 26, no. 31, pp. 5310–5336, Aug. 2014.
- [24] F. A. Tan, A. F. Abouraddy, and D. Kocak, “Underwater fiber optic cable with a predetermined buoyancy and associated methods,” pat. 10,001,616, Jun. 19, 2018.
- [25] J. A. Covas and P. Costa, “A miniature extrusion line for small scale processing studies,” *Polymer Testing*, vol. 23, no. 7, pp. 763–773, Oct. 2004.

- [26] S. Guns, V. Mathot, J. A. Martens, and G. Van den Mooter, “Upscaling of the hot-melt extrusion process: Comparison between laboratory scale and pilot scale production of solid dispersions with miconazole and Kollicoat® IR,” *European Journal of Pharmaceutics and Biopharmaceutics*, vol. 81, no. 3, pp. 674–682, Aug. 2012.
- [27] W. Michaeli, “Computation of Velocity and Temperature Distributions in Extrusion Dies,” in *Extrusion Dies for Plastics and Rubber: Design and Engineering Computations*, 3., rev. ed, OCLC: 249673553, München: Hanser, 2003, pp. 78–139.
- [28] I. N. Bronshtæin, *Handbook of mathematics*. Berlin; New York: Springer, 2007, OCLC: 739127546. [Online]. Available: <http://www.myilibrary.com?id=135274> (visited on 06/29/2019).
- [29] H. H. Rosenbrock, “An Automatic Method for Finding the Greatest or Least Value of a Function,” *The Computer Journal*, vol. 3, no. 3, pp. 175–184, Mar. 1, 1960.
- [30] R. Hooke and T. A. Jeeves, ““ Direct Search” Solution of Numerical and Statistical Problems,” *Journal of the ACM*, vol. 8, no. 2, pp. 212–229, Apr. 1, 1961.
- [31] R. Fletcher, M. J. Box, D. Davies, and W. H. Swann, “Mathematical and Statistical Techniques for Industry, ICI Monograph No. 5, "Non Linear Optimization Techniques",” *The Mathematical Gazette*, vol. 54, no. 390, p. 436, Dec. 1970.
- [32] J. A. Nelder and R. Mead, “A Simplex Method for Function Minimization,” *The Computer Journal*, vol. 7, no. 4, pp. 308–313, Jan. 1, 1965.
- [33] H.-P. Schwefel, *Evolution and Optimum Seeking*, ser. Sixth-Generation Computer Technology Series. New York: Wiley, 1995, 444 pp., OCLC: 610873120.
- [34] X. Yao and Y. Xu, “Recent Advances in Evolutionary Computation,” *Journal of Computer Science and Technology*, vol. 21, no. 1, pp. 1–18, Jan. 2006.

- [35] T. Bäck and H.-P. Schwefel, “An Overview of Evolutionary Algorithms for Parameter Optimization,” *Evolutionary Computation*, vol. 1, no. 1, pp. 1–23, Mar. 1993.
- [36] G. Tao, S. Shabahang, E.-H. Banaei, J. J. Kaufman, and A. F. Abouraddy, “Multimaterial preform coextrusion for robust chalcogenide optical fibers and tapers,” *Optics Letters*, vol. 37, no. 13, p. 2751, Jul. 2012.
- [37] J. J. Kaufman, R. Ottman, G. Tao, S. Shabahang, E.-H. Banaei, X. Liang, S. G. Johnson, Y. Fink, R. Chakrabarti, and A. F. Abouraddy, “In-fiber production of polymeric particles for biosensing and encapsulation,” *Proceedings of the National Academy of Sciences*, vol. 110, no. 39, pp. 15 549–15 554, Sep. 2013.
- [38] R. Kostecki, H. Ebendorff-Heidepriem, S. C. Warren-Smith, and T. M. Monro, “Predicting the drawing conditions for Microstructured Optical Fiber fabrication,” *Optical Materials Express*, vol. 4, no. 1, p. 29, Jan. 2014.
- [39] U. C. Paek and C. R. Kurkjian, “Calculation of Cooling Rate and Induced Stresses in Drawing of Optical Fibers,” *Journal of the American Ceramic Society*, vol. 58, no. 7, pp. 330–335, Jul. 1975.
- [40] F. T. Geyling, “Basic Fluid-Dynamic Considerations in the Drawing of Optical Fibers,” *Bell System Technical Journal*, vol. 55, no. 8, pp. 1011–1056, Oct. 1976.
- [41] U. C. Paek and R. B. Runk, “Physical behavior of the neck-down region during furnace drawing of silica fibers,” *Journal of Applied Physics*, vol. 49, no. 8, pp. 4417–4422, Aug. 1978.
- [42] H. M. Reeve and A. M. Mescher, “Effect of unsteady natural convection on the diameter of drawn polymer optical fiber,” *Optics Express*, vol. 11, no. 15, p. 1770, Jul. 2003.

- [43] H. M. Reeve, A. M. Mescher, and A. F. Emery, "Investigation of Steady-State Drawing Force and Heat Transfer in Polymer Optical Fiber Manufacturing," *Journal of Heat Transfer*, vol. 126, no. 2, p. 236, 2004.
- [44] F. DiMarcello, C. Kurkjian, and J. Williams, "Fiber Drawing and Strength Properties," in *Optical Fiber Communications*, T. LI, Ed., Orlando, FL, USA: Elsevier, 1985, pp. 179–248.
- [45] S. Roy Choudhury and Y. Jaluria, "Practical aspects in the drawing of an optical fiber," *Journal of Materials Research*, vol. 13, no. 2, pp. 483–493, Feb. 1998.
- [46] A. Mawardi and R. Pitchumani, "Optical Fiber Drawing Process Model Using an Analytical Neck-Down Profile," *IEEE Photonics Journal*, vol. 2, no. 4, pp. 620–629, Aug. 2010.
- [47] S. Roy Choudhury and Y. Jaluria, "Thermal transport due to material and gas flow in a furnace for drawing an optical fiber," *Journal of Materials Research*, vol. 13, no. 2, pp. 494–503, Feb. 1998.
- [48] Y. K. Kim, J. S. Choi, H. S. Kwak, and K. Kim, "Numerical modeling and analysis of glass fiber drawing process from large sized silica preform," *Journal of Thermal Science and Technology*, vol. 12, no. 2, JTST0030–JTST0030, 2017.
- [49] U. C. Paek, "Free Drawing and Polymer Coating of Silica Glass Optical Fibers," *Journal of Heat Transfer*, vol. 121, no. 4, p. 774, 1999.
- [50] X. Lu, "Experimental and analytical investigation of nonisothermal viscoelastic glass fiber drawing," Dissertation, University of Michigan, 1999. [Online]. Available: <http://hdl.handle.net/2027.42/131716>.
- [51] A. Fitt, K. Furusawa, T. Monro, and C. Please, "Modeling the fabrication of hollow fibers: Capillary drawing," *Journal of Lightwave Technology*, vol. 19, no. 12, pp. 1924–1931, 2001.



- [52] J. J. Kaufman, G. Tao, S. Shabahang, E.-H. Banaei, D. S. Deng, X. Liang, S. G. Johnson, Y. Fink, and A. F. Abouraddy, “Structured spheres generated by an in-fibre fluid instability,” *Nature*, vol. 487, no. 7408, pp. 463–467, Jul. 2012.
- [53] M. Elsabahy and K. L. Wooley, “Design of polymeric nanoparticles for biomedical delivery applications,” *Chemical Society Reviews*, vol. 41, no. 7, p. 2545, 2012.
- [54] B. P. Timko, K. Whitehead, W. Gao, D. S. Kohane, O. Farokhzad, D. Anderson, and R. Langer, “Advances in Drug Delivery,” *Annual Review of Materials Research*, vol. 41, no. 1, pp. 1–20, Aug. 4, 2011.
- [55] J. Wang, G. Liu, and G. Rivas, “Encoded Beads for Electrochemical Identification,” *Analytical Chemistry*, vol. 75, no. 17, pp. 4667–4671, Sep. 2003.
- [56] S.-H. Kim, S. Y. Lee, and S.-M. Yang, “Janus Microspheres for a Highly Flexible and Impregnable Water-Repelling Interface,” *Angewandte Chemie International Edition*, vol. 49, no. 14, pp. 2535–2538, Mar. 29, 2010.
- [57] G. Tao, J. J. Kaufman, S. Shabahang, R. Rezvani Naraghi, S. V. Sukhov, J. D. Joannopoulos, Y. Fink, A. Dogariu, and A. F. Abouraddy, “Digital design of multimaterial photonic particles,” *Proceedings of the National Academy of Sciences*, vol. 113, no. 25, pp. 6839–6844, Jun. 2016.
- [58] S. Shabahang, M. P. Marquez, G. Tao, M. U. Piracha, D. Nguyen, P. J. Delfyett, and A. F. Abouraddy, “Octave-spanning infrared supercontinuum generation in robust chalcogenide nanotapers using picosecond pulses,” *Optics Letters*, vol. 37, no. 22, p. 4639, Nov. 2012.
- [59] S. B. Mirov, I. S. Moskalev, S. Vasilyev, V. Smolski, V. V. Fedorov, D. Martyshkin, J. Peppers, M. Mirov, A. Dergachev, and V. Gapontsev, “Frontiers of Mid-IR Lasers Based on Transition Metal Doped Chalcogenides,” *IEEE Journal of Selected Topics in Quantum Electronics*, vol. 24, no. 5, pp. 1–29, Sep. 2018.

- [60] E. A. Romanova, S. Korsakova, M. Komanec, T. Nemecek, A. Velmuzhov, M. Sukhanov, and V. S. Shiryaev, “Multimode Chalcogenide Fibers for Evanescent Wave Sensing in the Mid-IR,” *IEEE Journal of Selected Topics in Quantum Electronics*, vol. 23, no. 2, pp. 289–295, Mar. 2017.
- [61] B. Bureau, C. Boussard, S. Cui, R. Chahal, M. L. Anne, V. Nazabal, O. Sire, O. Loréal, P. Lucas, V. Monbet, J.-L. Doualan, P. Camy, H. Tariel, F. Charpentier, L. Quetel, J.-L. Adam, and J. Lucas, “Chalcogenide optical fibers for mid-infrared sensing,” *Optical Engineering*, vol. 53, no. 2, p. 027 101, Feb. 2014.
- [62] G. E. Snopatin, V. S. Shiryaev, V. G. Plotnichenko, E. M. Dianov, and M. F. Churbanov, “High-purity chalcogenide glasses for fiber optics,” *Inorganic Materials*, vol. 45, no. 13, pp. 1439–1460, Dec. 2009.
- [63] G. Tao, H. Ebendorff-Heidepriem, A. M. Stolyarov, S. Danto, J. V. Badding, Y. Fink, J. Ballato, and A. F. Abouraddy, “Infrared fibers,” *Advances in Optics and Photonics*, vol. 7, no. 2, p. 379, Jun. 2015.
- [64] S. Shabahang, F. A. Tan, J. D. Perlstein, G. Tao, O. Alvarez, F. Chenard, A. Sincore, L. Shah, M. C. Richardson, K. L. Schepler, and A. F. Abouraddy, “Robust multimaterial chalcogenide fibers produced by a hybrid fiber-fabrication process,” *Optical Materials Express*, vol. 7, no. 7, p. 2336, Jul. 2017.
- [65] S. Shabahang, G. Tao, J. J. Kaufman, Y. Qiao, L. Wei, T. Bouchenot, A. P. Gordon, Y. Fink, Y. Bai, R. S. Hoy, and A. F. Abouraddy, “Controlled fragmentation of multimaterial fibres and films via polymer cold-drawing,” *Nature*, vol. 534, no. 7608, pp. 529–533, Jun. 2016.
- [66] A. Sincore, J. Cook, F. Tan, A. El Halawany, A. Riggins, S. McDaniel, G. Cook, D. V. Martyshkin, V. V. Fedorov, S. B. Mirov, L. Shah, A. F. Abouraddy, M. C. Richardson, and K. L. Schepler, “High power single-mode delivery of mid-infrared sources through chalcogenide fiber,” *Optics Express*, vol. 26, no. 6, p. 7313, Mar. 2018.

- [67] A. Sincore, J. Cook, F. Tan, A. F. Abouraddy, M. C. Richardson, and K. L. Schepler, “Practical limits of power transmission through single-mode chalcogenide fibers,” *Optical Engineering*, vol. 57, no. 11, p. 1, Nov. 2018.
- [68] Y. Bai, N. Bandyopadhyay, S. Tsao, S. Slivken, and M. Razeghi, “Room temperature quantum cascade lasers with 27% wall plug efficiency,” *Applied Physics Letters*, vol. 98, no. 18, p. 181 102, May 2, 2011.
- [69] P. Figueiredo, M. Suttinger, R. Go, E. Tsvid, C. K. N. Patel, and A. Lyakh, “Progress in high-power continuous-wave quantum cascade lasers [Invited],” *Applied Optics*, vol. 56, no. 31, H15, Nov. 1, 2017.
- [70] J. M. Kriesel, G. M. Hagglund, N. Gat, V. Spagnolo, and P. Patimisco, “Spatial mode filtering of mid-infrared (mid-IR) laser beams with hollow core fiber optics,” presented at the SPIE OPTO, M. Razeghi, E. Tournié, and G. J. Brown, Eds., San Francisco, California, United States, Dec. 18, 2013, p. 89930V.
- [71] Z. Li, C. Shi, and W. Ren, “Mid-infrared multimode fiber-coupled quantum cascade laser for off-beam quartz-enhanced photoacoustic detection,” *Optics Letters*, vol. 41, no. 17, p. 4095, Sep. 1, 2016.
- [72] P. Patimisco, V. Spagnolo, M. S. Vitiello, A. Tredicucci, G. Scamarcio, C. M. Bledt, and J. A. Harrington, “Coupling external cavity mid-IR quantum cascade lasers with low loss hollow metallic/dielectric waveguides,” *Applied Physics B*, vol. 108, no. 2, pp. 255–260, Aug. 2012.
- [73] V. Spagnolo, P. Patimisco, S. Borri, G. Scamarcio, B. E. Bernacki, and J. Kriesel, “Mid-infrared fiber-coupled QCL-QEPAS sensor,” *Applied Physics B*, vol. 112, no. 1, pp. 25–33, Aug. 2013.

- [74] A. Sampaolo, P. Patimisco, J. M. Kriesel, F. K. Tittel, G. Scamarcio, and V. Spagnolo, "Single mode operation with mid-IR hollow fibers in the range 5.1-10.5  $\mu\text{m}$ ," *Optics Express*, vol. 23, no. 1, p. 195, Jan. 12, 2015.
- [75] J. Cook, F. A. Tan, A. El Halawany, A. Sincore, L. Shah, A. F. Abouraddy, M. Richardson, and K. L. Schepler, "Efficient coupling of a quantum cascade laser to a few-mode chalcogenide fiber," Manuscript submitted for review on Jun. 6, 2019.
- [76] C. Markos, I. Kubat, and O. Bang, "Hybrid polymer photonic crystal fiber with integrated chalcogenide glass nanofilms," *Scientific Reports*, vol. 4, no. 1, p. 6057, May 2015.
- [77] C. Markos, J. C. Travers, A. Abdolvand, B. J. Eggleton, and O. Bang, "Hybrid photonic-crystal fiber," *Reviews of Modern Physics*, vol. 89, no. 4, p. 045 003, Nov. 27, 2017.
- [78] W. Yan, A. Page, T. Nguyen-Dang, Y. Qu, F. Sordo, L. Wei, and F. Sorin, "Advanced Multimaterial Electronic and Optoelectronic Fibers and Textiles," *Advanced Materials*, vol. 31, no. 1, p. 1 802 348, 2019.
- [79] R. He, P. J. A. Sazio, A. C. Peacock, N. Healy, J. R. Sparks, M. Krishnamurthi, V. Gopalan, and J. V. Badding, "Integration of gigahertz-bandwidth semiconductor devices inside microstructured optical fibres," *Nature Photonics*, vol. 6, no. 3, pp. 174–179, Mar. 2012.
- [80] M. Ordu, J. Guo, B. Tai, M. K. Hong, S. Erramilli, S. Ramachandran, and S. N. Basu, "Mid-infrared transmission through germanium-core borosilicate glass-clad semiconductor fibers," *Optical Materials Express*, vol. 7, no. 9, p. 3107, Sep. 1, 2017.
- [81] X. Ji, R. L. Page, S. Chaudhuri, W. Liu, S.-Y. Yu, S. E. Mohny, J. V. Badding, and V. Gopalan, "Single-Crystal Germanium Core Optoelectronic Fibers," *Advanced Optical Materials*, vol. 5, no. 1, p. 1 600 592, Jan. 2017.

- [82] L. Wei, C. Hou, E. Levy, G. Lestoquoy, A. Gumennik, A. F. Abouraddy, J. D. Joannopoulos, and Y. Fink, “Optoelectronic Fibers via Selective Amplification of In-Fiber Capillary Instabilities,” *Advanced Materials*, vol. 29, no. 1, p. 1 603 033, Jan. 2017.
- [83] M. Bayindir, A. F. Abouraddy, F. Sorin, J. D. Joannopoulos, and Y. Fink, “Detectors: Fiber Photodetectors Codrawn From Conducting, Semiconducting and Insulating Materials,” *Optics and Photonics News*, vol. 15, no. 12, p. 24, Dec. 2004.
- [84] M. Bayindir, F. Sorin, A. F. Abouraddy, J. Viens, S. D. Hart, J. D. Joannopoulos, and Y. Fink, “Metal–insulator–semiconductor optoelectronic fibres,” *Nature*, vol. 431, no. 7010, pp. 826–829, Oct. 2004. pmid: 15483607.
- [85] F. Sorin, A. F. Abouraddy, N. Orf, O. Shapira, J. Viens, J. Arnold, J. D. Joannopoulos, and Y. Fink, “Multimaterial Photodetecting Fibers: A Geometric and Structural Study,” *Advanced Materials*, vol. 19, no. 22, pp. 3872–3877, Nov. 2007.
- [86] M. Bayindir, O. Shapira, D. Saygin-Hinczewski, J. Viens, A. F. Abouraddy, J. D. Joannopoulos, and Y. Fink, “Integrated fibres for self-monitored optical transport,” *Nature Materials*, vol. 4, no. 11, pp. 820–825, Nov. 2005.
- [87] F. Sorin, O. Shapira, A. F. Abouraddy, M. Spencer, N. D. Orf, J. D. Joannopoulos, and Y. Fink, “Exploiting Collective Effects of Multiple Optoelectronic Devices Integrated in a Single Fiber,” *Nano Letters*, vol. 9, no. 7, pp. 2630–2635, Jul. 2009.
- [88] N. Chocat, G. Lestoquoy, Z. Wang, D. M. Rodgers, J. D. Joannopoulos, and Y. Fink, “Piezoelectric Fibers for Conformal Acoustics,” *Advanced Materials*, vol. 24, no. 39, pp. 5327–5332, Oct. 2012.
- [89] A. M. Stolyarov, L. Wei, F. Sorin, G. Lestoquoy, J. D. Joannopoulos, and Y. Fink, “Fabrication and characterization of fibers with built-in liquid crystal channels and electrodes for

- transverse incident-light modulation,” *Applied Physics Letters*, vol. 101, no. 1, p. 011 108, Jul. 2012.
- [90] S. L. Madorsky and S. Straus, “Thermal degradation of polymers at high temperatures,” *Journal of Research of the National Bureau of Standards Section A: Physics and Chemistry*, vol. 63A, no. 3, p. 261, Nov. 1959.
- [91] J. Ballato, T. Hawkins, P. Foy, R. Stolen, B. Kokuoz, M. Ellison, C. McMillen, J. Reppert, A. M. Rao, M. Daw, S. R. Sharma, R. Shori, O. Stafsudd, R. R. Rice, and D. R. Powers, “Silicon optical Fiber,” *Optics Express*, vol. 16, no. 23, p. 18 675, Nov. 10, 2008.
- [92] A. Gumennik, L. Wei, G. Lestoquoy, A. M. Stolyarov, X. Jia, P. H. Rekemeyer, M. J. Smith, X. Liang, B. J. Grena, S. G. Johnson, S. Gradečak, A. F. Abouraddy, J. D. Joannopoulos, and Y. Fink, “Silicon-in-silica spheres via axial thermal gradient in-fibre capillary instabilities,” *Nature Communications*, vol. 4, no. 1, p. 2216, Oct. 2013.
- [93] J. Zhao, A. Javadi, T.-C. Lin, I. Hwang, Y. Yang, Z. Guan, and X. Li, “Scalable Manufacturing of Metal Nanoparticles by Thermal Fiber Drawing,” *Journal of Micro and Nano-Manufacturing*, vol. 4, no. 4, p. 041 002, Oct. 2016.
- [94] N. Mott, “Conduction in glasses containing transition metal ions,” *Journal of Non-Crystalline Solids*, vol. 1, no. 1, pp. 1–17, Dec. 1968.
- [95] N. P. Bansal and R. H. Doremus, *Handbook of Glass Properties*. Elsevier, 1986.
- [96] W. Höland and G. H. Beall, *Glass-Ceramic Technology*. Hoboken, NJ, USA: John Wiley & Sons, Inc., Jun. 2012.
- [97] L. Murawski, C. Chung, and J. Mackenzie, “Electrical properties of semiconducting oxide glasses,” *Journal of Non-Crystalline Solids*, vol. 32, no. 1, pp. 91–104, Feb. 1979.

- [98] S. Tomotika and T. G. Ingram, “On the instability of a cylindrical thread of a viscous liquid surrounded by another viscous fluid,” *Proceedings of the Royal Society of London. Series A - Mathematical and Physical Sciences*, vol. 150, no. 870, pp. 322–337, Jun. 1935.
- [99] T. Khudiyev, O. Tobail, and M. Bayindir, “Tailoring self-organized nanostructured morphologies in kilometer-long polymer fiber,” *Scientific Reports*, vol. 4, no. 1, p. 4864, May 2015.
- [100] F. Tan, R. R. Naraghi, S. Sukhov, A. Dogariu, and A. F. Abouraddy, “Diffusive Scattering from a Single Composite Microsphere Fabricated by an In-Fiber Fluid Instability,” in *Photonics and Fiber Technology 2016 (ACOFT, BGPP, NP)*, Sydney, NSW, AUS: OSA, 2016, AW3C.3.
- [101] W. Hills, “Method of making plural component fibers,” U.S. Patent 5,162,074, Nov. 10, 1992.
- [102] A. Wilkie and H. Balk, “Method and apparatus for producing polymer fibers and fabrics including multiple polymer components,” U.S. Patent 7,740,777 B2, Jun. 22, 2010.